NOVEL OPTICAL CHARACTERISTICS AND APPLICATIONS OF 3D POLYSTYRENE COLLOIDAL PHOTONIC CRYSTALS

A Thesis Submitted for the Degree of

DOCTOR OF PHILOSOPHY

By

K. SHADAK ALEE

School of Physics

University of Hyderabad

Hyderabad - 500 046

India

July 2012

To my Parents,
Brother and Sister

DECLARATION

I here by declare that the matter embodied in the thesis entitled "**Novel optical characteristics and applications of 3D polystyrene colloidal photonic crystals**" is the result of investigation carried out by me in the School of Physics, University of Hyderabad, India, under direct supervision of Prof. D. Narayana Rao.

Place: Hyderabad

Date: (K. Shadak Alee)

CERTIFICATE

This is to certify that the work described in this thesis entitled "**Novel optical characteristics and applications of 3D polystyrene colloidal photonic crystals**" has been carried out by **K. Shadak Alee**, under my direct supervision and this has not been submitted for any degree or diploma at this or any other University.

Place: Hyderabad

Date: **(Prof. D. Narayana Rao)**

Dean
School of Physics

ACKNOWLEDGEMENTS

I express my deep sense of gratitude and profound thanks to my thesis supervisor, Prof. D. Narayana Rao, for his inspiring guidance and constant encouragement throughout the course of this research work. I have been able to learn a great deal in this fascinating field of research through his inspiring and thought provoking discussions, and I consider my association with him a rewarding experience. His guidance to me goes even beyond science and he has helped me to grow as a strong individual.

I thank Prof. S. P. Tewari, Dean, School of Physics, former Dean Prof. C. Bansal, and faculty for their co-operation in providing facilities in the School. I should also express my sincere thanks to Dr. Suneel Singh for his constant support and discussion in understanding some of theoretical concepts related to my dissertation work. I would like to thank Dr. V. Nirmal Kumar and Prof. S. Dutta Gupta, for their valuable suggestions at Doctoral committee meetings. The encouragement and support provided by the Non-teaching staff in the school is highly appreciable.

I wish to thank and appreciation to all my lab seniors, Bhakta, Chaitanya, Venkatram, Sai Santosh, Manoj, and Kurumurthy for constantly encouraging and supporting me throughout my time here. Thanks to my present lab members Dr. Satyavati, Deepak, Shekar, Sriram, Srirramulu, Kuladeep and Ashok for creating friendly and pleasant lab atmosphere. Special thanks to Bala Murali Krishna for his encouragement and helpful discussions in nonlinear absorption experiments. Without the support of these guys this thesis work wouldn't have been successful. I would like to thank technical assistants Deepti and Laxmi Narayana for their cooperation in using micro-Raman and FESEM instruments.

I would like to thank Prof. T. P. Radha Krishnan, School of Chemistry and his students Gupta, Hari and Ramesh for their helpful discussions in the mechanisms of various polymerization techniques. I would also like to thank Prof. P. S. R. Prasad, NGRI, Hyderabad, for his valuable discussion in the area of Raman spectroscopy.

I would like to thank all my teachers, especially a high school teacher, C. Subramanyam, who always supported and encouraged me at school level to reach this position.

At this juncture, I should extend my sincere thanks and deep appreciation to my friends Durga Rao and Sanyasi Rao for being my strength right through the course of my Ph.D days. I would like to thank my Ph.D batchmates Shankar, Chari, Anil Kumar, Balaji, Yugandar, Vasu, Rambabu, Bheema Lingam, Partha Sarathi, Sita, Arun, Devaraju, Venkaiah, Vijayan and I am also thankful to Anjaneyulu, Sree Hari, Satya Narayana, Sudha Nirmala for their constant encouragement and support throughout the duration of this period.

I would like to thank M.Sc. Project students Carina, Vikram, Sree Parvati and Sona Chandran for having nice time and discussions. Thanks are also due to all those whose names are missing in this list and have helped me in various stages of my work.

Financial assistance, in the form of Senior Research Fellowship from Council of Scientific and Industrial Research (CSIR) is gratefully acknowledged.

The unconditional love of my sister, father and brother and their blessings made me what I am today and I owe everything to them. A special word of appreciation to my cousin brother, for his timely help during the starting days of my course in this University. I would like to thank all my family members and relatives for their support and guidance throughout my life.

K. Shadak Alee

Table of Contents

Declaration		i
Certificate		ii
Acknowledgments		iii
List of abbreviations		ix
Chapter 1: Introduction: Photonic crystals		**1-30**
1.1	Photonic crystals	3
1.2	Photonic band structure calculations	5
	1.2.1 Reciprocal lattice	6
	1.2.2 Plane wave expansion method	8
	1.2.3 Towards Complete photonic band gap	11
1.3	Refraction in photonic crystals	15
1.4	Density of states in photonic crystals	16
1.5	Slow-photon effects	18
1.6	Natural Opals	19
1.7	Fabrication methods	21
1.8	Applications	25
1.9	Organization of thesis	26
1.10	References	27
Chapter 2: Experimental details and techniques		**31-45**
2.1	Transmission/Reflection spectrophotometer	33
2.2	Field Emission-Scanning Electron Microscopy (FE-SEM)	35
2.3	Z-scan	
	2.3.1 Open-aperture Z-scan for nonlinear absorption	39
2.4	Micro-Raman spectrometer	40
2.5	Modified Bragg's law	43
2.6	References	45
Chapter 3: Fabrication and optical characterization of 3D colloidal photonic crystals		**46-74**
3.1	Introduction	48
3.2	Synthesis of polystyrene microspheres	
	3.2.1 Emulsion polymerization	49
3.2	Vertical deposition method	53
3.3	Optical Characterization	56
3.4	Thickness measurement	57
3.5	Angle dependant spectral characteristics due to (111) plane	59
3.6	Scalar-wave approximation (SWA)	61
3.7	Spectral characteristics in the LU and LK path of the first Brillouin zone	63
3.8	Polarization dependant spectral characteristics	68
3.9	Conclusions	71
3.10	References	72

Chapter 4: Spectral and morphological changes of 3D polystyrene photonic crystals with the incorporation of alcohols **75-88**

4.1 Introduction 77
4.2 Experimental Details 78
4.3 Results and Discussion 79
4.4 Conclusions 87
4.5 References 87

Chapter 5: Experimental verification of enhanced electromagnetic fields at the band edge of 3D polystyrene photonic crystals using Z-Scan technique **89-106**

5.1 Introduction 91
5.2 Nonlinear absorption 92
5.3 Motivation of the experiment 95
5.4 Experimental details for Z-Scan 97
5.5 Results and Discussion 98
5.6 Conclusions 104
5.7 References 105

Chapter 6: In-situ investigation of the formation of silver nanoparticles in polyvinyl alcohol through Raman spectroscopy **107-138**

6.1 Background of Raman scattering 109
6.2 Surface enhanced Raman spectroscopy
6.2.1 Electromagnetic model 113
6.2.2 Chemical Enhancement 114
6.3 Micro-Raman studies of silver nanoparticles incorporated polystyrene photonic crystals
6.3.1 Experimental Results and Discussion 116
6.4 In-situ observation of silver nanoparticle formation through micro-Raman studies
6.4.1 Experimental Details 120
6.4.2 Results and Discussion
6.4.2.1 Studies with nanosecond pulsed laser excitation in polyvinyl alcohol + silver nitrate thin films 121
6.4.2.2 Confocal-micro-Raman studies on SERS 122
6.4.2.3 514 nm CW excitation 124
6.4.2.4 633 nm CW excitation 124
6.4.2.5 785 nm CW excitation 125
6.4.2.6 Studies with CW laser excitation in thin films of polyvinyl alcohol + silver nitrate 128
6.4.2.7 Heat generation due to silver nanoparticles 130
6.4.3 Light scattering in a pure solution of polyvinyl alcohol + silver nitrate 132
6.5 Conclusions 135
6.6 References 136

Chapter 7: Conclusions & Future perspectives **139-143**

7.1 Conclusions 140
7.2 Future perspectives 141
7.3 References 143

List of publications **144-148**

List of abbreviations

AgNPs	: Silver nanoparticles
BZ	: Brillouin zone
CPBG	: Complete photonic band gap
CW	: Continuous wave
CT	: Charge transfer
DOS	: Density of states
EFS	: Equifrequency surfaces
EF	: Enhancement factor
EM	: Electromagnetic
fcc	: Face centred cubic
FESEM	: Field emission scanning electron microscope
hMi	: high Miller index
PBG	: Photonic band gap
PC	: Photonic crystal
PCF	: Photonic crystal fibre
pDOS	: photonic density of states
PS	: Polystyrene
PVA	: Polyvinyl alcohol
LDOS	: Local density of states
NP	: Nanoparticle
RIC	: Refractive index contrast
SEM	: Scanning electron microscope
SERS	: Surface enhanced Raman scattering
SWA	: Scalar wave approximation

CHAPTER 1

Abstract

This chapter provides a detailed coverage on the novel optical properties of photonic crystals. A brief review on the construction of reciprocal lattice, important mathematical issues related to plane wave expansion method to calculate photonic band diagrams and required criteria to possess full photonic band gap are discussed. Important concepts of density of states and refraction in photonic crystals are presented. A wide variety of methods that have been used to fabricate photonic crystals of different dimensions and their applications are discussed. An overview of the thesis is presented at the end.

Introduction: Photonic crystals

1.1 Photonic crystals

'*Nanostructured materials containing ordered arrays of holes could lead to an optoelectronic revolution, doing for light what silicon did for electrons.*' This statement is made by Eli Yablonovitch and his pioneer work has lead to the field of so called 'photonic crystals (PCs).' These materials open an avenue to explore novel photonic applications based on the fundamental concepts of localization of light as well as control on spontaneous emission. In 1887, Lord Rayleigh was the first who studied the propagation of electromagnetic waves through 1D periodic layered structure and proposed the concept of quarter wave stack.[1] 100 years later, the study of spontaneous emission suppression in periodic structures by V. P. Bykov[2] in 1972 and extension of this work through complete photonic band gap (CPBG) structures by E. Yablonovitch[3] and S. John[4] in 1987 have led to increasing interest in PCs.

In an ordinary atomic crystal, the parallel planes which satisfy Bragg's law diffract X-rays for certain angles of incidence. As the refractive index contrast (RIC) for X-rays in crystals is very small, generally 1 part in 10^4, the forbidden X-rays form extremely narrow stop band.[5] The Bragg reflection equally applies to all wavelengths larger than the wavelength of X-rays if some dielectric materials are arranged periodically whose lattice constant approximately matches with the incident wavelength. Thus the spatial arrangements of low loss materials whose dielectric constants vary periodically either in 1D, 2D or 3D are classified into a novel type of photonic materials called 'PCs' or 'photonic band gap (PBG) materials'. A region in which the propagation of electromagnetic waves is forbidden is called PBG. For those wavelengths contained within these gaps, the associated wave vector takes an imaginary value and light propagating along the crystal with those wavelengths is exponentially attenuated.[6]

The electronic band structure is described by solving the time independent Schrödinger equation for the case of semiconductor crystals. Similarly band structure of photons in PCs can be obtained by solving Maxwell equations. Just in the same way as the strong periodic potentials in an ordinary crystal open up complete band gap to the electron motion, the larger RIC and type of arrangement of materials will decide the complete photonic band gap (CPBG) of PC.[6]

A quarter wave stack which consists of alternating layers of different dielectric materials is a widely used and well known example of 1D PC. Its schematic is shown in figure 1a. In a quarter wave stack the gap to midgap frequency ratio is related to the refractive indices of its constituent materials as given below[7]

$$\frac{\Delta\omega}{\omega_m} = \frac{4}{\pi} sin^{-1}\left(\frac{|n_1 - n_2|}{n_{1+}n_2}\right) = \frac{4}{\pi} sin^{-1}\left(\frac{\left|\frac{n_1}{n_2} - 1\right|}{\frac{n_1}{n_2} + 1}\right) \quad (1)$$

Here $\Delta\omega$ and ω_m are width and central frequency of band gap; n_1 and n_2 are the refractive indices of alternating layers with period 'a'. Figures 1b-d represents the dispersion relations of multilayer films with different RICs (RIC = $n_1 : n_2$). These band diagrams were calculated using RSoft's BandSOLVE commercial software, which implements the plane wave expansion method.[8] In all cases, each layer has the same width of $a/2$. The frequency is expressed in dimensionless units of $\frac{\omega a}{2\pi c} = \frac{a}{\lambda}$; where λ and c are the wavelength and velocity (in free space) of light. In the case of RIC = 3.6:3.5 (figure 1b), a very narrow band gap (shaded region) is opened between the first two bands (n = 1, 2) and further increased RIC between the alternating layers has resulted in a wider band gap (figure 1c and 1d) which confirms the band gap width is proportional to RIC.

According to 'Variational principle' the major power of the E-field of electromagnetic modes below the gap is concentrated in high-ε regions and vice versa. The band directly below a gap is referred to as the dielectric band and the band above the gap is the air band. In between the two bands a frequency gap – the PBG –

develops, where no extended modes can exist inside of the material. This is pretty much the same situation as the electronic band structure in semiconductor physics where the fundamental gap has the valence band below and the conduction band above.

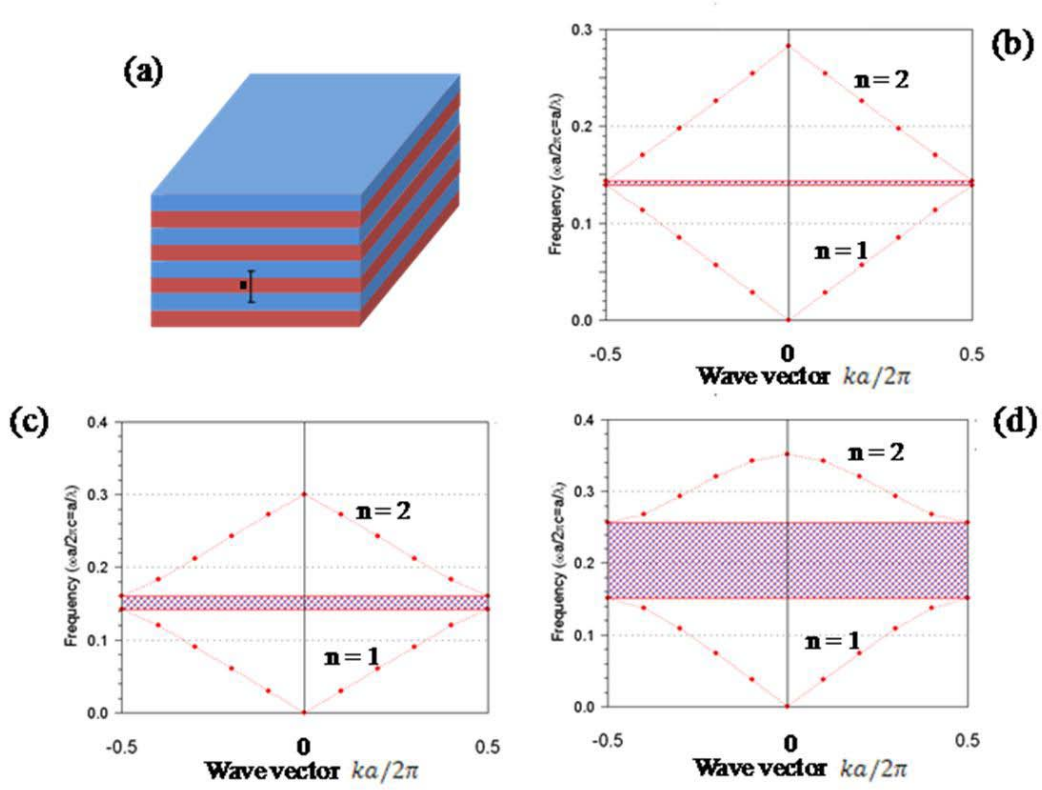

Figure 1: a) A multilayer film of 1D PC containing alternating layers with refractive index n_1 and n_2 with the period 'a'. The dispersion relations are calculated for different multilayer films with refractive index contrast (RIC) of b) 3.6:3.5, c) 3.6:3 and d) 3.6:1. The ordinate is plotted in dimensionless frequency units: $\frac{\omega a}{2\pi c} = \frac{a}{\lambda}$; λ and c are the wavelength and velocity (in free space) of light. In all cases each layer has a width of $a/2$. Shaded region indicate the photonic band gap.

1.2 Photonic band structure calculations

Optical properties of homogeneous isotropic materials can be simply characterized by the dielectric constant ε. Electromagnetic radiation of frequency ω in such a medium propagates in the form of plane waves, $\overline{E}\,(\bar{r},t)$ or $(\overline{H}\,(\bar{r},t)) = \bar{E}_0 e^{i(\bar{k}.\bar{r}-\omega t)}$

or ($\bar{H}_0 e^{i(\bar{k}.\bar{r}-\omega t)}$), ($\bar{E}_0$ and $\bar{H}_0$ represents the amplitude of electric and magnetic fields, respectively.) with vectors of electric field $\bar{E}(\bar{r},t)$, magnetic field $\bar{H}(\bar{r},t)$ and a wave vector $\bar{k}$ forming an orthogonal triplet. In such materials, the dispersion relation connecting wave vector and frequency is given by $\omega(k) = \frac{kc}{n}$, (c is the speed of light) which is known as 'light line'. The propagation of light modes lies along this 'light line'. However, to solve the dispersion relation $\omega(k)$ in 3D PC structures, one should know some basics of crystal structures and their transformation into reciprocal space which are discussed in the following section.

1.2.1 Reciprocal lattice

A 3D PC is generated by placement of duplicates of a basic dielectric structure, such as a sphere or a cube, at points of a 3D lattice generated by lattice vectors $\bar{R} = l\bar{a}_1 + m\bar{a}_2 + n\bar{a}_3$, where l, m and n are integers, and $\bar{a}_1$, $\bar{a}_2$ and $\bar{a}_3$ are primitive vectors defining the lattice unit cell. The overall structure is periodic and its physical properties, such as dielectric constant $\epsilon(\vec{r})$ are invariant to the translation by $\bar{R}$.

$$\epsilon(\bar{r}) = \epsilon(\bar{r} + \bar{a}) \quad \forall\, \bar{r}. \tag{2}$$

This periodic function may therefore be expanded in a 3D Fourier series.

$$\frac{1}{\epsilon(\bar{r})} = \sum \kappa(\bar{G})\, e^{i\bar{G}.\bar{r}} \tag{3}$$

where $\bar{G} = p\bar{b}_1 + q\bar{b}_2 + r\bar{b}_3$ is a vector defined by the primitive vectors $\bar{b}_1$, $\bar{b}_2$, $\bar{b}_3$ of another lattice, the reciprocal lattice, and p, q and r are integers. The $\bar{b}$ vectors are related to the $\bar{a}$ vectors via

$$\bar{b}_1 = 2\pi \frac{\bar{a}_2 \times \bar{a}_3}{\bar{a}_1.(\bar{a}_2 \times \bar{a}_3)},\ \bar{b}_2 = 2\pi \frac{\bar{a}_3 \times \bar{a}_1}{\bar{a}_2.(\bar{a}_3 \times \bar{a}_1)},\ \bar{b}_3 = 2\pi \frac{\bar{a}_1 \times \bar{a}_2}{\bar{a}_3.(\bar{a}_1 \times \bar{a}_2)} \tag{4}$$

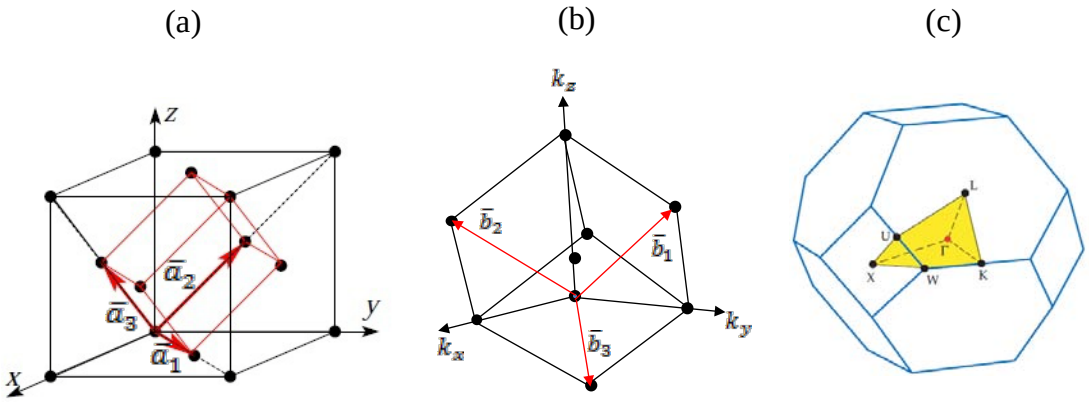

Figure 2: a) The rhombohedral primitive cell (indicated by red lines) of the face-centered cubic crystal. b) The corresponding reciprocal lattice is a body-centered cubic crystal. c) The Brillouin zone of face-centered cubic is a truncated octahedron and the shaded polyhedron region indicates the irreducible Brillouin zone whose corner points are marked by the crystallographic symbols $\Gamma XUKW$. $\bar{a}_1$, $\bar{a}_2$ and $\bar{a}_3$ are the primitive vectors in real space and $\bar{b}_1$, $\bar{b}_2$ and $\bar{b}_3$ are their corresponding primitive vectors in reciprocal space.

So that $\bar{b}_1.\bar{a}_1 = 2\pi$, $\bar{b}_1.\bar{a}_2 = 0$ and $\bar{b}_1.\bar{a}_3 = 0$, i.e. $\bar{b}_1$is orthogonal to $\bar{a}_2$ and $\bar{a}_3$ and its length is inversely proportional to $\bar{a}_1$. Similar properties apply to $\bar{b}_2$ and $\bar{b}_3$. It can also shown that $\bar{G}.\bar{R} = 2\pi$. An example of 3D crystal lattice for face centered cubic (fcc) and its corresponding reciprocal lattice (body centered cubic) with Brillouin zone (BZ) are shown in figures 2a, 2b and 2c, respectively.

Given a lattice with primitive vectors $\bar{R}_i$, we can consider a plane passing through the end of 3 translation vectors as: $(n_1\bar{a}_1, n_2\bar{a}_2, n_3\bar{a}_3)$ with (n_1, n_2, n_3) integer numbers. The inverses of the 3 integers define the Miller indices. However, as the inverse is not necessarily an integer, the Miller indices are the smallest integers with the same ratio as $(1/n_1, 1/n_2, 1/n_3)$. They are usually labeled as (hkl). Clearly a given (hkl) refers to a family of parallel planes. One can show that the vector $\bar{r} = \sum_{i=1,3} x_i\,\bar{a}_i$ belongs to a plane with Miller indices (hkl) if and only if $\bar{r}.\bar{G}$ = integer, with $\bar{G} = h\bar{G}_1 + k\bar{G}_2 + l\bar{G}_3$. Each value of the integer refers to $\bar{r}$ belonging to one plane in the family. Crystalline "directions" use a different convention. A direction defined by $\bar{R} = n_1\bar{a}_1 + n_2\bar{a}_2 + n_3\bar{a}_3$ is labeled as $[n_1 n_2 n_3]$.

A family of planes related to the (hkl) planes by a rotational symmetry operation of the lattice are denoted by $< hkl) >$. $\{hkl\}$ refers to all the planes parallel to the direction $[hkl]$.

The Wigner-Seitz Cell is defined as the primitive cell of a crystal in real space which is formed as the set of points that are closer to a given lattice point than to any other lattice point. Its analogy in reciprocal space is called the first Brillouin zone (BZ). It plays a crucial role in the description in the analysis of the energy band structure in electronic and PCs and also offers a vivid picture of diffraction within the crystal. Details can be found in every solid state physics textbooks.[9,10] The smallest region within the BZ for which the dispersion relations are not related by symmetry is called the irreducible BZ and the shaded region in Figure 2c represents the irreducible BZ for fcc crystal lattice. In chapter 3, the stop bands due to different Miller index planes of 3D polystyrene PCs that present in the LU and LK path of the BZ were discussed.

1.2.2 Plane wave expansion method

Schrodinger equation solves the band structure for electron motion; similarly the band structure for photons in PCs can be solved using Maxwell's equations. With the assumption that the medium is free of charges and currents, the wave equation for both electric and magnetic fields can be written as below, which forms the Master equation to solve the eigen values that give the allowed frequencies through the PC structure.[8]

$$\overline{\nabla} \times \frac{1}{\epsilon(\bar{r})} \overline{\nabla} \times \bar{H}(\bar{r}) = (\frac{\omega}{c})^2 \bar{H}(\bar{r}) \quad (5)$$

$$\overline{\nabla} \times \overline{\nabla} \times \bar{E}(\bar{r}) = \epsilon(\bar{r})(\frac{\omega}{c})^2 \bar{E}(\bar{r}) \quad (6)$$

The information about PC is given by dielectric function $\epsilon(\bar{r})$, which is periodic in space. To analyze wave propagation in periodic systems and to compute the photonic

band structure, the plane wave expansion method (PWM) is adapted. It is based on the Bloch-Floquet theorem, which allows expanding the eigen functions $\bar{E}(\bar{r})$ or $\bar{H}(\bar{r})$ of a wave equation in a periodic environment in the form of plane waves, which are modulated by lattice periodic function

$$\bar{E}_k\,(\bar{r}) = \bar{u}_k\,(\bar{r}) e^{i\bar{k}.\bar{r}} \tag{7}$$

and $\overline{\mathrm{H}}_{\mathrm{k}}(\overline{r}) = \bar{v}_k\,(\bar{r}) e^{i\bar{k}.\bar{r}}$ (8)

With a periodic function $u_k\,(\bar{r})$ and $v_k\,(\bar{r})$ which have the same periodicity as the lattice i.e.

$$u_k\,(\bar{r}) = u_k\,(\bar{r} + \bar{a}) \quad \forall\, \bar{a} \tag{9}$$

where $\bar{a}$ indicates the elementary lattice vector of the PC. Thus the eigen function of a wave equation 2 and 3 on a periodic lattice is the product of a plane wave $e^{i\bar{k}.\bar{r}}$ and the lattice periodic function, $\bar{u}_k\,(\bar{r})$, where the wave vector $\bar{k}$ can be restricted to the BZ.

Similarly the dielectric function $\epsilon(\vec{r})$ its reciprocal value is expanded into a Fourier series $\frac{1}{\epsilon(\bar{r})} = \sum \kappa(\bar{G})\, e^{i\bar{G}.\bar{r}}$ (10)

With $\epsilon(\bar{r}) = \epsilon\,(\bar{r} + \bar{a})$. Here $\kappa(\bar{G})$ is the Fourier coefficient and it can be calculated through integration over the Wigner-Seitz cell (WSC) with a volume V as given below.

$$\kappa(\bar{G}) = (\tfrac{1}{V}) \int_V d^3\,\bar{r}\epsilon^{-1}(\bar{r}) e^{-i\bar{G}.\bar{r}} \tag{11}$$

Similarly the Fourier expansion of $\vec{E}(\vec{r})$ and $\vec{H}(\vec{r})$ leads to the following form of the eigenfunctions

$$\bar{H}_{\bar{k}}(\bar{r}) = \sum_{\bar{G}} \bar{H}_{\bar{k}}(\bar{G})\, e^{i\{\bar{k}+\bar{G}\}.\bar{r}} = \sum_{G} \sum_{j=1}^{2} h_{\bar{G}}^{j}\, e_{\bar{G}}^{j} e^{i\{\bar{k}+\bar{G}\}.\bar{r}} \quad (12)$$

where $h_G$is the Fourier coefficient, and j labels the two transverse polarizations of any plane wave such that $e_{\bar{G}}^{j=1,2}$and $\bar{k}+\bar{G}$ form an orthogonal triad. Because of the discrete translational symmetry of the lattice, the wave vector $\bar{k}$ may be restricted to lie in the first BZ.

Substituting equations 10 and 12 into master equations 5 and 6 leads an infinite, Hermitic matrix eigen value problem for the eigen frequencies $\omega(\bar{k})$ of the crystal for a given wave vector $\bar{k}$ of the form.

$$\sum_{\bar{G}} \sum_{j=1}^{2} M_k^{ij}\ (\bar{G}, \bar{G}') h_k^{\bar{G}'j} = \frac{\omega_k^2}{c^2} h_k^{\bar{G}'j} \quad (13)$$

With the matrix elements

$$M_k(G, G') = \left|\bar{k}+\bar{G}\right|\left|\bar{k}+\bar{G}'\right| \kappa(\bar{G}-\bar{G}') \times \begin{pmatrix} e_{\bar{G}_2}.e_{\bar{G}'_2} & -e_{\bar{G}_2}.e_{\bar{G}'_1} \\ -e_{\bar{G}_1}.e_{\bar{G}'_2} & e_{\bar{G}_1}.e_{\bar{G}'_1} \end{pmatrix} \quad (14)$$

After calculating $\vec{H}$, the electric field corresponding to a given eigen frequency $\omega(\bar{k})$ can be obtained from the Maxwell's equation

$$\bar{E}_{n\bar{k}}(\bar{r}) = -i \frac{c}{\omega_n(\bar{k})}\, \epsilon^{-1}(\bar{r}) \bar{\nabla} \times \bar{H}_{n\bar{k}}(\bar{r}) \quad (15)$$

The band structure for the photons can be generated for a finite number of high symmetric reciprocal lattice vectors which forms irreducible BZ. The band structures shown in this thesis were computed using commercially available RSoft's BandSOLVE software.

An important property of Master equation is that it is scale independent. If all the dimensions of the system are multiplied by 5, then the solutions are exactly the same except the frequencies are divided by 5. Hence, the equations are solved once and the

same result can be applied to problems at all length scales and frequencies. This scale invariance leads to use dimensionless units for distance and time. Hence, in the band structure calculations, a natural length scale 'a' (which is a periodicity) is chosen and all the distance and angular frequencies ω are the multiples of 'a' and $\frac{\omega a}{2\pi c}(=\frac{a}{\lambda})$ respectively.

1.2.3 Towards Complete photonic band gap

The complete photonic band gap of a PC which provides band gap in all directions for TE and TM polarizations, localizes light in three dimensions without any leaky modes, strongly suppresses or enhances emission of dyes and reduces the threshold for the lasing action.[11,12] We discussed in the following paragraphs briefly about the kind of band gap existed with different dimensional PCs.

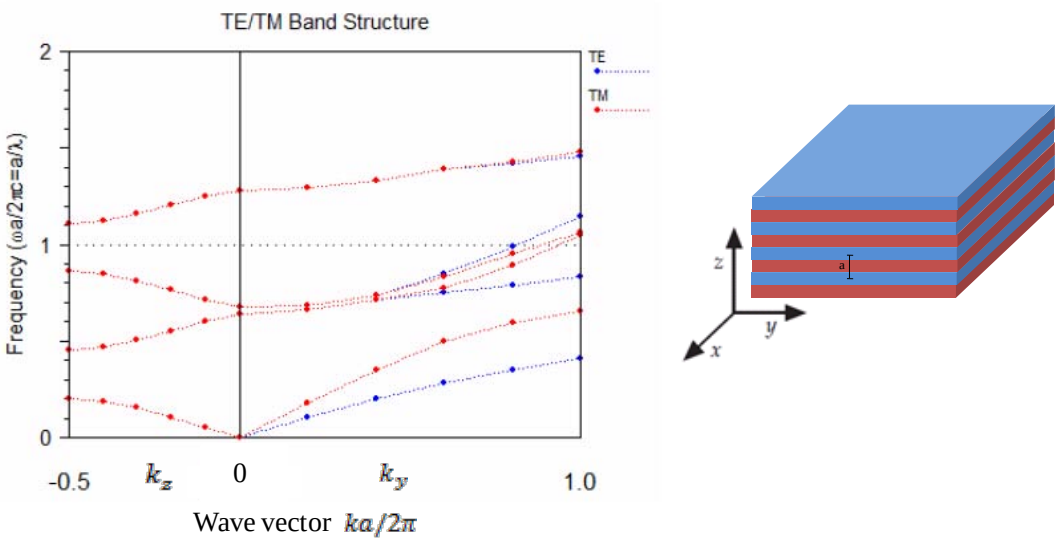

Figure 3: The band structure of a multilayer film of GaAs/Air (RIC = 3.6:1) generated using RSoft (BandSOLVE). The on-axis bands (0, 0, k_z) are shown on the left side, and an off-axis band structure (0, k_y, 0) is displayed on the right. On-axis, the bands overlap—they are degenerate. Along k_y, the bands split into two distinct polarizations. Blue indicates TM modes polarized so that the electric field points in the x - direction, and red indicates TE modes polarized in the yz plane.

As 1D PCs provide band gap only in the direction of periodicity (on-axis) and there are no band gaps for off-axis propagation as shown in figure 3. This is always the case for a multilayer film, because the off-axis direction contains no periodic dielectric regions to coherently scatter the light and split open a gap.

A 2D PC is formed by fabricating a structure that has periodicity in two directions, such as by etching a periodic array of dielectric rods in air or pores in Si. The PBG is naturally restricted to a plane, whereas in the third dimension EM waves can propagate freely. Unlike the multilayer film, this 2D PC can prevent light from

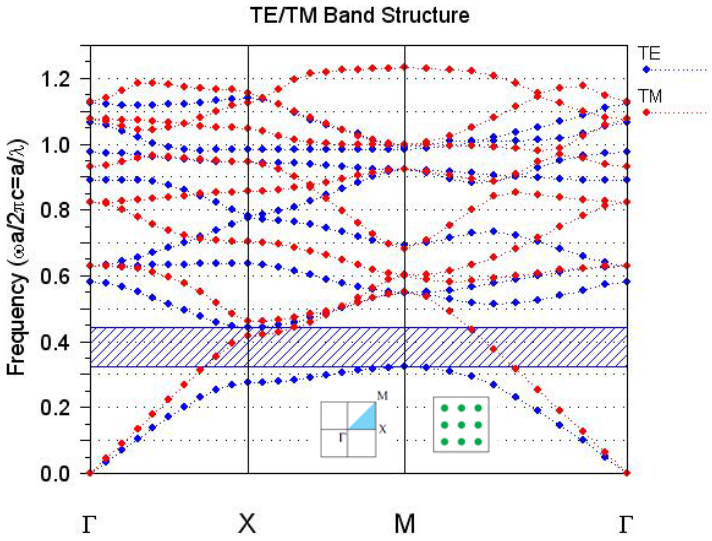

Figure 4: Calculated photonic band structure (using RSoft (BandSOLVE)) of 2D PC made of dielectric cylindrical columns (RIC = 2.98) of radius r=0.2a organized in the form of a square lattice with lattice constant 'a'. The abscissa spans Bloch wave vectors defined by points on the periphery of the irreducible Brillouin zone, the ΓMK triangle (left inset). The ordinate is plotted in units of $\frac{\omega a}{2\pi c}$*. The right inset shows a cross-sectional view of the dielectric function. The blue bands represent TE modes and the red bands represent TM modes.*

propagating in any direction within the plane of periodicity. 2D PCs show a strong polarization dependence of the PBG, for example, a PC of dielectric cylindrical columns with square periodicity possesses a CPBG for TM modes where as it shows

a directional band gap for TE modes as shown in figure 3. A detailed explanation can be found in reference [6].

An fcc lattice is more favourable for 3D PC since its BZ is a truncated octahedron and therefore close to spherical (compared to the other Bravais lattices) which improves the prospects for a forbidden gap to overlap all the way and may lead to CPBG.[13,14] As presented in figure 5a, an opal structure with RIC = 1.59 possesses a pseudo band gap between 2nd and 3rd bands. An inverse opal structure with a RIC of 3.2 produces CPBG and it is expected to open up between the 8th and 9th bands as shown in figure 5b. Since the band is located between high-frequency bands it is unfortunately very sensitive to disorder within the crystal structure.[14] The gap opens between the 2nd and 3rd band and is approximately three times wider than the gap in a simple fcc structure[8] and more robust against disorder and structural

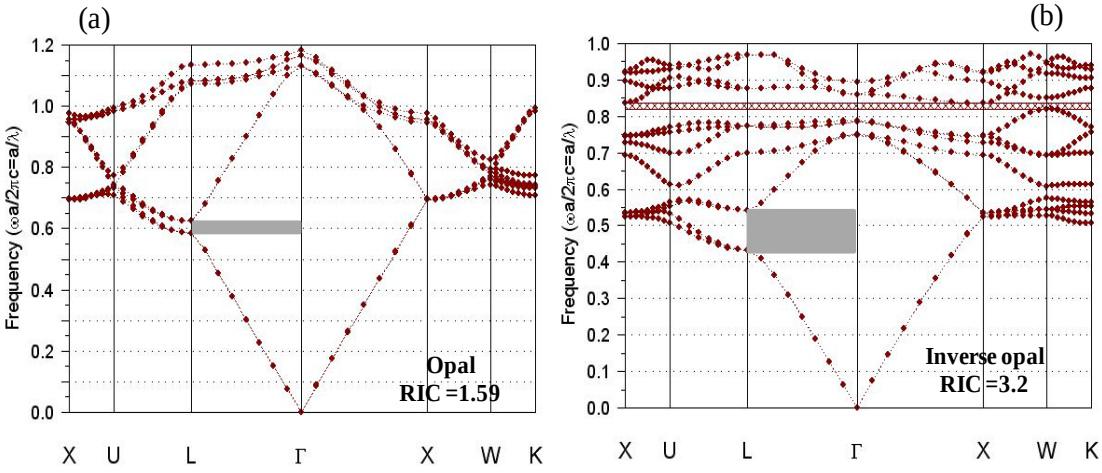

Figure 5: Calculated photonic band structure (using RSoft (BandSOLVE)) for a) direct (RIC = 1.59) and b) inverted opal (RIC = 3.2). A complete PBG cannot build up in direct opal due to insufficient RIC (figure a). For inverted opal with a high refractive index a CPBG emerges between the 8th and band 9th (figure b, shaded with ' ×' marks). A directional gap in Γ-L direction is always present between the 2nd and 3rd band (grey shaded) for both the structures.

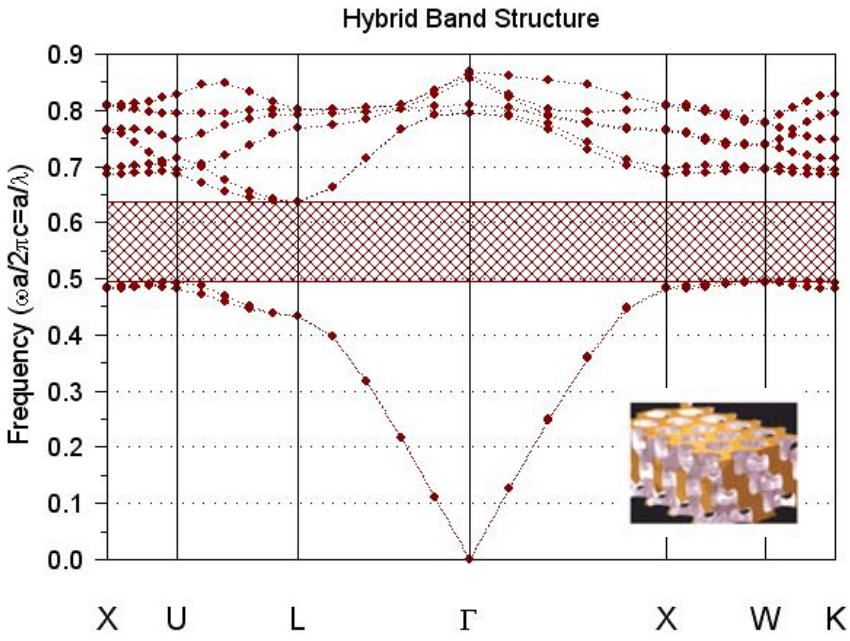

Figure 6: Calculated photonic band structure (using RSoft (BandSOLVE)) of Yablonovite. CPBG is shaded in red color and the inset represents the lattice structure of Yablonovite.

defects.[15] It should be mentioned that the diamond structure is even more favourable to show a CPBG. The Bravais lattice of the diamond structure is fcc as well, but with a two-atom basis leading to a different structure factor that supports the opening of a CPBG. The diamond structure is highly difficult to produce in artificial opals and inverse opal structures which are mostly created by a self-assembly process of spheres.

However, the first experimental observation of a 3D CPBG was made by Eli Yablonovitch in 1991 using a variant of the diamond lattice structure, now known as the Yablonovite.[16] This slanted-pore structure is fabricated by drilling a periodic array of cylindrical holes at specified angles in a dielectric slab. Three holes are drilled at each point of a 2D triangular lattice at the surface of slab; the directions of the holes are parallel to three of the axes of the diamond lattice as shown in the inset of figure 6. This structure has a CPBG as shown in figure 6 with a gap-midgap ratio of 0.19 when the refractive index is 3.6.

1.3 Refraction in photonic crystals

The group velocity and phase velocity of light are affected by a material's dielectric constant and results into a change of the direction of propagation of light. The group velocity ($\bar{v}_g = \bar{\nabla}_k \omega$) is a vector which indicates energy propagation while phase velocity ($v_p = \omega/|k|$) is a scalar indicating the speed of light or velocity with which the electromagnetic phase wave front travel. The propagation of light is described in terms of equi-frequency (or dispersion) surfaces (EFS). An EFS is the collection of all allowed wave vectors for a particular given frequency. In a uniform and isotropic media, the EFS are just spheres given by: $k = \frac{n\omega}{c}$ where n is the refractive index and and c is the speed of light in vacuum. In a uniform material the group velocity of the incident and refracted waves are parallel to the wave vector k. Hence the direction of energy flow coincides with the direction of the wave vector. Moreover, its direction is perpendicular to EFS that is given by ω = constant, which is denoted by a

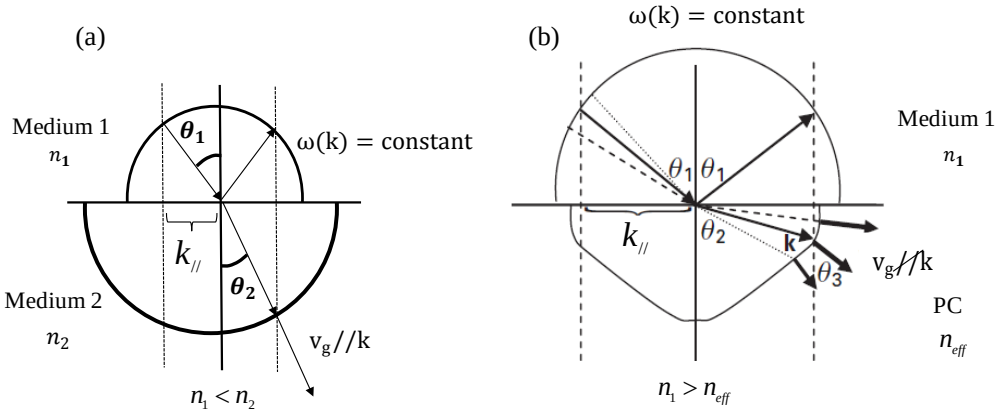

Figure 7: a) Refraction at the interface between two homogeneous dielectric media. b) Refraction at the interface between homogeneous dielectric medium and PC.

hemicircle in figure 7a. The wave vector inside the second medium is determined by the conservation of the component of the wave vector parallel to the interface ($k_{//}$),

and is parallel to the direction of propagation of energy. This yields the well known expression for Snell's law:

$$n_1 sin\theta_1 = n_2 sin\theta_2 \quad (16)$$

where n_i and θ_i are the refractive index and propagation angles in each medium.

In a PC structure, the EFS are not smooth and deviate from the spherical nature and lead to a marked difference[17] as shown in figure 7b. The wave vector of the refracted wave has its end point on the EFS given by the band structure of PC, which is drawn with a solid curve in figure 7b. Due to the acircular shape of the EFS in PCs, the direction of the group velocity can be quite different from the direction of the phase velocity ($v_p \sim k$). This effect is especially pronounced in the vicinity of the band edges, as surfaces of constant frequency are distorted more strongly at such frequencies. Therefore, when operated near the band edge, there exist regimes where a considerable change in the angles θ_3 of a transmitted light can be observed when an incident direction (angle θ_1) is only slightly varied which leads to 'super prism effect'.[18]

1.4 Density of states in photonic crystals

The electronic density of states of the semiconductors undergoes a significant modification if they are structured at nanometer scales.[19] Similarly, the periodic modulation of the refractive index at the scale of optical wavelengths leads to the change in density of photonic states (or of electromagnetic modes, DOS) which differs from the density of states in free space. The DOS is defined as the number of allowed electromagnetic modes for a unit frequency. In free space, the density of states $D(\omega)$ is proportional to ω^2, and can be expressed for a volume $'V'$ by the following equation:

$$D(\omega) = \frac{\omega^2 V}{\pi^2 c^3} \quad (17)$$

This equation still applies to a homogeneous material of refractive index n where the speed of light in the material can be replaced by $v = c/n$. For PCs this equation is no longer valid due to the dispersion characteristics $\omega(k)$ of the PC. The pDOS for

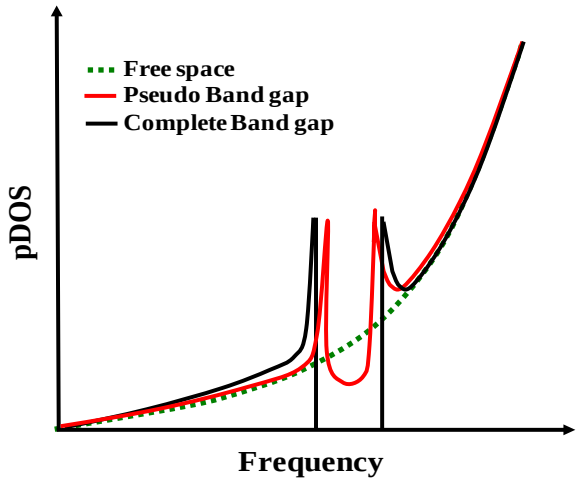

*Figure 8: Photonic d*ensity of states (pDOS) in PCs which possess a) pseudo gaps (continuous red line) and b)complete band gap (black color) compared to free space (dotted green line).

PC structure can be calculated by integrating the Dirac-δ-function over the first BZ with a summation of overall allowed transmission bands:

$$D(\omega) = \sum_n \int_{BZ} d^3\, k\; \delta(\omega - \omega_n) \qquad (18)$$

The pDOS in PCs presents a significant deviation from the DOS in free space as shown in figure 8. The pDOS significantly reduces in pseudo gaps and becomes zero at frequencies located in the CPBG while presenting maxima near the edges of this gap as shown in figure 8.

However, in a real situation of quantum optical experiments in PCs, it is necessary not to consider only the total availability of modes with a frequency ω, but also the local coupling arising between an excited atom emitting a photon at the frequency ω and the electromagnetic environment created by the PC in the region where the atom is located . In other terms, the overlap which occurs between the matrix elements of the dipolar moment of the atom on the one hand, and the electric

field of electromagnetic modes on the other hand is the determining factor of such quantum optical effects as the radiative life time of the atom. The overlap can be clearly discerned from the local photonic DOS (LDOS) defined as follows.[20]

$$D(\bar{r},\omega) = \sum_n \int_{BZ} d^3\, k\, |E_{nk}(\bar{r})|^2 \delta(\omega - \omega_n) \qquad (19)$$

Thus the LDOS differs usually from location to location in the unit cell and also from the pDOS. This indicates that the location of the active spices within the unit cell strongly influences its emission properties. If therefore makes a difference to have emitters uniformly distributed all over the unit cell or only at well defined locations.

If a full gap cannot be obtained as for example shown in figure 8a, the pDOS changes only marginally – this illustrates the difficulty to analyze the influence of the PC on the spontaneous emission, etc. in PCs with directional PBGs. Although the emission properties are influenced strongly in certain directions, the average effect can be very small.

1.5 Slow-photon effects

PCs exhibit an unique and interesting phenomenon of ‘slow light’ propagation which is not exhibited by other materials.[21] Moreover, it is expected to be relatively insensitive (“robust”) to lattice disturbances, making it especially interesting for opals. Because of the photonic band structure, light can propagate with extremely low group velocities at specific frequncies.[22,23,24] This effect is of basic as well as application interest, as it can enhance non-linear optical interactions, laser efficiencies, sensor efficiencies, and the photochemical activity of materials.[25]

In normal media, there is only small difference between phase and group velocity, but in PCs the situation alters dramatically, and v_g can be much smaller than v_p. This is a result of the band structure $\omega(k)$, or after recalculation, the strong dispersion $n(\omega)$, of these media. Slow photons are defined as being when $v_g \ll c$,

independent of the value of the phase velocity. In some cases, v_g can even be zero. In PCs, the slope of the bands, decreases when approaching the band edges, that is, the derivative of $\omega(k)$, $(\frac{d\omega}{dk})$ tends to zero. This means that the group

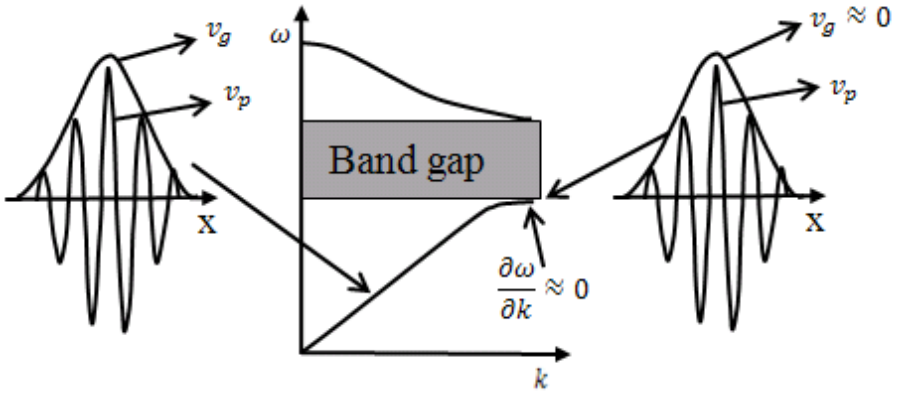

Figure 9: Electromagnetic pulse propagation in PCs. Near the center of the band gap, light travels with $v_g = v_p = c/n$ as usual. At photon energies approaching a band gap (partial or complete), the group velocity decreases and approaches zero.

velocity is considerably reduced when approaching band gaps (Figure 9). The practical applications of slow light are based on the possible strong enhancement of light–matter interactions, such as absorption and nonlinear effects. Such an enhancement can be used in optical delay lines, phase shifters, optical microamplifiers, and microlasers.[25,26]

1.6 Natural Opals

Recently a nice review article has been published on various types of natural opals discussing their shapes and various formation methods from the phenomenological point of view.[26] Natural opals have been known since ancient times. They are an unusual type of gemstone: They are not hard, they do not impress with their regular geometrical shape, but they amaze observers with their coloration, which changes when the stone is moved. This mysterious property is called opalescence. The word “opal” comes from Sanskrit (*upala* means “precious stone”), then it was used in Latin and Greek, *opalus* and *opallios*, both meaning “to see a color change”.

Generally the opal density lies between 2.0 and 2.2 g/cm^3 and they contain varying amounts of water (mostly 4–9%, sometimes 20%), and consist of silica in which impurities such as Fe^{3+}, Al^{3+}, or Ti^{3+} can be found.[27,28] Silica spheres with diameters ranging from 150 to 400 nm are often amorphous, but frequently they can also contain crystobalite and tridymite, forming imperfect stacking layers.[28]

Precious opals are considered to be one of the most beautiful gems owing to its play of color. In earlier times, the coloration of opals was believed to arise from contaminants, internal cracks, or liquids trapped within.[29] The first almost correct explanation was proposed by Raman and Jayaraman, [30] who suggested that the colors arise from diffraction of light by regular arrays of silica layers with differing refractive index. Finally, it was shown by Sanders et al.[31,32,33] in the mid- 1960s that the diffraction at regular arrays of silica spheres is responsible for the colors. Electron microscopy showed that opals consist of periodic three-dimensionally arranged silica spheres of sub micrometer size. The role of opals as a prototype for PCs is twofold. Firstly, opals are three-dimensional periodic systems, which are the most interesting PCs from the point of view of dimensionality.[6] Secondly, they represent a basic fabrication approach employing self-assembly mechanisms (bottom-up techniques) for PCs. PCs in general can be fabricated by both bottom-up and top-down approaches. These approaches compete with each other, but combinations of both are possible.

Generally, opals have millimeter-sized single-color domains with very individual irregular shapes. The color of the domains is not fully homogeneous, but appears to fluctuate slightly in the sub-millimeter range. In nearly all opals, the pores between the silica spheres are filled with water-containing silica. This filling gives the opals mechanical stability and lowers the RIC, which is advantageous for the visual impression, as it reduces scattering. As a result, the opal appears less milky and the colors seem to come from deeper regions. There is only one special sort of natural

opals known that they have very incomplete filling, the so-called 'hydrophane opals'.[29]

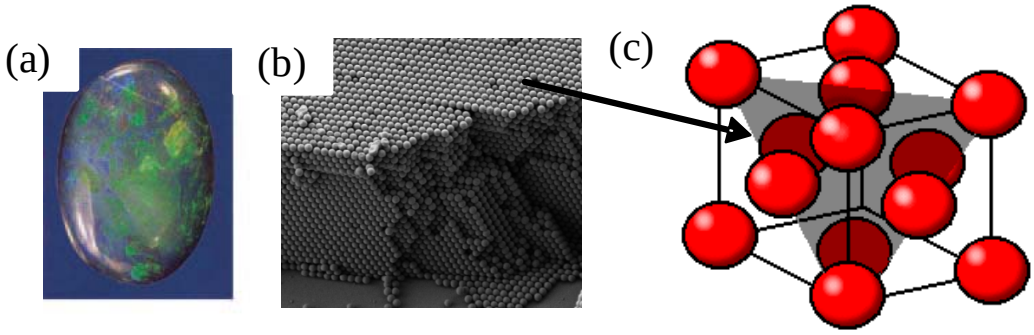

Figure10: a) A natural opal. b) SEM image of the opal nanostructure, which is responsible for the color effects by interference. c)The fcc lattice used for the description of the nanostructure lattice.

Their optical properties change dramatically from milky to transparent when water soaks into the open pores. However, opals never have the so called CPBG, which is a central property of PCs.[6] Inverse opals can, however, exhibit this important property.[34] With a complete band gap, opal-related systems can have all the basic PC properties. Artificial opals are also fabricated in various forms. The mechanism of synthesis and their optical properties are discussed in the second chapter of this thesis.

1.7 Fabrication methods

Generally, 1D PCs are prepared by layer-by-layer deposition of alternating materials using molecular beam epitaxy,[35] rf sputtering,[36] spin coating[37] etc. These methods allow thin film stacks to be prepared on substrates larger than the area of few tens of mm^2. Dielectric mirrors (Bragg reflector) and interference filters were actually the first (1D) PCs. However, they usually are not referred to as crystals because the name crystal is normally reserved for 2D or 3D structures. A stop gap in a desired spectral range can then be achieved by appropriately adjusting the dielectric contrast and the thickness ratios of the alternating layers.[7]

Lithographic methods, which use well developed techniques from the field of microelctronics were the first ones to yield structures predicted to have a band gap in the near IR region.[38,39,40] Electro-chemical etching[41] used to be a common top-down method to fabricate 2D periodic structures at the early age of PBG structure development. This method was able to etch porous materials with nano-scale holes with nice order and high aspect ratio, yielding perfect 2D PBG structures: dielectric constant change in the two dimensions and good uniformity along the third direction. An obvious disadvantage is that it is limited to 2D structures. Few reports were devoted to the fabrication of 3D PBG structures with the electro-chemical etching method.[42]

But efficient micro-fabrication of 3D photonic band gap microstructures, especially at a large-scale has been a scientific challenge over the past decade. So far, a number of fabrication techniques have been employed to produce sub-micron 3D PCs or templates. They include: conventional multilayer stacking of woodpile structures by using semiconductor fabrication processes,[43] colloidal self-assembly,[44] and multi-photon direct laser writing.[45]

Among them, colloidal crystals offer a starting point for the fabrication of periodic dielectric materials created through self-assembly. Here, one has the potential to create samples with full three-dimensional ordering, a feature important for engineering larger and more complete photonic band gaps. Also, self-assembly methods[46] can create thicker materials than those made using lithography. In addition, self-assembly methods are not limited in their length scale, and it is feasible to create materials that are active in the far infrared and even the near UV range using colloids with smaller diameters. Finally, as has been demonstrated recently, colloidal crystals provide an ideal scaffold for the creation of both polymeric and inorganic samples with complex porous structures.[47,48,49,50] Such samples may exhibit more CPBG than silica-air crystals as higher RICs are possible; in addition, they also may find applications in catalysis and separation technologies. A popular

method for creating colloidal crystals is the gravity sedimentation of colloids from dispersions.[49,51,52] Recent progress in the area has focused on strategies for strengthening the crystals and generating sample formats well suited for optical testing. In one method silica colloids were crystallized between parallel plates, and the solvent was then polymerized so as to trap their crystalline order. In another work, silica colloids were crystallized in capillaries, and the solvent was allowed to evaporate. The resulting silica-air structures have strong diffractive properties, and transmission spectra can be collected over some regions. Gravity-sedimented samples generally contain polycrystalline domains of unknown sizes. Other methods for ordering colloids into arrays have been explored by investigators seeking to make dense monolayer films of close-packed colloids for non-optical applications. Under the right conditions, colloid solutions that are spun-coated onto surfaces provide high quality monolayers. Convective self-assembly of wetting solutions is also a route for making ordered monolayers and structures of nanocrystals on a variety of substrates. Another method applied to polymer colloids uses the flow of solvent through micromachined channels to create dense colloidal arrays of multiple layers. Finally, recent work by Nagayama et al.[53,54] has exploited capillary forces to drive the assembly of larger ($D > 1$ μm) polystyrene colloids on flat surfaces. This method, which is conceptually similar to the Langmuir-Blodgett methods for film deposition, creates ordered monolayer films on nearly any vertical surface. Under the appropriate solvent and colloid conditions Nagayama et al.[53,54] showed that patches of bi- and tri-layer arrays could also be formed. All these methods have the advantage of producing well-ordered films on planar surfaces quite rapidly; however, in most instances the deposition techniques have been optimized for the formation of monolayer films. Jiang et al.[44] used a self-assembly technique which relies on capillary forces to organize colloids to fabricate colloidal crystal multilayers. These arrays are ordered over long (1 mm) length scales and can be fabricated with thicknesses ranging from two layers to several hundred layers. Moreover, the thickness of the resulting sample can be precisely dictated through control of sphere

size and concentration in solution. This deposition behavior can be adequately simulated using existing models of film formation developed for monolayer samples. The vertical deposition method of crystallization of colloidal crystals, as introduced by Jiang et al.,[44] will be used to prepare colloidal crystal alloys of various volume fraction compositions.

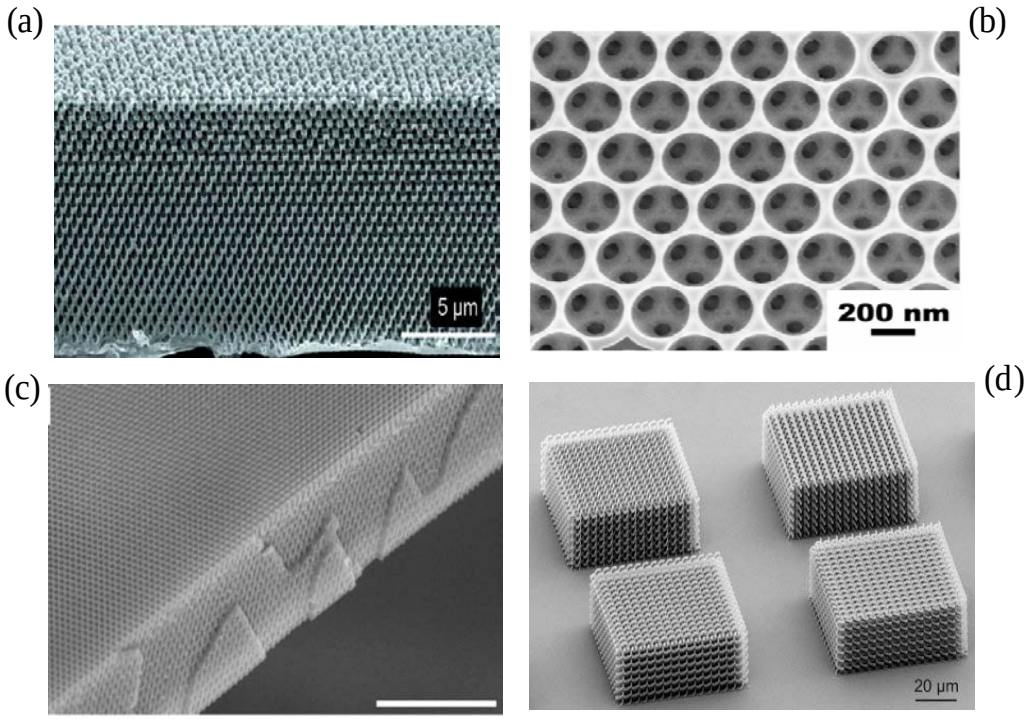

Figure 11: 3D PC structures fabricated by a) lithography, b) self assembly and further processing to obtain an inverse silica opal c) holographic lithography and d) laser direct writing. (Images have been adapted from references 36, 71, 53 and 43, respectively.)

Holographic method,[55] which utilizes the interference between two or more coherent light waves to produce a periodic intensity pattern, have been used to produce a periodic photo produced photonic structure in a resin (photo resist). Here, the initial laser beam is split into several beams and allowed to overlap in the resin at angles predetermined by the desired periodicity. This fabrication method yields samples of good quality in a reduced time (typically few hours), and in principle does not require expensive equipment besides a laser, polymer and some basic optics. The disadvantage of this method is high RIC PCs may not be achieved as the

photo resist polymer materials, do not posses high refractive index like any other Si or semiconductors materials.

1.8 Applications

As mentioned, PCs are expected to have a number of applications in optoelectronics and photonics.[56,57] They are mainly based on the modification (suppression) of spontaneous emission and localization of light. In optical industries, 1D PC are already in widespread use in the form of thin-film optics[58] with applications ranging from low and high reflection coatings on lenses and mirrors to color changing paints and inks.

Higher dimensional PCs are of great interest for both fundamental and applied research, and the 2D ones are beginning to find commercial applications. The first commercial products involving two-dimensionally periodic PCs are already available in the form of photonic crystal fibers (PCFs),[59] which use a micron scale structure to confine light with radically different characteristics compared to conventional optical fiber for applications in nonlinear devices and guiding exotic wavelengths. The losses of hollow core PCFs are falling dramatically. Researchers from Corning reported 13 dB/km at 1.55 μm wavelength – which is an improvement of almost two orders of magnitude within one year. Taking into consideration greatly reduced signal degradation, 100 times lower nonlinearities than current fibers and almost perfect control of chromatic dispersion. PCFs are supposed to become an interesting alternative to standard optical fibers in the future.[60] The 3D counterparts are still far from commercialization but offer additional features possibly leading to new device concepts like optical computers,[61] when some technological aspects such as manufacturability and principal difficulties such as disorder are under control.

A PC also provides the prospect of designing optical micro- and nanocavities by introducing appropriate point defects into it.[62] Furthermore, an extended defect such as line defect will work as a light waveguide.[63] There is a wealth of proposed applications relating to this principle of functioning including linear waveguide,[63]

bendings,[64] crossings, splitting,[65,66] junctions, add-drop filters,[67] etc. All the devices in this category can direct the flow of light as electrons are directed by conductive wires. These waveguides can be made to bend through sharp corners without energy loss since scattering loss is prohibited by the nature of the PBG structures. Waveguides in a 2D PBG structures have been studied extensively. A commercial PBG fiber is basically a 2D PBG waveguide in cylindrical coordinates.

True PBG behaviour at visible wavelengths also promises real advantages for light emitting devices. Applications include ultra-compact, low threshold lasers,[12,68] smart lenses,[69] nonlinear optical materials,[70] single mode LEDs,[71] sensors,[72,73] random lasing[74] and many more. For a recent overview one can see the references 47 and 70.

The existence of full and complete, non-polarization dependent PBG in 3D PCs gives rise to a number of peculiar optical properties useful for photonic engineering. Most important, the fabrication of 3D PCs with a complete PBG in visible and near IR regimes remains a great challenge.

1.9 Organization of the thesis

Chapter 2 is devoted for the discussion on details of various experimental techniques that carried out in this dissertation.

Chapter 3 discusses mainly the fabrication of polystyrene opals and their angle dependant transmission and reflection characteristics.

Chapter 4 involves the study of transmission spectral characteristics of different high Miller index Bragg planes with the incorporation of different alcohols and their effect on microspheres.

Chapter 5 is dedicated to the investigation of non linear optical absorption of polystyrene PCs with Z-scan technique using pico second pulses. The enhancement in the nonlinear absorption is observed when the wavelength of the pump beam falls

at the stop band edge of (111) Bragg plane and the possible mechanism was discussed.

Chapter 6 presents a simple method to enhance the surface electromagnetic fields by incorporating chemically prepared silver nanoparticles into the lattice of polystyrene opal. Along with this a simple method of in-situ formation of silver nanoparticles (through micro-Raman spectroscopy) with low power continuous wave laser irradiation in a polymer matrix was investigated as an alternate route to diffuse nanoparticles in the opal and inverse opal structures.

Chapter 7 summarizes the results obtained in this dissertation work and future implications and perspective are discussed in brief.

1.10 References

1. Rayleigh, Lord XVII. On the maintenance of vibrations by forces of double frequency, and on the propagation of waves through a medium endowed with a periodic structure. *Philosophical Magazine Series 5* **24**, 145–159 (1887).
2. Bykov, V. P. Spontaneous emission from a medium with a band spectrum. *Soviet Journal of Quantum Electronics* **4**, 861–871 (1975).
3. Yablonovitch, E. Inhibited Spontaneous Emission in Solid-State Physics and Electronics. *Phys. Rev. Lett.* **58**, 2059–2062 (1987).
4. John, S. Strong localization of photons in certain disordered dielectric superlattices. *Phys. Rev. Lett.* **58**, 2486–2489 (1987).
5. Photonic Crystals: Semiconductors of Light. at <http://www.sciamdigital.com/index.cfm?fa=Products.ViewIssuePreview&ARTICLEID_CHAR=6394F751-8AA0-4232-95DE-DCBE90CB3B7>
6. Joannopoulos, J. D. *Photonic Crystals: Molding The Flow Of Light*. (Princeton University Press: 2008).
7. Yeh, P. *Optical waves in layered media*. (Wiley: 2005).
8. Ho, K. M., Chan, C. T. & Soukoulis, C. M. Existence of a photonic gap in periodic dielectric structures. *Phys. Rev. Lett.* **65**, 3152–3155 (1990).
9. Kittel, C. *Introduction To Solid State Physics*. (Wiley: 2005).
10. Ashcroft, N. W. & Mermin, N. D. *Solid state physics*. (Holt, Rinehart and Winston: 1976).
11. Noda, S., Fujita, M. & Asano, T. Spontaneous-emission control by photonic crystals and nanocavities. *Nature Photonics* **1**, 449–458 (2007).
12. Ryu, H.-Y., Kwon, S.-H., Lee, Y.-J., Lee, Y.-H. & Kim, J.-S. Very-low-threshold photonic band-edge lasers from free-standing triangular photonic crystal slabs. *Appl. Phys. Lett.* **80**, 3476–3478 (2002).
13. Yablonovitch, E. Photonic Crystals. *Journal of Modern Optics* **41**, 173–194 (1994).
14. Li, Z.-Y. & Zhang, Z.-Q. Fragility of photonic band gaps in inverse-opal photonic crystals. *Phys. Rev. B* **62**, 1516–1519 (2000).

15. Li, Z.-Y., Zhang, X. & Zhang, Z.-Q. Disordered photonic crystals understood by a perturbation formalism. *Phys. Rev. B* **61**, 15738–15748 (2000).
16. Yablonovitch, E., Gmitter, T. J. & Leung, K. M. Photonic band structure: The face-centered-cubic case employing nonspherical atoms. *Phys. Rev. Lett.* **67**, 2295–2298 (1991).
17. Skorobogatiy, M. & Yang, J. *Fundamentals of Photonic Crystal Guiding*. (Cambridge University Press: 2009).
18. Kosaka, H. *et al.* Superprism phenomena in photonic crystals. *Phys. Rev. B* **58**, R10096–R10099 (1998).
19. *Low-Dimensional Semiconductor Structures: Fundamentals and Device Applications*. (Cambridge University Press: 2001).
20. Lourtioz, J.-M. *et al. Photonic Crystals: Towards Nanoscale Photonic Devices*. (Springer: 1999).
21. Sakoda, K. *Optical Properties of Photonic Crystals*. (Springer: 2001).
22. Notomi, M. *et al.* Extremely Large Group-Velocity Dispersion of Line-Defect Waveguides in Photonic Crystal Slabs. *Phys. Rev. Lett.* **87**, 253902 (2001).
23. Gersen, H. *et al.* Real-Space Observation of Ultraslow Light in Photonic Crystal Waveguides. *Phys. Rev. Lett.* **94**, 073903 (2005).
24. Vlasov, Y. A., O'Boyle, M., Hamann, H. F. & McNab, S. J. Active control of slow light on a chip with photonic crystal waveguides. *Nature* **438**, 65–69 (2005).
25. Soljačić, M. & Joannopoulos, J. D. Enhancement of nonlinear effects using photonic crystals. *Nature Materials* **3**, 211–219 (2004).
26. Marlow, F., Muldarisnur, Sharifi, P., Brinkmann, R. & Mendive, C. Opals: Status and Prospects. *Angewandte Chemie International Edition* **48**, 6212–6233 (2009).
27. Kalceff, M. A. S., Phillips, M. R., Moon, A. R. & Smallwood, A. Cathodoluminescence microanalysis of natural hydrated amorphous SiO₂; opal. *Physics and Chemistry of Minerals* **24**, 131–138 (1997).
28. Gaillou, E. *et al.* The geochemistry of gem opals as evidence of their origin. *Ore Geology Reviews* **34**, 113–126 (2008).
29. Eckert, A. W. *The World of Opals*. (Wiley: 1997).
30. Raman, C. & Jayaraman, A. The structure and optical behaviour of iridescent opal. *Proceedings Mathematical Sciences* **38**, 343–354 (1953).
31. Sanders, J. V. Colour of Precious Opal. , *Published online: 19 December 1964; | doi:10.1038/2041151a0* **204**, 1151–1153 (1964).
32. Sanders, J. V. Diffraction of light by opals. *Acta Crystallographica Section A* **24**, 427–434 (1968).
33. Darragh, P. J., Gaskin, A. J., Terrell, B. C. & Sanders, J. V. Origin of Precious Opal. , *Published online: 01 January 1966; | doi:10.1038/209013a0* **209**, 13–16 (1966).
34. Sözüer, H. S., Haus, J. W. & Inguva, R. Photonic bands: Convergence problems with the plane-wave method. *Phys. Rev. B* **45**, 13962–13972 (1992).
35. Herman, M. A. & Sitter, H. *Molecular Beam Epitaxy: Fundamentals and Current Status*. (Springer: 1996).
36. Chiasera, A. *et al.* High quality factor Er3+-activated dielectric microcavity fabricated by rf sputtering. *Applied Physics Letters* **89**, 171910–171910–3 (2006).
37. Katouf, R., Komikado, T., Itoh, M., Yatagai, T. & Umegaki, S. Ultra-fast optical switches using 1D polymeric photonic crystals. *Photonics and Nanostructures - Fundamentals and Applications* **3**, 116–119 (2005).
38. Shir, D. *et al.* Three dimensional silicon photonic crystals fabricated by two photon phase mask lithography. *Applied Physics Letters* **94**, 011101–011101–3 (2009).
39. Lin, S. Y. *et al.* A three-dimensional photonic crystal operating at infrared wavelengths. *Nature* **394**, 251–253 (1998).
40. Noda, S., Tomoda, K., Yamamoto, N. & Chutinan, A. Full Three-Dimensional Photonic Bandgap Crystals at Near-Infrared Wavelengths. *Science* **289**, 604–606 (2000).
41. Wehrspohn, R. b. & Schilling, J. Electrochemically Prepared Pore Arrays for Photonic-Crystal Applications. *MRS Bulletin* **26**, 623–626 (2001).

42. Trifonov, T., Marsal, L. F., Rodríguez, A., Pallarès, J. & Alcubilla, R. Fabrication of two- and three-dimensional photonic crystals by electrochemical etching of silicon. *physica status solidi (c)* **2**, 3104–3107 (2005).
43. Ho, K. M., Chan, C. T., Soukoulis, C. M., Biswas, R. & Sigalas, M. Photonic band gaps in three dimensions: New layer-by-layer periodic structures. *Solid State Communications* **89**, 413–416 (1994).
44. Jiang, P., Bertone, J. F., Hwang, K. S. & Colvin, V. L. Single-Crystal Colloidal Multilayers of Controlled Thickness. *Chem. Mater.* **11**, 2132–2140 (1999).
45. Deubel, M. *et al.* Direct laser writing of three-dimensional photonic-crystal templates for telecommunications. *Nature Materials* **3**, 444–447 (2004).
46. Norris, D. J. & Vlasov, Y. A. Chemical Approaches to Three-Dimensional Semiconductor Photonic Crystals. *Advanced Materials* **13**, 371–376 (2001).
47. Tarhan, İ. İ. & Watson, G. H. Photonic Band Structure of fcc Colloidal Crystals. *Phys. Rev. Lett.* **76**, 315–318 (1996).
48. Vos, W. L. *et al.* Strong effects of photonic band structures on the diffraction of colloidal crystals. *Phys. Rev. B* **53**, 16231–16235 (1996).
49. Míguez, H. *et al.* Control of the Photonic Crystal Properties of fcc-Packed Submicrometer SiO2 Spheres by Sintering. *Advanced Materials* **10**, 480–483 (1999).
50. López, C. Materials Aspects of Photonic Crystals. *Advanced Materials* **15**, 1679–1704 (2003).
51. Míguez, H. *et al.* Evidence of FCC Crystallization of SiO2 Nanospheres. *Langmuir* **13**, 6009–6011 (1997).
52. Rogach, O. . *et al.* Self-organization of uniform silica globules into the three-dimensional superlattice of artificial opals. *Materials Science and Engineering: B* **64**, 64–67 (1999).
53. Denkov, N. *et al.* Mechanism of formation of two-dimensional crystals from latex particles on substrates. *Langmuir* **8**, 3183–3190 (1992).
54. Dimitrov, A. S. & Nagayama, K. Continuous Convective Assembling of Fine Particles into Two-Dimensional Arrays on Solid Surfaces. *Langmuir* **12**, 1303–1311 (1996).
55. Campbell, M., Sharp, D. N., Harrison, M. T., Denning, R. G. & Turberfield, A. J. Fabrication of photonic crystals for the visible spectrum by holographic lithography. *Nature* **404**, 53–56 (2000).
56. Joannopoulos, J. D., Villeneuve, P. R. & Fan, S. Photonic crystals: putting a new twist on light. , *Published online: 13 March 1997; | doi:10.1038/386143a0* **386**, 143–149 (1997).
57. Galisteo-López, J. F. *et al.* Self-Assembled Photonic Structures. *Advanced Materials* **23**, 30–69 (2010).
58. Povey, I. M. *et al.* Photonic crystal thin films of GaAs prepared by atomic layer deposition. *Applied Physics Letters* **89**, 104103–104103–3 (2006).
59. Knight, J. C., Birks, T. A., Russel, P. S. J. & Atkin, D. M. All-silica single-mode optical fiber with photonic crystal cladding. *Opt. Lett.* **21**, 1547–1549 (1996).
60. Graydon, O. Researchers report photonic crystal fibers with record low-loss operating at telecoms wavelengths. at <http://optics.org/articles/news/8/9/18/1, 2002)>
61. Nishimura, N., Awatsuji, Y. & Kubota, T. Two-dimensional arrangement of spatial patterns representing numerical data in input images for effective use of hardware resources in digital optical computing system based on optical array logic. *Journal of Parallel and Distributed Computing* **64**, 1027–1040 (2004).
62. Qi, M. *et al.* A three-dimensional optical photonic crystal with designed point defects. *Nature* **429**, 538–542 (2004).
63. Adibi, A., Lee, R. K., Xu, Y., Yariv, A. & Scherer, A. Design of photonic crystal optical waveguides with singlemode propagation in the photonic bandgap. *Electronics Letters* **36**, 1376 (2000).
64. Lin, S.-Y., Chow, E., Hietala, V., Villeneuve, P. R. & Joannopoulos, J. D. Experimental Demonstration of Guiding and Bending of Electromagnetic Waves in a Photonic Crystal. *Science* **282**, 274–276 (1998).

65. Schonbrun, E. et al. Polarization beam splitter based on a photonic crystal heterostructure. *Opt. Lett.* **31**, 3104–3106 (2006).
66. Liu, T., Zakharian, A. R., Fallahi, M., Moloney, J. V. & Mansuripur, M. Design of a compact photonic-crystal-based polarizing beam splitter. *Photonics Technology Letters, IEEE* **17**, 1435 – 1437 (2005).
67. Douay, M. *et al.* FORMATION OF BRAGG GRATINGS IN GERMANIUM DOPED OPTICAL FIBERS USING A PRISM INTERFEROMETER. *Le Journal de Physique IV* **01**, C7–529–C7–532 (1991).
68. Colombelli, R. *et al.* Quantum Cascade Surface-Emitting Photonic Crystal Laser. *Science* **302**, 1374–1377 (2003).
69. Parimi, P. V., Lu, W. T., Vodo, P. & Sridhar, S. Photonic crystals: Imaging by flat lens using negative refraction. *Nature* **426**, 404–404 (2003).
70. Slusher, R. E. & Eggleton, B. J. *Nonlinear Photonic Crystals*. (Springer: 2003).
71. Wierer, J. J., David, A. & Megens, M. M. III-nitride photonic-crystal light-emitting diodes with high extraction efficiency. *Nature Photonics* **3**, 163–169 (2009).
72. Holtz, J. H. & Asher, S. A. Polymerized colloidal crystal hydrogel films as intelligent chemical sensing materials. *Nature* **389**, 829–832 (1997).
73. Khoo, I. C. *et al.* Liquid-Crystals for Tunable Photonic Crystals, Frequency Selective Surfaces and Negative Index Material Development. *Molecular Crystals and Liquid Crystals* **453**, 309–319 (2006).
74. Soukoulis, C. M. *Photonic Crystals and Light Localization in the 21st Century*. (Springer: 2001).

CHAPTER 2

Abstract

We describe here briefly the experimental facilities that were used for the characterization of the photonic crystals and the nonlinear optical studies. We briefly described the commercial setups such as JASCO spectrophotometer, micro-Raman spectrometer and the field emission scanning electron microscope, as these instruments were used very extensively in our study. A modified Z-scan setup suitable for the nonlinear absorption studies of photonic crystals is described.

Experimental details and techniques

2.1 Transmission/Reflection spectrophotometer

The transmission and reflection optical characteristics are carried out using a commercial Ultra Violet-Visible- Near Infrared (UV-Vis-NIR) double-beam spectrophotometer (JASCO V-670). The spectrophotometer uses two lights sources, a deuterium (D_2) lamp for ultraviolet region and a halogen lamp for visible and near infrared region. It utilizes a unique, single monochromator design covering a wavelength range from 190 to 2700 nm. The monochromator features dual gratings: 1200 grooves/mm for the UV/Vis region; 300 grooves/mm for the NIR region. A PMT detector is provided for the UV/VIS region and a Peltier-cooled lead sulphide (PbS) detector is employed for the NIR region. Both gratings and detector are automatically exchanged within the user selectable 750 to 900 nm range.

The light from the source lamp gets reflected from mirror 1 and beam passes through slit 1(S_1) and hits a diffraction grating. The grating can be rotated allowing for a specific wavelength to be selected. At any specific orientation of the grating, only monochromatic (single wavelength) beam successfully passes through slit 2 (S_2). A filter (F) is used to remove unwanted higher order diffraction beam. The light beam hits a second mirror (M_2) before it gets split by a half mirror (M_3) (half of the light is reflected, the other half gets transmitted). One of the beams is allowed to pass through a reference sample (air in the present case), the other passes through the sample. The intensities of the light beams are then measured at the end as shown in figure 1. The photometer computes the ratio of the sample signal to the reference signal (I/I_o) to obtain the transmittance.

The spectrometer is provided with three different measurement accessories: 1) variable angle transmittance, 2) fixed angle and 3) variable angle reflectance. The

schematic of the beam path in the spectrometer is shown in the figure 1. The optical path of the fixed angle (5°) reflectance measurement accessory in the path of the sample beam is presented in figure 1b. We have used an aluminum mirror for standard reference.

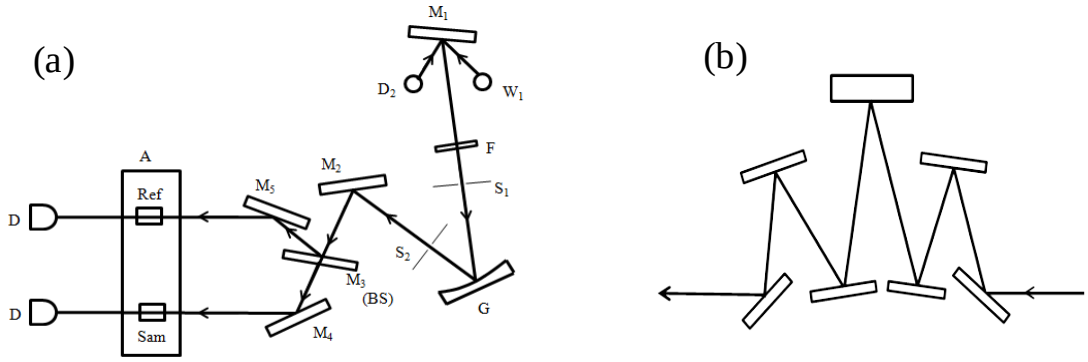

Figure 1: Schematic of the optical setup of the commercial JASCO spectrometer for a) transmission and b) fixed angle (5°) reflection geometry. W1: Halogen lamp, D_2: Deuterium lamp, S: Slit, F: filter, G: grating, BS: Beam splitter, M: Mirror, A: Accessory, Sam: Sample, Ref: Reference beam, D: Detector.

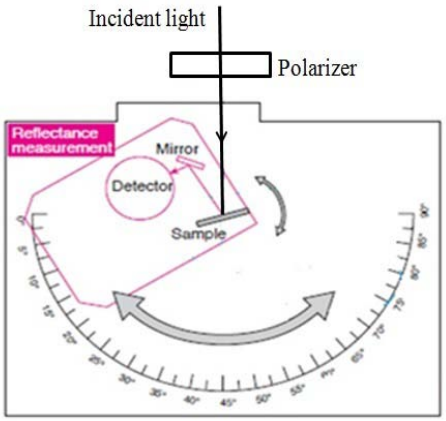

Figure 2: Schematic of the beam path of the absolute reflectance measurement accessory for JASCO spectrometer.

The polarization dependent studies are carried out in the reflection geometry and their spectral characteristics are compared with s-, p- and unpolarized light. The schematic of the absolute reflectance measurement accessory is shown in figure 2. The sample, reflecting mirror and detector are mounted on a single rotational stage.

Absolute reflectance is measured by rotating this stage to determine the angle of the light incident upon the sample. The detector is equipped with an integrating sphere and thus it permits measurement of the relative reflectance of a diffusely reflecting sample. The polarization of the beam is selected using Glan-Taylor prism polarizer. This accessory allows recording the reflectance from 5-70° only.

2.2 Field Emission-Scanning Electron Microscopy (FESEM)

The scanning electron microscopy is a versatile technique that reveals detailed information about the morphology and the composition of natural and manufactured materials.

The wavelength of electrons accelerated by a voltage U is given by the well known de Broglie wavelength:

$$\lambda = h/\sqrt{2m_0 eU} \quad (1)$$

in the non-relativistic case, which is a good approximation for voltages below 100 kV. Here h is Plank's constant, m_0 the rest-mass of electrons and e the elementary charge. The corresponding wavelength ranges from 38 pm for 1 keV electrons to 7 pm for 30 keV electrons.

Due to the short de Broglie wavelength of electrons in comparison to visible light, the SEM offers a much better resolution which is not diffraction limited in comparison to optical microscopes. Whereas the resolution of optical microscopes is limited by the wavelength of the light used (it is ~ 200 nm at λ=500 nm), the resolution in modern SEMs is limited by lens aberrations. Recent efforts to compensate these errors using magnetic correction lenses resulted in resolutions better than 0.1 nm.[1,2,3] The routinely used standard SEM which raster a focused electron beam across a sample surface, provide high- spatial resolutions down to several nm.

A field-emission SEM provides narrower probing beams at low as well as high electron energy, resulting in both improved spatial resolution and minimized sample charging and damage. There are two classes of emission source: thermionic emitter

and field emitter. Emitter type is the main difference between the Scanning Electron Microscope (SEM) and the Field Emission Scanning Electron Microscope (FESEM). Thermionic Emitters use electrical current to heat up a filament; the two most common materials used for filaments are Tungsten (W) and Lanthanun Hexaboride (LaB6). When the heat is enough to overcome the work function of the filament material, the electrons can escape from the material itself. Thermionic sources have relative low brightness, evaporation of cathode material and thermal drift during operation. Field Emission is one way of generating electrons that avoids these problems.

A Field Emission Gun (FEG); also called a cold cathode field emitter, does not heat the filament. The emission is reached by placing the filament in a huge electrical potential gradient. The FEG is usually a wire of Tungsten (W) fashioned into a sharp point. The significance of the small tip radius (~ 100 nm) is that an electric field can be concentrated to an extreme level, becoming so large to exceed the work function of the material and electrons leave the cathode. FESEM uses Field Emission Gun producing a cleaner image, less electrostatic distortions and spatial resolution < 2 nm (that means 3 or 6 times better than SEM). The images formed by the field emission scanning electron microscope are from secondary electrons, backscattered electrons, characteristic X-rays, Auger electrons and others that are emitted by the sample. Figure 3 represents the schematic diagram of field emission scanning electron microscopy.

A field emission gun is a type of electron gun in which a sharply-pointed Schottky-type emitter is held at several kilovolts negative potential relative to a nearby electrode, so that there is sufficient potential gradient at the emitter surface to cause field electron emission. Schottky type emitter is a thermal field emitter (TFE) cathode, in which thermionic emission is enhanced by barrier lowering in the presence of a high electric field. Schottky emitters are made by coating a tungsten tip

with a layer of zirconium oxide. A high energy (typically 10-30 keV) electron beam, emitted from a tungsten tip is focused to a spot size of 1 nm to 5 nm by the

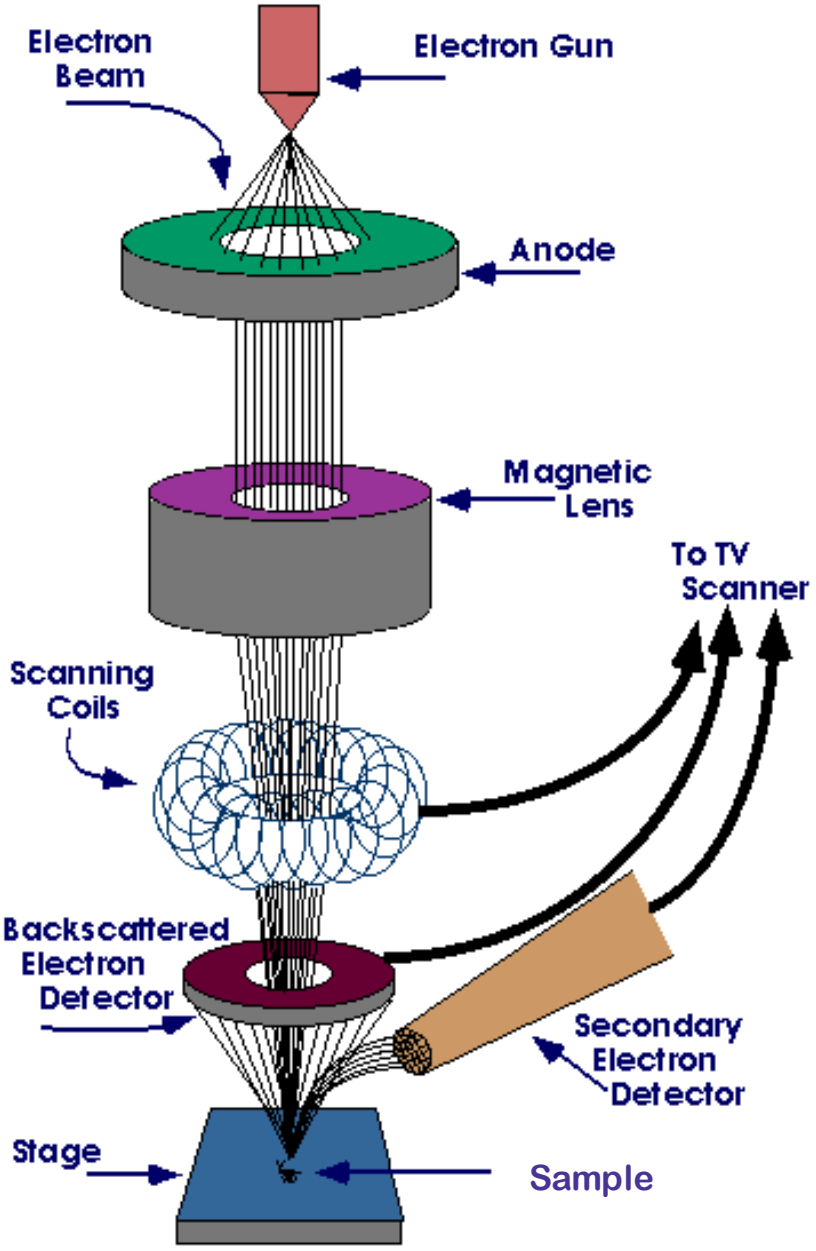

Figure 3: Schematic diagram of field emission scanning electron microscopy.

condenser magnetic lenses. The focused beam passes through a pair of scanning coils, which raster the beam across the surface. The incident electrons cause low energy secondary electrons generation. The secondary electrons emitted from the sample are detected by a scintillator-photomultiplier device and the resulting signal is rendered into a two-dimensional intensity distribution that can be viewed and saved as a digital image. The most common imaging mode monitors low energy (<50 eV) secondary electrons which originates within a few nanometers from the surface.

There are the high-energy electrons which are elastically scattered and essentially possess the same energy as the incident electrons called as back scattered electrons. The probability of backscattering increases with the atomic number Z of the sample material. Back scatter electrons are used to detect contrast between areas with different chemical compositions. Because these electrons are emitted from a depth in the sample, the resolution in the image is not as good as for secondary electrons.

2.3 Z-scan

The Z-scan technique is a single beam technique, which allows the determination of the real and imaginary parts of the third order susceptibility[4]. This technique is a simple, sensitive, single beam method that uses the principle of spatial beam distortion to measure both the sign and the magnitude of refractive nonlinearities of optical materials. The experiment uses a Gaussian beam from a laser in tight focus geometry to measure the transmittance of a nonlinear medium through a finite aperture in the far field as a function of the sample position Z, from the focal plane. In addition to this, the sample transmittance without an aperture (or fully opening the aperture to allow the transmitted beam after the sample to detector as shown in figure 4) is also measured to extract complementary information about the absorptive nonlinearities of the sample.

2.3.1 Open-aperture Z-scan for nonlinear absorption

The presence of multi-photon (two or more) absorption suppresses light at higher intensities, while saturation of absorption produces the opposite effect. The sensitivity of the experiment to refractive nonlinearities is entirely due to the aperture. The removal of the aperture will make the Z-scan sensitive to absorptive nonlinearities alone. Thus by doing the Z-scan with and without aperture both the refractive and absorptive nonlinearities of the sample can be studied. The schematic of an open aperture Z-scan is as shown in figure 4. Spatially filtered input beam is focused using a lens. The sample is scanned across the focus using a stepper motor. The transmitted light is then collected using another lens (large area) of f ~ 100 mm and fast photodiode (FND100). The data collected by the detector D_1 is divided with the data obtained from D_2 in order to reduce the error from the fluctuations in the power level of laser beam. Different neutral density filters are used for attenuation to ensure that the photodiode does not get saturated.

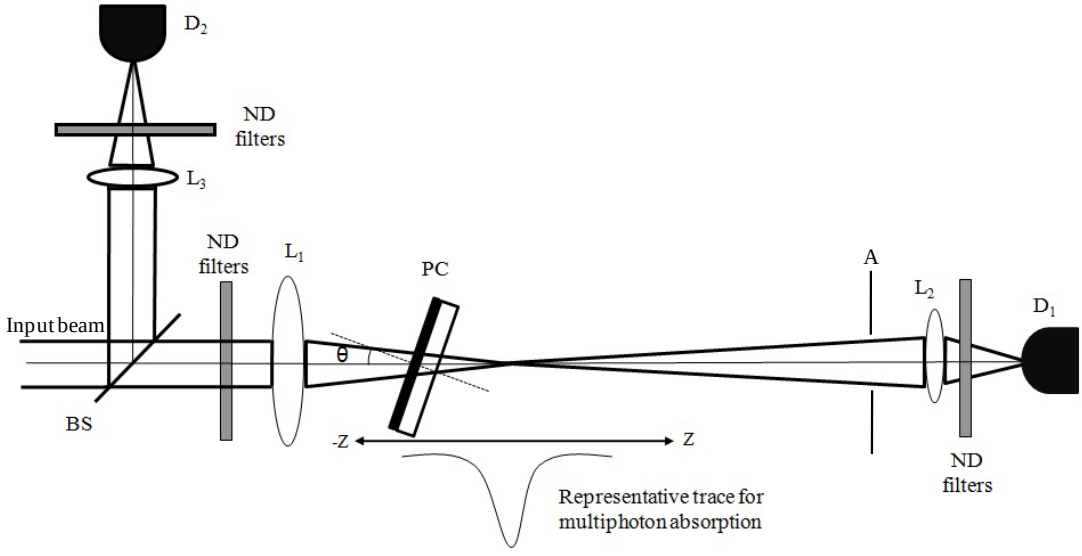

Figure 4: Schematic of open aperture Z-scan experimental setup. L: Lens, D: Detector, BS: Beam splitter, ND filters: Neutral density filters, A: Aperture, PC: Photonic crystal on a glass plate. Dotted and thin lines represent the normal to photonic crystal structure and optic axis.

The translation stage with stepper motor is used to move the sample under investigation along the Z-axis of the laser beam during the experiment. The stepper motor driver is the interface between the computer and the stepper motor on the translation stage. It controls the movement of the stepper motor based on the commands from the computer. A program in C++ language was developed to control the motion of the stepper motor and for data collection. An oscilloscope is used to inspect the signal form detectors and the boxcar integrators visually. This allows the adjustments on the boxcar average to ensure correct overlap of the boxcar's gate and signals from the large area photodiodes. This output from the boxcars can also be checked to ensure that the data acquisition card is not saturated or damaged.

2.4 Micro-Raman spectrometer

Raman spectroscopy is a light scattering technique, and can be thought of in its simplest form as a process where a photon of light interacts with a molecule in the sample to produce scattered radiation of different frequencies. If frequency of scattered photon is less than the incident photon, then it is known as Stokes scattering. If frequency of scattered photon is greater than the incident photon then it is called anti-Stokes scattering. Raman spectroscopy is extremely information rich, for example it is useful for chemical identification, characterization of molecular structures, effects of bonding, environment and stress on a sample.

In Raman experiments, the sample is irradiated with monochromatic light and the scattered light is traditionally observed at right angles to the incident radiation. However, in modern confocal Raman microscopes, the scattered signals are recollected by a microscope objective in 180° geometry. Selection of appropriate light source for micro-Raman spectroscopy is of great importance because the Raman signals are usually much weaker than the excitation intensity. For strong scattering material only one Raman scattered photon can be explored for every 10^7 incident photon. Further a coherent light source (laser) is preferred due to its high power, monochromatic and collimated beam nature. The most commonly used

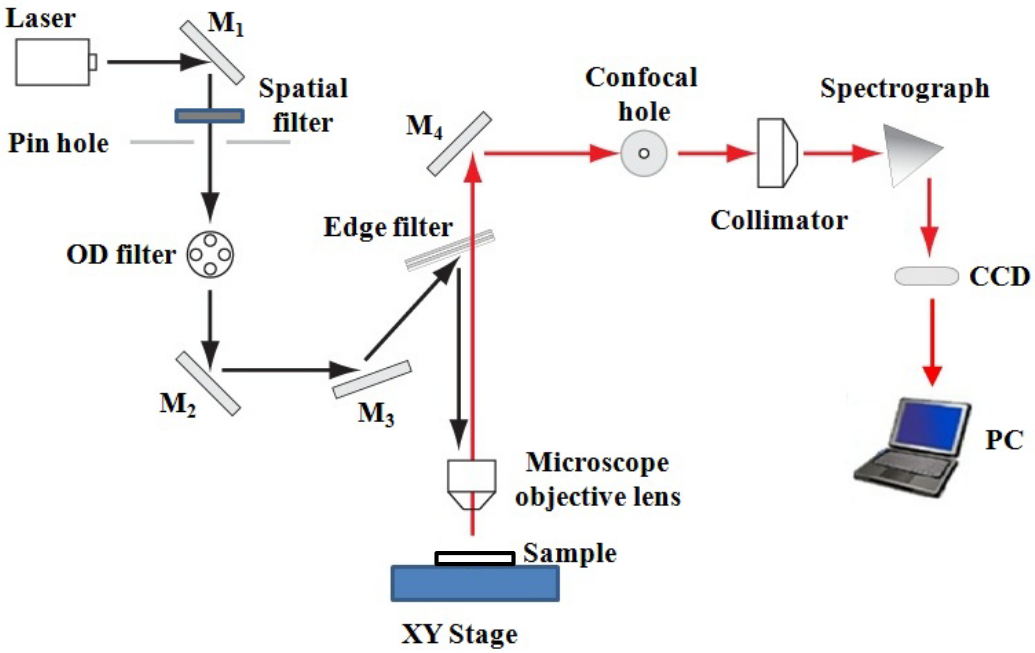

Figure. 5: Schematic of a micro-Raman spectrometer.

laser sources in Raman applications are He-Ne, Ar^+ ion and diode lasers delivering at 632.8, 514.5 and 785 nm respectively.

In the present work Raman scattering measurements were performed with a LabRAM HR800 micro-Raman spectrometer manufactured by HORIBA Jobin Yvon. It includes a variety of optical components arranged as illustrated in Figure 5. A collimated laser beam is sequentially passed through several optical components including the spatial filter, optical density filters, an edge filter which serves as a dichroic mirror, and the microscope objective lens which focuses the beam on the core sample. An automated x-y motorized stage allows moving the sample to acquire Raman spectra at each position. The scattered radiation emanating from the sample is collected through the same objective lens and is passed through the edge filter for elimination of the excitation line. A controllable slit and a confocal hole are used before the Raman radiation reaches the spectrograph. The spectrograph utilizes two gratings with 600 and 1800 lines/mm. The spectrograph focuses the scattered wavelength spectrum on a CCD camera. All these optical components are controlled

through a graphical user interface on a computer attached to the system. A brief description of optical components such as filters, confocal hole, CCD and calibration of micro Raman spectrometer are provided in the following paragraphs.

Parts description

Filters: There are several holographic filters or wavelength selectors used throughout the laser path. At first, a narrow band-pass filter (interference/absorption filter) is placed in between a source and a sample to isolate a single exciting line. Another most important filter used in the Raman spectrometer is an edge filter. This serves as both dielectric mirror, which reflects the pump to the sample and as a high pass filter, which eliminates the excitation line prior to passing it to the spectrograph. It transmits less than 0.5% of the backscattered laser line while allows more than 90% of the remaining frequencies to reach the detector. The drop off is at 50 cm^{-1}.

Confocal hole: Confocal optics means that the sample is illuminated with diffraction limited spot and that the illuminating spot is imaged on an ideally point-like detector. Practically, the point-like detector is realized with an adjustable pinhole called ‘confocal hole’ in front of the real detector (hole placed at the spectrograph entrance). The advantage of confocal sampling is a considerable reduction of the depth of focus and thus an increased Z discrimination. For example, this means that a confocal microscope allows separating the signal from each layer of a laminar/multilayer sample, or isolating the signal from an inclusion against the signal coming from the surrounding medium. The smaller the confocal hole, the faster is the drop of the Raman signal as one goes out from focus. In our experiment we have used a confocal hole of 300 µm.

CCD: CCD (charged coupled device) camera has rectangular two dimensional arrays of pixels (standard 1024×256 pixels, pixel size = 26 µm × 26 µm) that convert the light falling to each pixel into a charge, which is proportional to the integrated light intensity. Raman signal after passing through slit is focused on CCD

after being separated by the diffraction grating into discrete wavelengths, where each frequency is measured simultaneously. Photoelectrons are created in the CCD upon exposure to the scattered beam. The dispersed beam is spread vertically across horizontal lines of pixels, which are summed. Data acquisition was then obtained from computer by using the Labspec software. This software allows the user to set the spectral range for the spectrum, exposure time of the CCD and read-out the spectrum appears on the computer screen which can be stored and manipulated.

Calibration: In order to have the maximum accuracy in the frequency of Raman signal careful calibration is required. For this purpose we use the crystalline Si wafer throughout the measurements. Si is used for calibration in our case because it exhibits strong first-order Raman signal at around 520.5 cm^{-1}.[5] The excitation energies used for Raman measurements were greater than the bandgap energy of the silicon so the laser light is strongly absorbed in the upper layer of Si thus making it ideal for the alignment of spectrometer optics which is required on the occasion.

2.5 Modified Bragg's law

The modified Bragg's law[6] which is a combination of Bragg and Snell's law allows knowing the central wavelengths of stop bands of close packed fcc opals at each incident angle. When modeling the diffraction of light by a periodic medium as a layered structure as shown in figure 7a, one computes the phase difference accumulated by rays that suffer scattering from different planes in the stack and add up those with a multiple of 2π (constructive interference). To arrive at a simplified picture for deriving the Bragg formula, we assume the region where the PS spheres are in contact as n_{high} region. As one goes to midway between these regions, the air gap increases leading to n_{low}. Therefore figure 7b is taken as two layers with high refractive index reflection occurring at these layers. However since the medium in between these layers contains both PS and air, for simplicity we have taken the refractive index between the layers as n_{eff} which is the effective refractive of close packed fcc structure. By considering an equivalent thin film of thickness similar to

that of interplanar distance of (111) planar array as shown in figure 7a, the path difference (ΔS) between rays R_2 and R_1 (which comes from the two consecutive layers of (111) planes of fcc structure) that interact with two media of different refractive indices, n_{air} and n_{eff} can be calculated as below.

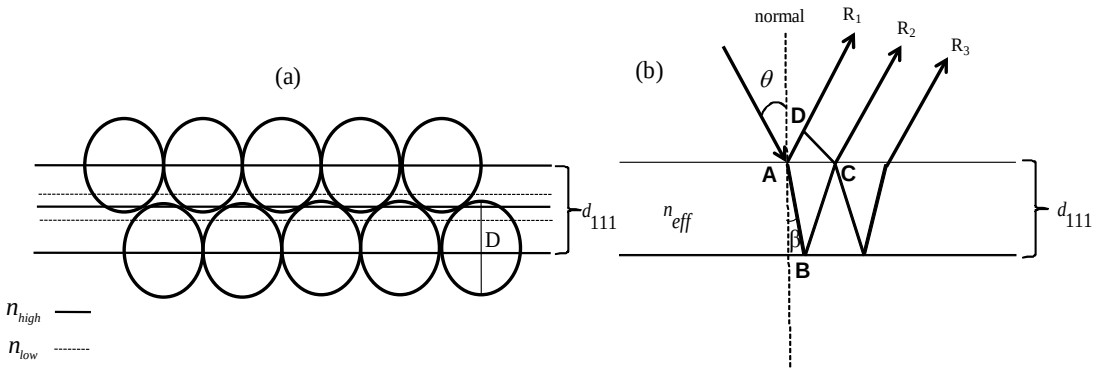

Figure 7: Schematic for a) parallel arrays of (111) plane of close packed fcc structure and b) reflected and refracted wave combination for interference in the equivalent film of thickness d_{111}.

$$\Delta S = 2n_{eff}\overline{AB} - n_{air}\overline{AD} \quad (2)$$

Here, the effective refactive index (n_{eff}) of the close packed fcc structure can be defined as below.

$$n_{eff}^2 = f_{PS}n_{PS}^2 + f_{air}n_{air}^2 \quad (3)$$

where f_{PS} and f_{air} are volume fractions of PS microsphere and air; n_{PS} and n_{air} are refractive indices of PS and air respectively. The values for f_{PS} and f_{air} can be taken as 0.74 and 0.26 based on the perfect close packed fcc structure of identical particles respectively. The path difference ΔS can be expressed in terms of d_{111} and θ from figure 7b.

$$\Delta S = 2n_{eff}\left(\frac{d_{111}}{cos\theta}\right) - n_0\left[\left(\frac{d_{111}}{cos\theta}\right)\frac{n_0}{n_{eff}}\sin^2\theta\right] \quad (4)$$

where, d_{111} is the inter-planar spacing of (111) planes. For (111) planes, d_{111}=0.816D, where D is the diameter of the PS sphere.

Using Snell's law

$$n_0 sin\theta = n_{eff} sin\beta \quad (5)$$

and trigonometric relationships, we obtain upon substitution of equation 5 into equation 4:

$$\Delta S = 2n_{eff}\, d_{111}\sqrt{1-\frac{n_0^2}{n_{eff}^2}sin^2\theta} \quad (6)$$

The phase difference δ between the two paths is $\delta = (2\pi/\lambda)\Delta S$.

For constructive interference $\delta = 2m\pi$ and then $m\lambda = \Delta S$, where m is the order of refelction for which interference occurs and λ is the light wavelength,

$$m\lambda = 2d_{111}\sqrt{n_{eff}^2 - n_0^2 sin^2\theta} \quad (7)$$

Using the above equation 7, the basic parameters of interplanar spacing of (111) plane (d_{111}) and effective refractive index (n_{eff}) of PC structure can be evaluated and details are given in the next chapter.

2.6 References

1. Haider, M., Uhlemann, S., Schwan, E., Rose, H., Kabius B. & Urban, K. *Electron microscopy image enhanced.* Nature 392, 768-769 (1998)
2. Batson, P.E., Dellby, N., & Krivanek, O.L. *Sub-Ångstrom resolution using aberration corrected electron optics.* Nature **418**, 617 - 620 (2002)
3. Sheik-Bahae, M., Said, A.A., Wei, T.H., Hagan, D.J. & Van Stryland, E.W. *Sensitive measurement of optical nonlinearities using a single beam. IEEE Journal of Quantum Electronics* **QE-26**, 760-769 (1990).
4. Balkanshki, M., Wallis, R. F., & Haro, E. *Anharmonic effects in light scattering due to optical phonons in silicon.* Phy. Rev. B **28,** 1928-1934 (1983).
5. Goldstein, J., Newbury, D., Joy, D., Lyman, Ch., Echlin, P., Lifshin, E., Sawyer, L., & Michael, J. *Scanning electron microscopy and x-ray microanalysis* Springer (2003)
6. Aguirre, C. I., Reguera, E. & Stein, A. *Tunable Colors in Opals and Inverse Opal Photonic Crystals.* Advanced Functional Materials 20, 2565–2578 (2010).
7. JASCO Inc. operation manuals for UV-vis-NIR spectrophotometer.
8. Horiba Jobin Yvon manuals for micro-Raman spectrometer.

CHAPTER 3

Abstract

Different sizes of polystyrene microspheres were synthesized through emulsion polymerization method and 3D colloidal photonic crystals were grown using vertical deposition method. By analyzing the stop band features due to different Bragg planes using transmission and reflection spectral characteristics, important parameters such as interplanar spacing for diffrent Bragg palnes, effective refractive index and thickness of these colloidal photonic crystals were calculated. The study of polarization dependant reflection spectral characteristics due to (111) Bragg plane was also carried out.

Fabrication and optical characterization of 3D colloidal photonic crystals

3.1 Introduction

In recent years, interest in the synthesis of colloidal microsphers such as silica or polymer has grown markedly in order to fabricate 2D or 3D photonic crystal (PC) structures under ambient conditions and explore their photonic applications.[1] The colloidal crystals made out of the microsphers typically in the range of 150-500 nm lead to a band gap in the visible region. The position and width of the band gap of resulting PCs are determined mainly by the effective refractive index and refractive index contrast of the constituent materials of the PC. More the refractive index contrast, wider will be the band gap of PCs. Among the colloidal microspheres of silica, poly(methyl methacrylate) (PMMA) and polystyrene (PS), PS has highest refractive index and hence, it is chosen to fabricate colloidal structures and their characterization. Even though some sizes of the PS microspheres are available commercially, the stop band of those colloidal PC structures is not desirable to our studies; hence we synthesized different sizes of microspheres for fabricating colloidal PC structures that produce stop gaps which meet our requirements.

According to literature, the first studies on these colloidal PCs were focused on the first order Bragg-diffraction due to (111) plane. Lopez et al.[2] have studied the transmission spectral characteristics along the LU and LK paths of the first Brillouin zone (BZ) using un-polarized light. Many people have used polarized light to study the diffraction effects due to different planes in the PS,[3,4] poly(methyl methacrylate) (PMMA)[5,6] and silica[7,8] opals. It has become challenging debate for the explanation of Bragg planes other than in the optical spectra of 3D opals. Un-polarized light consist of all components, so one would get the information of all Bragg planes whereas in case of polarized light, p-polarization couples to PCs very weakly

compared to s-polarization.[7] So in this work, we have used an un-polarized light to study the transmission spectral characteristics by rotating the 3D PS PC in clock-wise (CW) and anti clock-wise (ACW) directions placing the PC grown on a glass substrate vertically. If the transmission spectral characteristics of PCs don't have sharp band edges and steeper band gap depths then there would be problem in identifying the features for a particular Bragg plane at the lower wavelength region. Schutzmann et al.[4] have not discussed about the Bragg planes even though they observe planes whose features are more prominent in the LK path. In the current chapter, we present the data with all Bragg planes that exist in the LU and LK paths with better quality. The clearly distinguishable stop band in the transmission spectrum with increasing angle of incidence due to different planes resemble the band gaps obtained with the hetero structure PCs, where by multi band gaps can be achieved.[9] Some of the basic parameters of these PC parameters like effective refractive index, inter-planar spacing and thickness are investigated using the angle dependent transmission spectra. To exploit the effect of thickness on band width of the stop band due to (111) plane, the transmission experimental data at normal incidence is compared with the scalar-wave approximation. Finally, the chapter is concluded by summarizing some important issues regarding polarization properties of these colloidal PCs.

3.2 Synthesis of polystyrene microspheres

3.2.1Emulsion polymerization

Emulsion polymerization or a variation of this, such as micro-, miniemulsion, emulsifier-free, or dispersion polymerization have been well investigated to synthesize colloidal polymer particles consisting of PS or PMMA.[10,11] Among these methods, emulsifier free emulsion polymerization[12] yields different sizes of highly monodisperse microspheres that have average diameter in the range from 180 - 350

nm with the polydispersity of < 5%. The classic emulsion polymerization involves the following procedure.

The monomer emulsion is made up of water-immiscible monomer droplets stabilized by surfactant molecules, empty micelles (colloidal surfactant vesicles) and monomer-swollen micelles. Water-insoluble monomers are dispersed into water with a small amount of a surfactant, in this case sodium 4-styrenesulfonate. The monomer droplets can range in size from less than 1 μm to 10 μm. A water-soluble initiator, in this case potassium persulfate, which has a weak peroxide bond, forms radicals when heated, and these radicals initiate chain reaction polymerization of the monomers in the water. Polymer chains grow in the water and are either trapped by surfactant micelles, which then become the primary polymer particles, or polymer chains aggregate to form primary particles. The size of the primary particles is probably only 10-20 nm diameter. The primary particles swell with monomers. After the primary particles have formed, all further polymerization increases the size but not the number of particles. Growth continues until all of the monomer is consumed. As polymerization proceeds, the monomer droplets decrease in size and eventually disappear. When the polymer particles become large, the surfactant molecules in the micelles suspend the polymer particles. Final particle diameters typically are 50-500 nm, depending on all of the possible variables in the experimental procedure. The particles are stabilized electrostatically against coagulation in water by the ionic sulfonate groups on their surface. A fraction of the sodium counter ions of the sulfonate groups dissociate in water, leaving the particles negatively charged. The nonpolar PS resides in the core of the particles to avoid water. A high concentration of ionic groups on the particle surface increases colloidal stability. The polymerization can be carried out in one or more stages of addition of monomers. The physical character of the final polymer depends on the temperature of reaction, the formulation and the manipulation of the reaction conditions, such as when and how much of the ingredients are added to the reactor. Required chemicals and the

brief procedure to synthesize different sizes of PS microspheres are outlined in the following section.

Materials: Styrene, procured from Merck, Germany was washed with 10% sodium hydroxide solution using separating funnel three times in order to remove the antipolymerizer. Sodium styrene sulfonate, sodium hydrogen carbonate and potassium persulfate of Sigma-Aldrich make were used without further purification.

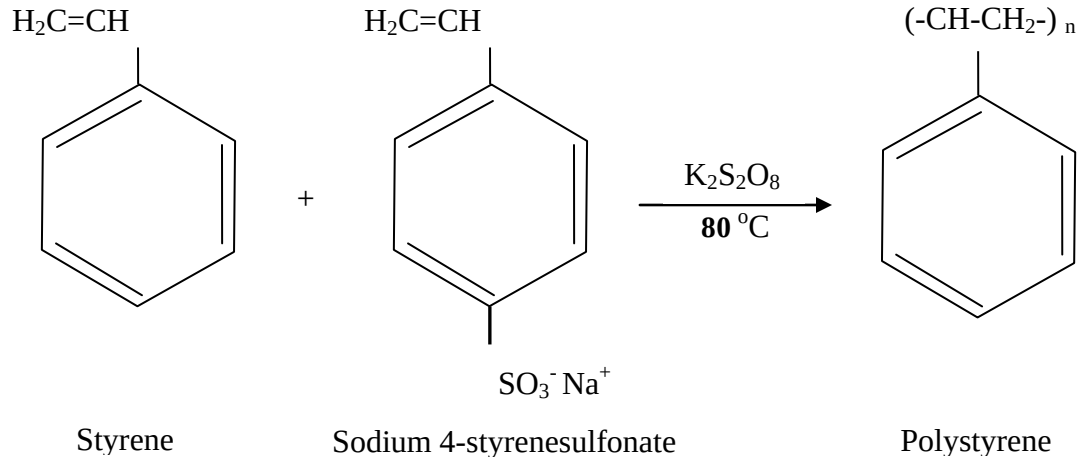

Figure 1: Chemical equation for emulsion polymerization.

To synthesize monodisperse PS microspheres, 225 ml of deionized water was poured into 500 ml of four-neck round bottom flask, kept at 80±4 ^{o}C with constant stirring at 350 ± 10 rpm. 15 mg of sodium styrene sulfonate as emulsifier and 125 mg of sodium hydrogen carbonate as buffer were added to the water. After 10 min, 28 ml of styrene was added to the solution. One hr later, 125 mg of potassium persulfate was added and the polymerization was performed under argon atmosphere for nearly 20 hrs. A chemical equation which represents the polymerization reaction is shown in figure 1. The solution was filtered with glass wool in order to remove agglomerations. Again, the solution was centrifuged three times at 10,000 rpm for one hour and re-dispersed in water and stored at 4 ^{o}C. These microspheres are highly stable for more than a year. The average diameter of micropsheres formed through

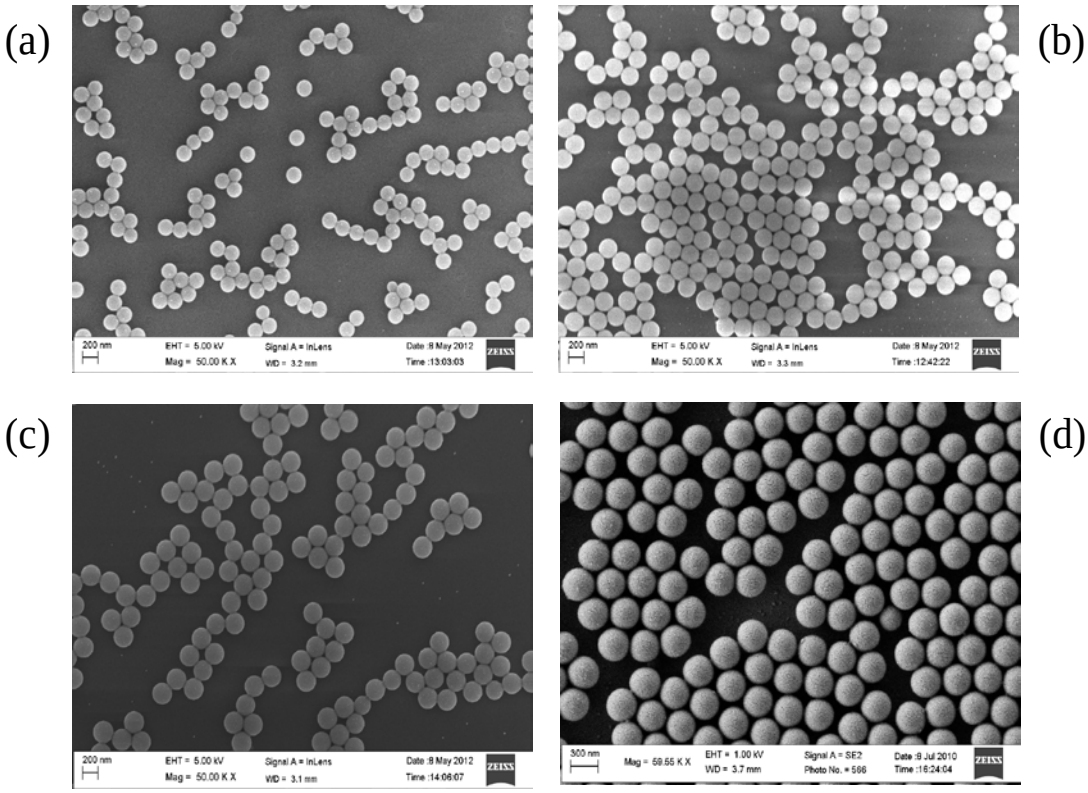

Figure 2: Different sizes of PS microspheres of diameter a) D = 186 nm, b) 225 nm, c) 260 nm and d) 331 nm. The relative standard deviation is <5% for all microspheres.

this recipe was 186 nm. By changing only the weight of emulsifier and remaining all the weights of the reactants same (using the same temperature), different sized

Table 1: Weights of reactants to synthesize PS microspheres of different sizes. Same temperature and stirring speed is maintained for all reactions.

DI water (ml)	Sodium styrene sulfonate (mg)	Sodium hydrogen carbonate (mg)	Styrene (ml)	Potassium persulfate (mg)	Temp (°C)	Avg. diameter (nm) D
225	15	125	28	125	80	186
225	25	125	28	125	80	226
225	50	125	28	125	80	260
225	75	125	28	125	80	331

microspheres were synthesized whose averages sizes are tabulated in table 1. A very dilute concentration of the solution of microspheres was spin coated on a glass plate to estimate the average size and their relative standard deviation from field emission scanning election microscope (FESEM) micrographs. The FESEM micrographs of different sizes of microspheres are shown in figure 2. The relative standard deviation is estimated by taking the sizes of 100 particles and found that it is less than 5% for all sizes in our present study.

3.3 Vertical deposition method

In the present work, we have undertaken the task of fabricating colloidal crystal structures that produce stop bands in the visible region so as to explore the novel optical characteristics of these structures which will be discussed mainly in the chapter 4. Hence, we have selected only D = 226, 260 and 331 nm microspheres to fabricate PCs. There are variety of bottom-up approaches to fabricate 3D colloidal PCs such as gravity sedimentation,[13] centrifugation,[14] electrophoresis,[15] vertical deposition,[16] horizontal deposition,[17] controlled drying, [18,19] etc.[1] All these methods work on the unique process of self-assembly. Among these methods, vertical deposition is widely accepted due to low cost and rapid production. Moreover, this method has gained great interest because it does not require any special training and is highly reproducible without generating major cracks.

In a typical procedure of vertical deposition method, a flat glass substrate of dimensions 6×1.5 cm^2 was bathed in a mixture containing concentrated sulfuric acid and hydrogen peroxide (3:1, volume ratio) over night in order to make it hydrophilic. The substrate is then washed ultrasonically with deionized water and dried. It was kept in a vial containing aqueous solution of PS microspheres. Then the vial was kept in a vibration-free temperature controlled oven (Incucenter, Cole-Parmer) at 50 ^{o}C. The relative humidity was maintained around 55-60%.

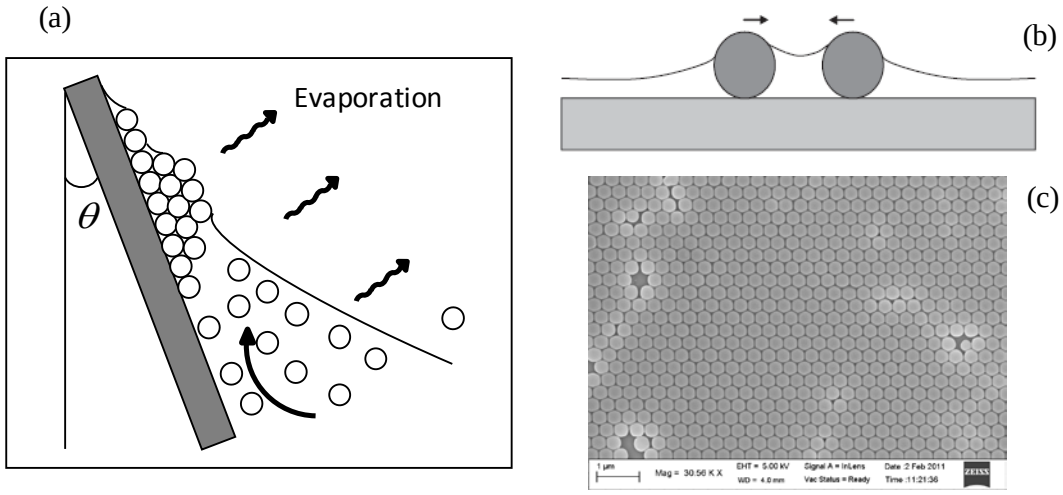

Figure 3: a) Schematic diagram for the formation of multilayers at the meniscus. b) Lateral capillary forces can arise when colloidal spheres are partially immersed in a thin layer of liquid. Such forces can cause an attractive interaction between two spheres. c) A single layer of PS colloidal spheres.

Although extensively used for more than a decade now, the crystal formation is not completely understood to the present date.[20] Due to the hydrophilic nature of the substrate a meniscus is formed where the substrate, air and liquid meet as shown in figure 3a. Crystal growth begins at the point where the meniscus thickness is less than the diameter of the sphere. Menisci formed between two spheres, which are pulled towards the substrate and attracted to each other by lateral capillary forces, organize them into close-packed monolayer array. During evaporation, solvent flow towards the meniscus region drags spheres towards meniscus to form monolayer. A close packed monolayer of colloidal microspheres is observed as depicted in figure 3c when the solution contains 0.1% (weight percent) of PS microspheres. However, under the appropriate conditions like concentration of solution, wettability of the substrate, temperature and humidity, more than one layer may begin to grow at the meniscus. Without altering the temperature and humidity, a weight percent of PS microspheres around 1- 2 yield a multilayer structure as displayed in figures 4 and 5.

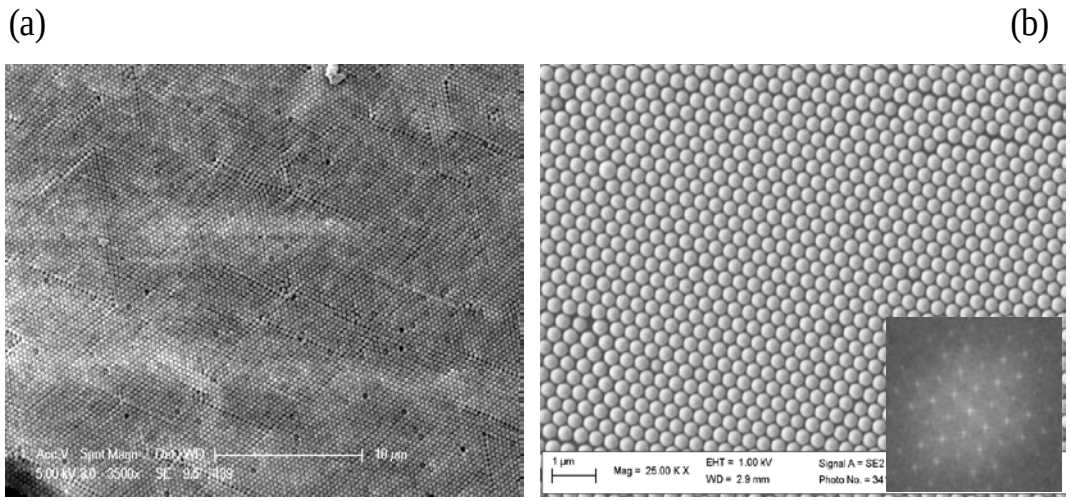

Figure 4: Surface morphology of (111) Bragg plane of D = 331 nm PS PC with different magnifications. a) scale bar 10µm and b) scale bar = 1µm. Inset of (b) shows the FFT (fast Fourier transform) image.

These conditions were kept constant to grow the multilayer structures using various diameters. During the formation of multilayers, planar arrays of spheres can be arranged as either ABCABC… (face centered cubic (fcc)) or ABAB… (hexagonal close packed (hcp) structure). However, computer simulations performed by Woodcock[21] showed that the stacking of hard spheres in a fcc structure is more stable than that in a hcp structure by an amount of Gibbs free energy of 0.005RT per mol, which corresponds to $\Delta G = 0.13$ meV per particle. In the self-assembly process, (111) plane of fcc structure grows parallel to glass substrate and this is confirmed through FESEM picture as shown in figures 4a and 4b. Inset of figure 4b shows the FFT (Fast Fourier Transform) image. Moreover the cross sectional FESEM pictures of our samples did not show any rectangular alignment with one sphere in the center and four spheres at the corners, that is typical of hcp stacking. Other than (111) plane, few planes such as (200) and $(\bar{1}11)$ can be seen in the cross sectional view of FESEM pictures as presented in figure 5. Some of the experimental results[13,22,23,24] have proved that these planar arrays formed into close packed fcc structure only. The experimentally measured single domain area of PC is larger than 50 × 50 µm using

the optical microscope images. The PC prepared with other diameters also show similar results.

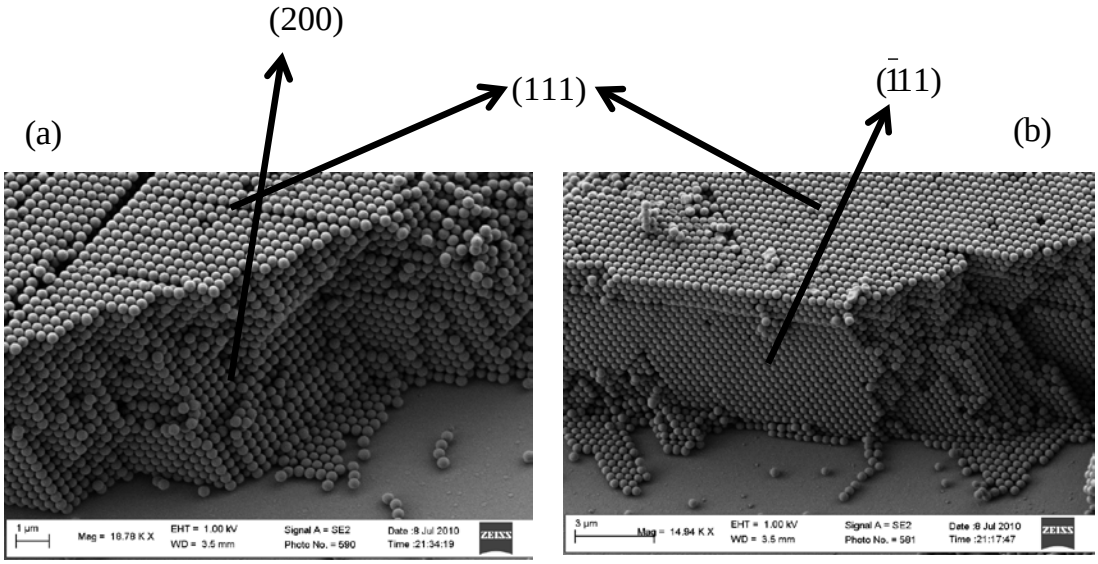

Figure 5: (a) and (b) represent the FESEM images recorded in the cross sectional view. Arrows indicate the (111), $(\bar{1}11)$ *and (200) planes of fcc structure.*

3.4 Optical Characterization

The transmission and reflection optical characteristics are carried out using UV-vis-NIR double-beam spectrophotometer (JASCO V-670). In the transmission geometry, the beam dimensions are 1×6 mm^2 at normal incidence and the fixed angle reflection geometry presents the circular beam with the diameter of 2 mm. The transmission and reflection spectra at normal and near normal incidence for D = 226, 260 and 331 nm PCs are shown in figures 6a and 6b, respectively. These spectra show around 50% of light attenuation with their maximum transmission losses at 531 nm, 612 nm and 771 nm, respectively.

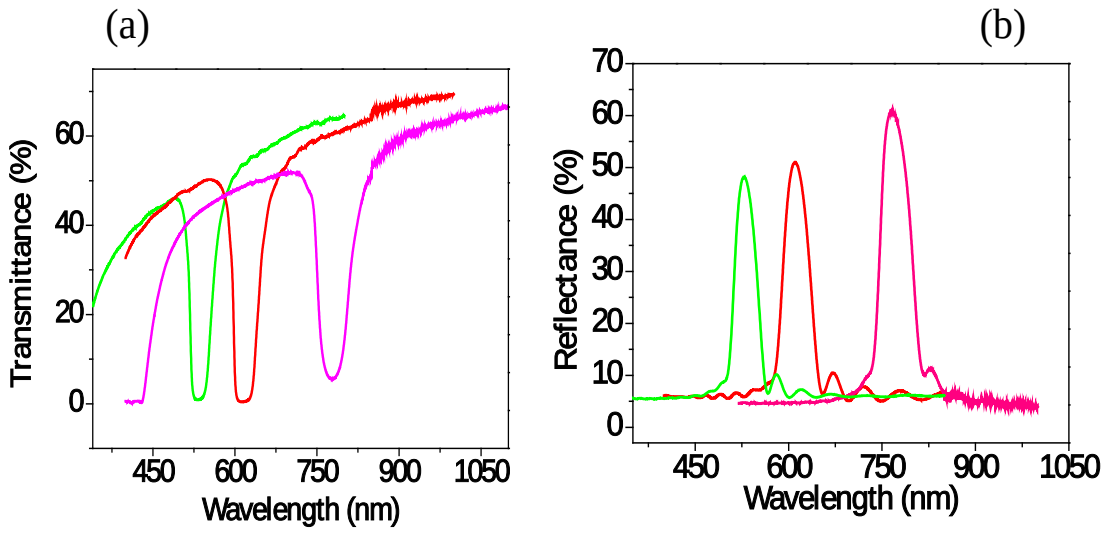

Figure 6: a) Transmission and b) reflection spectra of D = 226 nm (green), 260 nm (red) and 331 nm (pink) PS PC recorded at $\theta=5^0$ with the Bragg-peaks at 531 nm, 612 nm and 771 nm respectively. The small oscillations on either side of the stop band indicate the Fabry-Perot fringes.

3.5 Thickness measurement

The Fabry-Perot fringes on either side of the stop band can be observed in both transmission and reflection spectra as shown in figure 6 and these oscillations are due to the interference of light reflected from the top and bottom surface of the PC film. These fringes indicate the homogeneity of the thickness and effective refractive index of the PC within the illuminated area. The experimental spectra could be compared with the theoretical data to know the lattice parameters but calculating them from an analytical expression would be more appropriate in order to determine the quality of the PC. From the spectral separation of the Fabry-Perot fringes, the thickness of the sample can be quantified. The amplitude of local reflectance maxima due to the Fabry-Perot resonances will appear at[25]

$$m\lambda = 2hn_{eff} \quad (1)$$

For opals and inverse opals, the effective refractive index n_{eff} can be taken as

$$n_{eff}^2 = f_{PS} n_{PS}^2 + f_{air} n_{air}^2 \quad (2)$$

where f_{PS} and f_{air} are volume fractions of PS microsphere and air; n_{PS} and n_{air} are refractive indices of PS and air, respectively. The values for f_{PS} and f_{air} can be taken as 0.74 and 0.26 based on the perfect close packed fcc structure of identical particles and the refractive indices of PS and air are n_{PS}=1.59 and n_{air}=1, respectively.

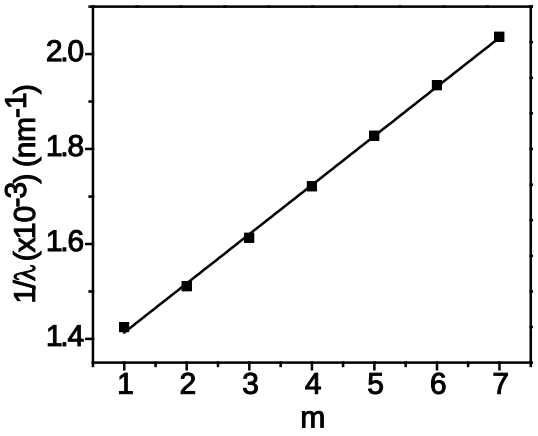

Figure 7: Plot of m versus 1/λ for D = 331 nm PS PC. Square symbol represents the experimental values and line represents the linear fit based on equation 1.

m (an integer) is the resonance order and h is the sample thickness. Plotting the inverse wavelength as a function of the resonance order, a linear relation is obtained. The plot of m versus 1/λ for D =331 nm PS PC is shown in figure 7. From the slope (=$1/2hn_{eff}$), the thickness of the sample can be calculated. For close packed fcc structure the thickness of the crystal is related to the number of layers N as follow.[26]

$$h(N) = D \times [(N-1) \times 0.816 + 1] \quad (3)$$

Thicknesses (h) and the number of layers of all PCs are given in the table 2.

Table 2: Calculated thickness and the corresponding number of layers for different sizes of PS PCs.

Diameter D (nm)	Thickness h (µm)	No. of layers N
226	4.2	23
260	6.13	29
331	6.3	23

3.6 Angle dependent spectral characteristics due to (111) stop band

As the (111) plane of the fcc structure is parallel to substrate, we measured the transmission spectrum by changing the external angle θ (it is measured with respect to the normal of the (111) plane) from 0 - 45° and found that the central wavelength of the stop band is changed from 532 - 468, 617 - 534, 771- 676 nm for D = 226, 260 and 331 nm diameter PCs as shown in Figure 8a-c.

The modified Bragg's law[27] which is a combination of Bragg and Snell's law allows knowing the central wavelengths of the stop band due to (111) plane at each incident angle.

$$m\lambda = 2d_{111}\sqrt{n_{eff}^2 - n_0^2 sin^2\theta} \quad (4)$$

Here, d_{111} is the inter-planar spacing for (111) planes. For (111) planes $d_{111} = 0.816D$, where D is the diameter of the PS microspheres. n_{eff} is the effective refractive index and θ is the external angle between the incident wave and normal to the (111) plane.

The inter-planar spacing, thereby the diameter and effective refractive index can be calculated from the angle dependent transmission spectra as λ^2 will vary linearly with $\sin^2\theta$ from equation 4. The results are shown in figure 8d for D = 226 nm PS PC. The slope (= $-4d_{111}^2$) and intercept (= $4d_{111}^2 n_{eff}^2$) of $sin^2\theta$ versus λ^2 plot would

give the values of d_{111} for (111) plane and n_{eff}, respectively. The calculated diameter D using d_{111}=0.816D is in good agreement with the value obtained from

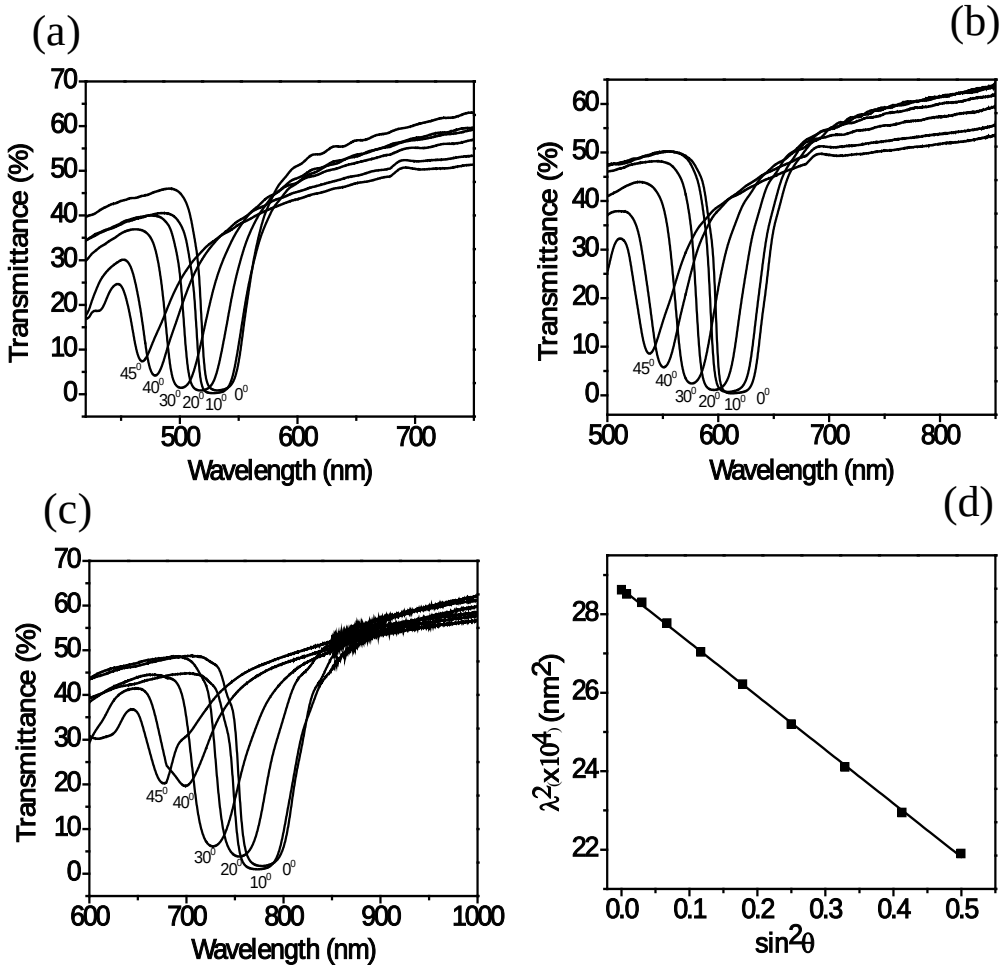

Figure 8: Angle dependent transmission spectra of a) D = 226 b) 260 and c) 331 nm PS PC. θ is changed from 0 - 45° in steps of 5°. d) Plot of λ^2 versus $sin^2\theta$ based on the Bragg diffraction formula for D = 226 nm PS PC (where λ is the central wavelength of the transmission spectrum and θ is angle of incidence). Square symbol represents the experimental values and line represents the linear fit based on equation 4.

FESEM pictures. From equation 2, n_{eff} can be calculated as 1.45 and this is in good agreement with the calculated value from the linear fit for all PCs. For D = 226 nm, 260 and 331 nm PS PCs, d_{111} and n_{eff} are given in table 3.

Table 3: Calculated effective refractive index and interplanar spacing of (111) plane for different sizes of PS PCs.

Calculated D (nm)	n_{eff}	d_{111} (nm)
226	1.45	184.88
260	1.45	212.57
331	1.43	271.14

Even though all these colloidal PCs are made out of same material, the shifting of (111) stop band in the range of 45° is different for different diameter PCs. The differences between the central wavelengths of the stop bands obtained at θ = 0 and 45° for D = 226, 260 and 331 nm diameter PCs are 64, 83 and 95 nm, respectively. Higher the diameter, larger will be the lattice constant and they diffract higher wavelengths compared to smaller diameter PCs.

3.7 Scalar-Wave Approximation (SWA)

In this study, we adopted the scalar-wave approximation[26,28] (SWA) which is a well known tool to analyze the beam-propagation characteristics in periodically varying dielectric structures. Unlike modified Bragg's law, SWA gives the full profile of stop band due to (111) plane and the results can be compared with the experimental data. In the SWA, the vector nature of the electromagnetic wave is ignored. This puts a limitation in analyzing the wave propagation along an arbitrary direction in a 3D crystal structure. As detailed by Shung and Tsai,[28] it is possible to solve the Maxwell equation for an electric field in a periodic medium, where the dielectric function is the sum of an average dielectric constant ε_0 and a periodic part ϵ'. The solutions of such a system depend on the sign of a function given by $F(\omega)$.

$$F(\omega) = \frac{G^2}{4} + \varepsilon_0 \times \left(\frac{\omega}{c}\right)^2 - \sqrt{G^2 \times \varepsilon_0 \times \left(\frac{\omega}{c}\right)^2 + U_G^2 \left(\frac{\omega}{c}\right)^4} \quad (5)$$

where G=2π/d_{111} is a reciprocal wave vector and U_G the corresponding Fourier coefficient in the Fourier development of the periodic function ϵ'.[28] When the system resulting from the Maxwell equations is resolved, nontrivial solutions with the following general expression are found:

$k = \frac{G}{2} \pm q$ for band region, where $F(\omega) \geq 0$

$k = \frac{G}{2} \pm iq$ for band region, where $F(\omega) \leq 0$

Where $q = \sqrt{F(\omega)}$

The final form of the equations for transmission rate for band and gap regions are obtained by applying the boundary conditions at the interface of the periodic dielectric structure.

For band regions

$$T = \frac{1}{1+(\kappa_b - 1)sin^2(kN d_{111})} \quad (6)$$

and for gap regions

$$T = \frac{1}{1+(\kappa_g + 1)sin^2(qN d_{111})} \quad (7)$$

where N and d_{111} are the number of layers and separation between the two successive (111) planes. Other constants κ_b, like κ_g, and etc. are analytic expressions depending on other parameters not described here (see reference 28 for more details). A MATLAB program is developed to compare the experimental data. Here we have chosen reflection spectra of D = 260 nm PCs obtained for two different thicknesses. We normalized the experimental and predicted data using proper conversion factors and compared their normalized absorbance spectra as shown in figures 9a and 9b. The values of inter-planar spacing (d_{111}) and effective refractive index (n_{eff}) that

were obtained with the linear fit of modified Bragg's law were given as input parameters. We adjusted only the parameter N to match the Fabry-Perot fringe positions as these fringes play a main role in determining thickness of the crystal. By fitting the experimental data with SWA, the thicknesses of the two crystals were found to be 17 and 35, respectively. The increased number of layers resulted in reduced FWHM (from 64 - 49 nm) and fringe spacing as demonstrated

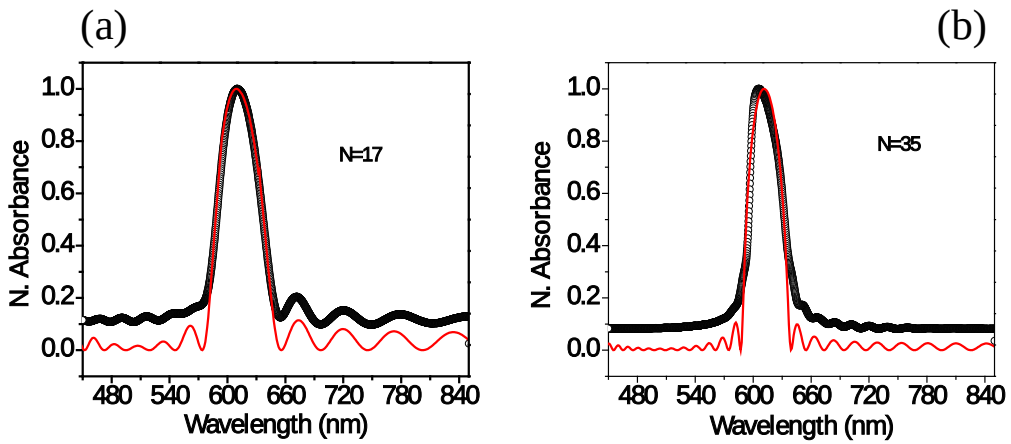

Figure 9**:** Comparison between experimental (circles) and simulated optical transmission spectra using SWA approximation (solid line) for D= 260 nm PS PC with different number of layers a) N=17 and b) N=35, respectively.

in figures 9a and 9b. Our results match well with those observed in the reference 29. The good agreement between the experimentally observed and theoretically predicted spectra gives evidence of superior quality of the crystals.

3.8 Spectral characteristics in the LU and LK path of the first Brillouin zone

Till now we have discussed only the diffraction due to (111) plane in order to calculate crystal parameters such as effective refractive index and inter planar distance. To explore the study of stop bands due to other planes we have chosen D = 331 nm PC and recorded the transmission spectral characteristics by changing the incident angle θ from 0 - 75° in both clock-wise (CW) and anti clock-wise (ACW)

directions by keeping the substrate vertically as shown in figure 10. The spectral range is 300 - 1000 nm. Here we have used the following equation to find Bragg resonances for other planes (hkl).[6]

$$\lambda_{hkl} = 2d_{hkl}n_{eff}\sqrt{1 - sin^2\left\{\beta - \arcsin\left(\frac{sin\theta}{n_{eff}}\right)\right\}} \quad (8)$$

Here d_{hkl} are the inter-planar spacing for (hkl) planes and β is the angle between the normals of (111) and any other (hkl) planes. θ is the external angle between the incident wave and normal to the (111) plane. In the shorter wavelength region the

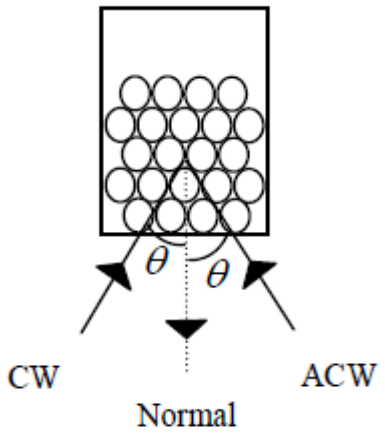

Figure 10: Schematic illustration of the incident light on the surface of the PC in the CW and ACW directions.

transmittance decreases drastically at normal incidence indicating that the Bragg diffraction is due to other planes and these planes are getting well resolved and they move to longer wavelength region with increasing θ as shown in figure 11. In CW (ACW) rotation of the sample from θ = 20 to 75°, a dip has appeared, represented by unfilled triangles (filled triangles), that shifts from 481 nm to 708 nm (525 nm to 710 nm) as shown in figure 11. These dips are coinciding with each other after $\theta = 50^0$ as shown in figure 11. By fitting the experimental data with the equation 8, it is found that the dips in CW direction agree with the $(\bar{1}11)$ plane and in ACW direction the data fits well with the (200) plane up to θ=50°. After θ =50° it again fits well with

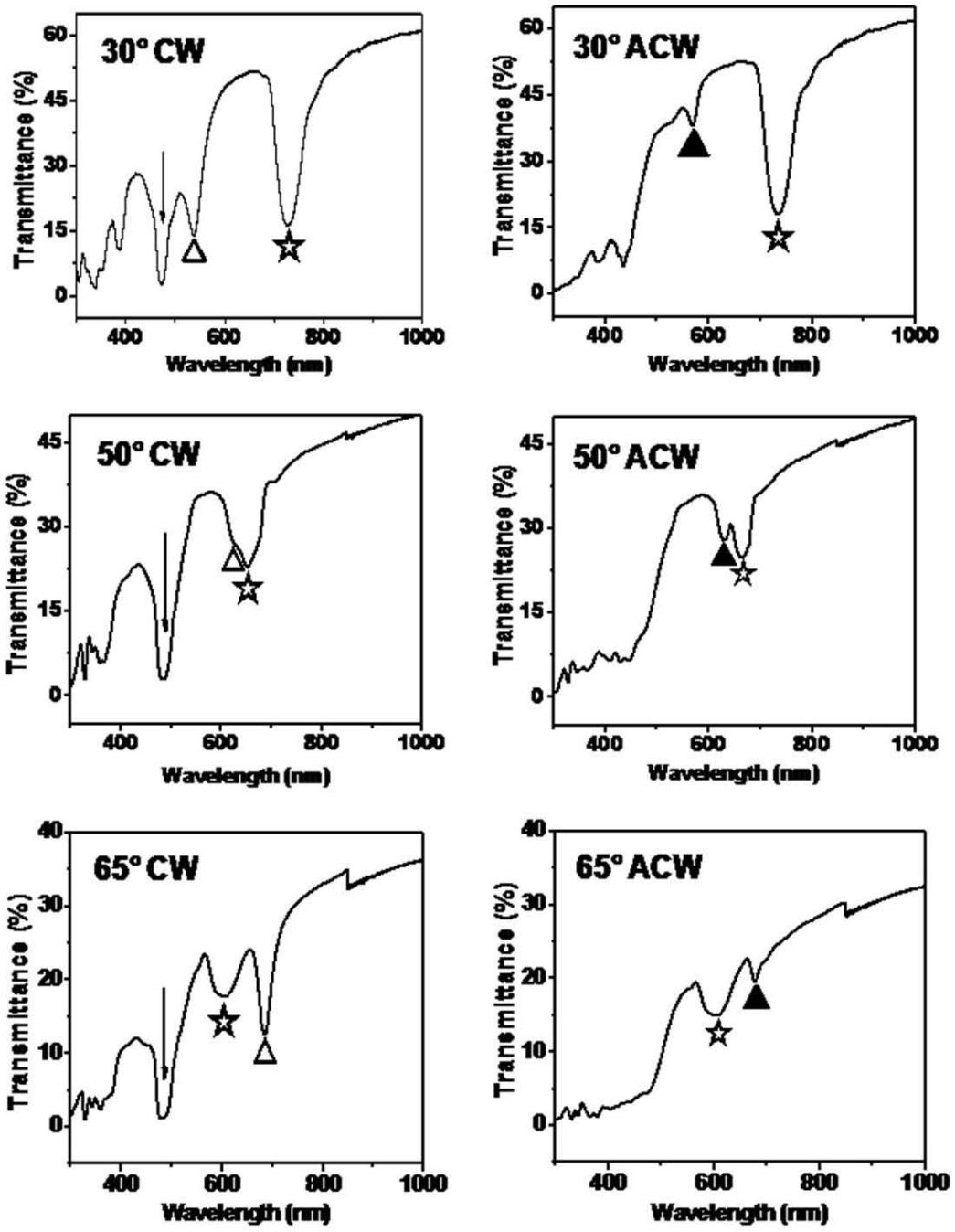

Figure 11: Transmission spectra recorded in CW and ACW directions from θ = 30 - 65°. The arrows and unfilled triangles represent the respective (220) and $(\bar{1}11)$ *planes in CW direction and the filled triangles represent the (200) plane until 50° and then* $(\bar{1}11)$ *plane in ACW direction. Star marked dips correspond to (111) plane in both directions.*

the $(\bar{1}11)$ plane. From these fittings it is found that CW represents the LK path and ACW represents the LU path in the first BZ of the fcc structure. We observed that the average stop band depths for (200) and $(\bar{1}11)$ planes are 4% and 9% upto θ = 50° respectively. After θ = 55° the stop band depth for $(\bar{1}11)$ plane in the LK and LU paths is not same even though the dips represent the same Bragg plane and found that average stop band depths in both the paths are 9% and 4%. In the CW direction another dip appears at θ = 10° and it has shifted to longer wavelength region till θ =

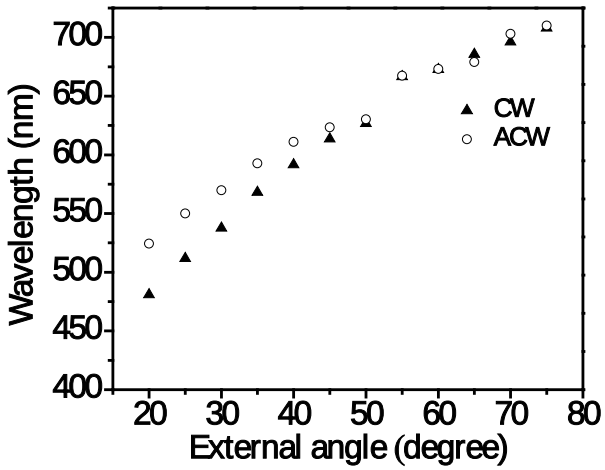

Figure 12: Transmission dips corresponding to $(\bar{1}11)$ *and (200) CW (filled triangles) and ACW (open circles) directions from θ = 20-75°.*

55° and again shifted to shorter wavelength region up to θ = 75°. This is represented with an arrow mark as shown in figure 11. This dip is well fitted to the (220) plane. This also confirms that CW direction is LK path where K point represents the (220) point in FBZ of the fcc structure.[5] The (220) plane has attained 25% of stop band depth at θ = 35° in this LK path which is the normal incidence for (220) Bragg plane. This is the maximum depth for the stop band due to (220) plane that has been reported till now to the best of our knowledge. After this angle the stop band depth monotonically decreases and at θ = 75° it attains a value of 4%. The theoretical fits using equation 8 for different planes are shown in figure 13a by continuous lines. From the fits, the inter-planar spacings and angles β for (200), $(\bar{1}11)$ and (220) planes are 233, 263 and 166 nm and 53°, 66° and 35°, respectively. The β obtained

for ($\bar{1}11$) plane is better than the value obtained in reference 7 which indicates the superior quality of the PC.

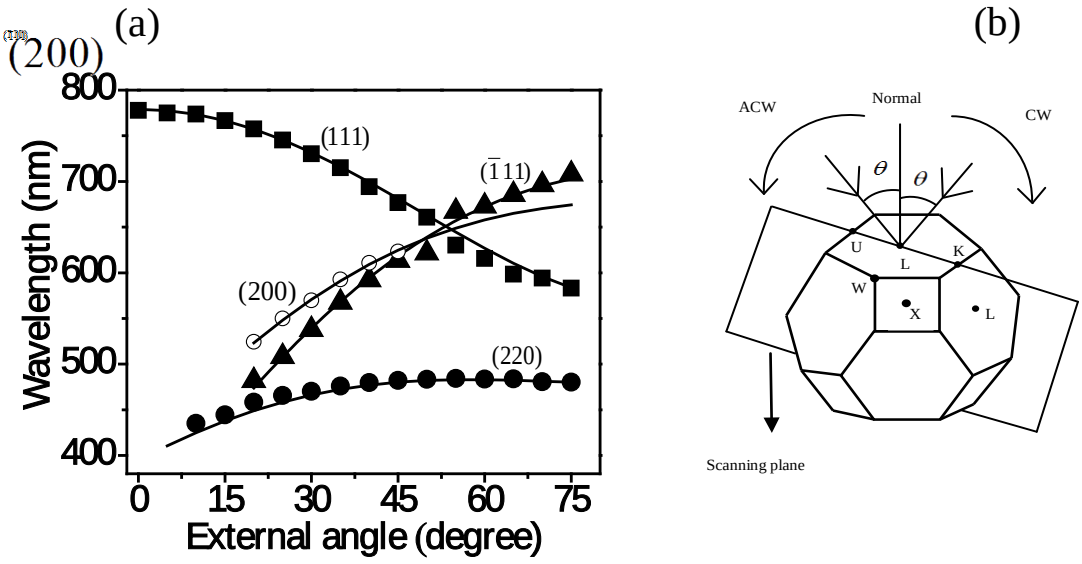

Figure 13: (a) Experimental transmission dips corresponding to (111) (squares), (200) (open circles), ($\bar{1}11$) *(filled triangles) and (220) (filled circles) planes in the CW and ACW directions from θ = 10 - 75° and line represents the theoretical fitting. (b) FBZ of fcc structure which indicates the LK and LU paths in the CW and ACW directions.*

In ACW direction the features of the (220) plane are also present but with less stop band depth compared with the CW direction. At θ = 50° the two dips due to ($\bar{1}11$) and (111) planes merge up in the CW direction, while in the ACW direction there is a clear splitting of dips as shown in figure 11. This behavior is expected due to the phenomenon of simultaneous diffraction by the (111) and (200)/($\bar{1}11$) families of planes.[30,31] But in the CW direction the dips do not split as the ($\bar{1}11$) plane makes more angle than the (200) with the (111) plane. In our study we found the features of (200) plane appear from θ = 20 to 50° in the LU path. After θ = 50° it follows the ($\bar{1}11$) curve fitting. The interplanar spacing which is nearly equal for these two planes (d_{200} = a/2 and $d_{\bar{1}11}$ = a/1.732) probably resulted in the observation of this kind of behavior after θ = 50°. The band structures calculated for (111) plane are same in the LU and LK paths[2] and the data obtained here follow the same. In our

study we observed that the diffraction efficiencies are more for (111) and (220) and less for (200) and $(\bar{1}11)$ planes. For (220) plane the FWHM increases from 24.4 nm ($\theta = 30°$) to 38.7 nm ($\theta = 65°$) and then decreases to 34.3 nm ($\theta = 75°$). For (200) and $(\bar{1}11)$ planes the FWHMs have not followed any particular monotonic increase or decrease. Finally, the observations are viewed such that the PC is oriented in the LK and LU paths of the first BZ when the transmission spectrum is recorded in the CW and ACW directions as shown in figure 13b. The more pronounced stop bands due to different planes in the LK direction from $\theta = 30$ to 50° are as shown in figure 11. This large stop band depth with θ till 45° due to different planes in our PC is reminiscent of the PBGs that present in the hetero structure PC. The clear observation of (200) and $(\bar{1}11)$ planes in the LU and LK paths with large stop band depths and steeper band edges over a wide range of incident angle are reported for the first time. This, we feel, signifies the high quality of PCs prepared by us. Many studies in the literature report the observation of (200) or $(\bar{1}11)$ or mixing of these Bragg planes in the same path.[6,30,32,33] This study clearly brings out the contribution of different Bragg planes in different paths (LU and LK). This again could be due to the good crystalline structure of PC. These stop bands due to different Bragg planes certainly promises many applications in the area of integrated optics, e.g. optical switches and filters.

3.9 Polarization dependent reflection spectral characteristics

The polarization dependent spectral characteristics due to (111) plane are carried out in the reflection geometry using s-, p- and unpolarized light. The beam dimensions at near normal incidence (5°) are 5×3 mm^2. Reflectivity spectra with external incident angle from $\theta = 5$ to 60° for D = 331 nm PS PC are shown in figures 14a-d. The peak height and FWHM are the two important properties that get mainly affected with increasing incident angle when recorded with polarized and un-polarized light. First, in the case of the s-polarized light a nearly constant reflectivity was observed at each

external angle, while a decrease of peak height is observed with both the p- and un-polarized light as shown in figures 14a-c. The changes in the height of the absolute

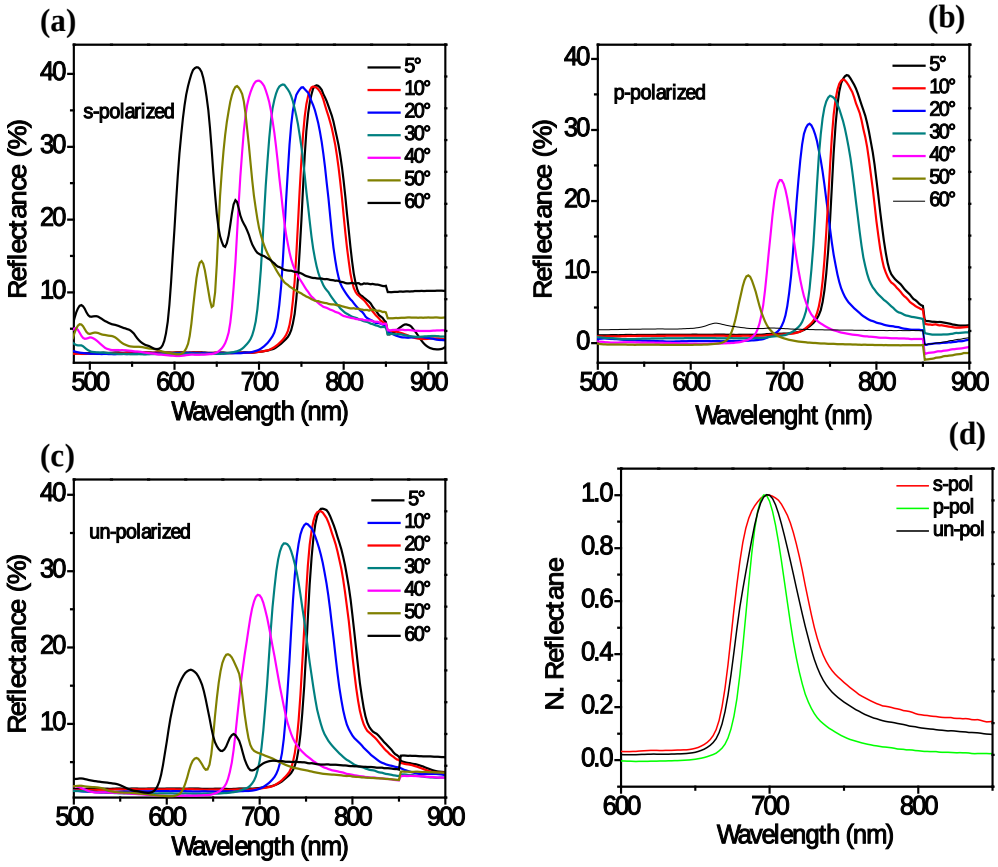

Figure 14: Measured reflectance spectra for a) s- b) p- and c) un-polarized light for D = 331 nm PS PC. d) Normalized reflectance spectra at θ=40° for s-, p- and un-polarized light.

reflectance are 2, 8 and 6% for s-, p- and unpolarized light respectively. This effect can be attributed to Brewster angle effect. Around at θ = 55°, the appearance of two peaks is attributed to the simultaneous diffraction due to (111) and $(\bar{1}11)$/(200) Bragg planes. For s- and un-polarized light the two peak behavior is observed while it is absent in the case of p-polarized light. As the volume fraction for (111) plane is larger compared to other planes in the fcc lattice,[6] only a small percent of the peak corresponding to (111) plane is expected to appear in the case of p-polarized light as presented in figure 14b.

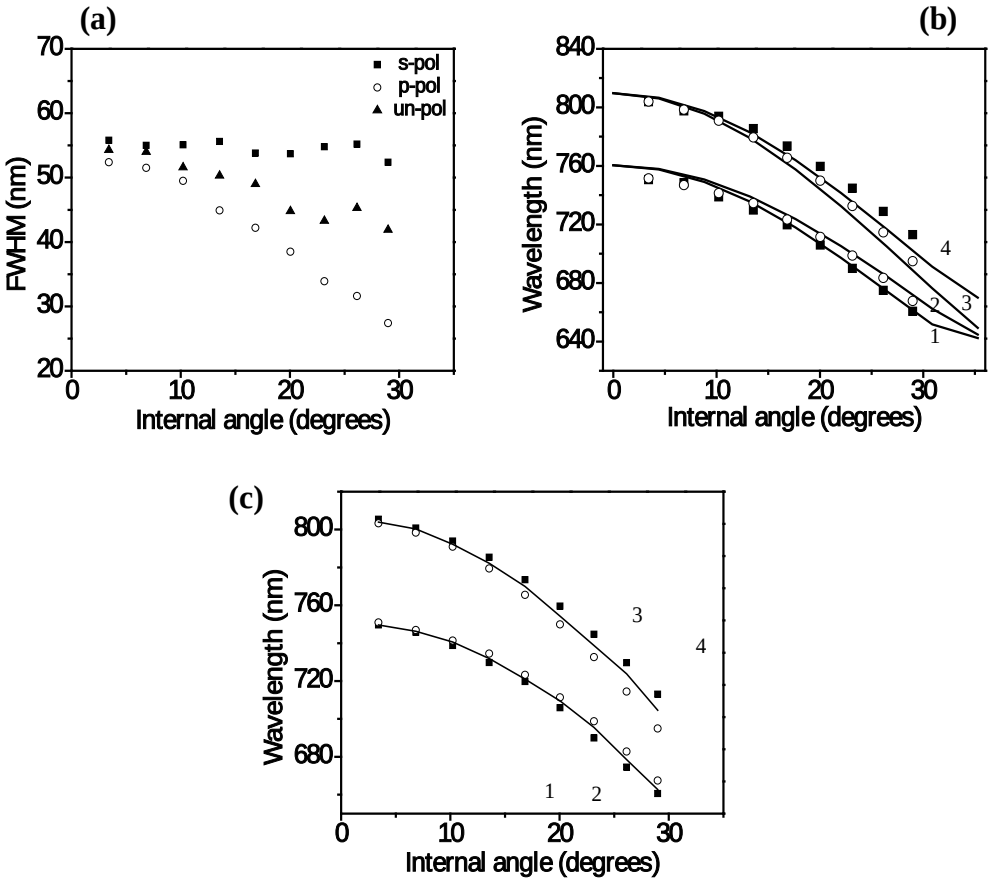

Figure 15: a) Measured FWHM at each internal angle of incidence for s- (square), p- (circle) and unpolarized (triangle) light. b) FWHMs of s- (square) and p- (circle) polarized light compared with band gap calculations (lines) using RSoft (BandSolve). c) Comparison of FWHMs of s-(square, 1&4), p-(circle, 2&3) and un (lines) polarized light. The internal angle for every θ can be found using Snell's law (n_{eff} is used for PC structure which is obtained in the section 3.6).

The normalized reflectance spectra obtained at θ = 40° for s-, p- and unpolarized light are shown in figure 14d which clearly shows the (second) important property of FWHM of reflection spectra is different for different polarizations. The FWHM at normal incidence remains constant irrespective of polarization and shows a reduction with increasing angle as presented in figure 15a. The four lowest lying calculated energy bands represented by lines (1, 2, 3 and 4) as shown in figure 15b are identical irrespective of the tilting the of the PC around the normal to (111) plane for the

angular range of θ = 5 to 45°.[34] Hence, the corresponding data obtained in this angular range is compared with the band gap calculations as shown in figure 15b. The external angles are converted into internal angles using Snell's law (n_{eff} is used for PC structure which is obtained in the section 3.6) in order to compare the experimental FWHMs obtained at each θ with the band gap calculations. Galisteo-Lopez et al.[34] have reported that the electromagnetic modes of s-polarized light couple to bands 1 and 4 while the inner bands 2 and 3 couple to p-polarized light in the band diagram calculations (lines) and the same is observed with our sample as shown in figure15b. Moreover, it is mentioned in the reference 32 that the electromagnetic modes of un-polarized light couple to outer bands only as the modes which couple to 2&3 will be hidden as the broader peaks correspond to s-polarized light contain narrow peaks correspond to p-polarized light. In contrast, we observed that the FWHM due to un-polarized light (represented by line) falls in between the 1&2 and 3&4 band lines as shown in figure 15c and it is more pronounced for the external angle range of θ = 20-45°. Moreover, the decrease in FWHM for p-polarized light is more and it is less in the case of s- and unpolarized light. According to previous discussion in section 3.7, the reduction in the FWHM with higher number of layers indicates that the penetration length for p-polarized light is more compared to s-polarized light. Hence, p-polarized light experiences more number of bulk defects and cracks resulting in smaller narrowing for s-polarized light while larger narrowing for p-polarized light.[35,36] However, the unpolarized light which consists of both the components of s- and p-polarization components penetrates much deeper inside the crystal compared to s-polarized light and result in smaller peak widths than that of s-polarized light.

3.10 Conclusions

In summary, different sizes of PS microspheres were synthesized using emulsifier-free emulsion polymerization and PCs were fabricated using vertical deposition method. The crystal parameters of effective refractive index and inter-planar spacing

were found out using angle dependent transmission spectral characteristics. The stop band features due to (111) plane for two different thicknesses are compared with the scalar wave approximation and the number of layers are calculated. By comparing the Fabry-Perot fringes The features of different planes like (200), (220) and $(\bar{1}11)$ with predominant optical quality in terms of large stop band depth and steeper band edges are discussed from the transmission spectral characteristics. It is confirmed that the features of (200) and $(\bar{1}11)$ planes are more prominent in the LK path while the features of (200) plane for lower angles and $(\bar{1}11)$ plane features for higher angles in the LU path due to the increasing area of the $(\bar{1}11)$ planes contributing to the spectral features with angle variation.

Finally, it is found that the experimentally observed peak widths of reflection spectra obtained for $\theta>20°$ for unpolarized light do not follow the theoretical bands calculated using plane wave expansion method and they fall in between the bands 1&2 and 3&4. This observation indicates that the unpolarized light penetrates more deep inside the crystal structure compared to s-polarized light and it is maximum for p-polarized light.

3.11 References

1. Galisteo-López, J. F. *et al.* Self-Assembled Photonic Structures. *Advanced Materials* **23**, 30–69 (2010).
2. Galisteo-López, J. F., Palacios-Lidón, E., Castillo-Martínez, E. & López, C. Optical study of the pseudogap in thickness and orientation controlled artificial opals. *Phys. Rev. B* **68**, 115109 (2003).
3. Ishii, M., Harada, M., Tsukigase, A. & Nakamura, H. Photonic band structures of colloidal crystals measured with angle-resolved reflection spectroscopy. *Colloids and Surfaces B: Biointerfaces* **56**, 224–230 (2007).
4. Schutzmann, S., Venditti, I., Prosposito, P., Casalboni, M. & Russo, M. V. High-energy angle resolved reflection spectroscopy on three-dimensional photonic crystals of self-organized polymeric nanospheres. *Opt Express* **16**, 897–907 (2008).
5. Romanov, S. G., Bardosova, M., Essig, S., Busch, K. & Peschel, U. Polarisation anisotropy in colloidal photonic crystals. *ICTON Mediterranean Winter Conference,2009. ICTON-MW 2009. 3rd* 1 –5 (2009).doi:10.1109/ICTONMW.2009.5385629
6. Romanov, S. Anisotropy of light propagation in thin opal films. *Physics of the Solid State* **49**, 536–546 (2007).
7. Baryshev, A. V., Khanikaev, A. B., Fujikawa, R., Uchida, H. & Inoue, M. Polarized light coupling to thin silica-air opal films grown by vertical deposition. *Phys. Rev. B* **76**, 014305 (2007).

8. Rybin, M. V. *et al.* Complex interaction of polarized light with three-dimensional opal-based photonic crystals: Diffraction and transmission studies. *Photonics and Nanostructures - Fundamentals and Applications* **4**, 146–154 (2006).
9. Liu, G. Q. *et al.* Synthesis and photonic band gap characterization of high quality photonic crystal heterostructures. *Optik - International Journal for Light and Electron Optics* **122**, 9–13 (2011).
10. Arshady, R. Suspension, emulsion, and dispersion polymerization: A methodological survey. *Colloid & Polymer Science* **270**, 717–732 (1992).
11. Odian, G. *Principles of Polymerization*. (Wiley-Interscience: 2004).
12. Kim, J. H., Chainey, M., El-Aasser, M. S. & Vanderhoff, J. W. Emulsifier-free emulsion copolymerization of styrene and sodium styrene sulfonate. *Journal of Polymer Science Part A: Polymer Chemistry* **30**, 171–183 (2003).
13. Míguez, H. *et al.* Evidence of FCC Crystallization of SiO2 Nanospheres. *Langmuir* **13**, 6009–6011 (1997).
14. Ha, N. Y., Wu, J. W. & Park, B. Fabrication and optical characterization of 3-D polystyrene colloidal photonic crystal. *Journal Of The Korean Physical Society* **45**, 108–111 (2004).
15. Medebach, M. & Palberg, T. Phenomenology of colloidal crystal electrophoresis. *The Journal of Chemical Physics* **119**, 3360–3370 (2003).
16. Ye, Y.-H., LeBlanc, F., Haché, A. & Truong, V.-V. Self-assembling three-dimensional colloidal photonic crystal structure with high crystalline quality. *Applied Physics Letters* **78**, 52–54 (2001).
17. Wang, L. *et al.* Binary Colloidal Crystals Fabricated with a Horizontal Deposition Method. *Langmuir* **25**, 6753–6759 (2009).
18. Dimitrov, A. S. & Nagayama, K. Continuous Convective Assembling of Fine Particles into Two-Dimensional Arrays on Solid Surfaces. *Langmuir* **12**, 1303–1311 (1996).
19. Lin, S. Y. *et al.* A three-dimensional photonic crystal operating at infrared wavelengths. *Nature* **394**, 251–253 (1998).
20. Norris, D. J., Arlinghaus, E. G., Meng, L., Heiny, R. & Scriven, L. E. Opaline Photonic Crystals: How Does Self-Assembly Work? *Advanced Materials* **16**, 1393–1399 (2004).
21. Woodcock, L. V. Entropy difference between the face-centred cubic and hexagonal close-packed crystal structures. *, Published online: 09 January 1997; | doi:10.1038/385141a0* **385**, 141–143 (1997).
22. Zhang, H., Duan, R., Li, F., Tang, Q. & Li, W. Microscopy evidence of the face-centered cubic arrangement of monodisperse polystyrene nanospheres. *Materials & Design* **28**, 1045–1049 (2007).
23. Cheng, B. *et al.* More direct evidence of the fcc arrangement for artificial opal. *Optics Communications* **170**, 41–46 (1999).
24. Gu, Z.-Z., Fujishima, A. & Sato, O. Fabrication of High-Quality Opal Films with Controllable Thickness. *Chem. Mater.* **14**, 760–765 (2002).
25. Born, M. & Wolf, E. *Principles of Optics: Electromagnetic Theory of Propagation, Interference and Diffraction of Light*. (Cambridge University Press: 1997).
26. Reculusa, S. & Ravaine, S. Synthesis of Colloidal Crystals of Controllable Thickness through the Langmuir−Blodgett Technique. *Chem. Mater.* **15**, 598–605 (2003).
27. Aguirre, C. I., Reguera, E. & Stein, A. Tunable Colors in Opals and Inverse Opal Photonic Crystals. *Advanced Functional Materials* **20**, 2565–2578 (2010).
28. Shung, K. W.-K. & Tsai, Y. C. Surface effects and band measurements in photonic crystals. *Phys. Rev. B* **48**, 11265–11269 (1993).
29. Jiang, P., Bertone, J. F., Hwang, K. S. & Colvin, V. L. Single-Crystal Colloidal Multilayers of Controlled Thickness. *Chem. Mater.* **11**, 2132–2140 (1999).
30. Schutzmann, S., Venditti, I., Prosposito, P., Casalboni, M. & Russo, M. V. High-energy angle resolved reflection spectroscopy on three-dimensional photonic crystals of self-organized polymeric nanospheres. *Optics Express* **16**, 897 (2008).
31. Romanov, S. G. *et al.* Diffraction of light from thin-film polymethylmethacrylate opaline photonic crystals. *Phys. Rev. E* **63**, 056603 (2001).

32. Khunsin, W., Kocher, G., Romanov, S. G. & Torres, C. M. S. Quantitative analysis of lattice ordering in thin film opal-based photonic crystals. *Advanced Functional Materials* **18**, 2471–2479 (2008).
33. Nair, R. V. & Vijaya, R. Multiple Bragg diffraction in polymeric photonic crystals. *Applied Optics* **48**, G59 (2009).
34. Galisteo-Lopez, J. F., López-Tejeira, F., Rubio, S., López, C. & Sánchez-Dehesa, J. Experimental evidence of polarization dependence in the optical response of opal-based photonic crystals. *Applied Physics Letters* **82**, 4068–4070 (2003).
35. Thijssen, M. S. *et al.* Inhibited Light Propagation and Broadband Reflection in Photonic Air-Sphere Crystals. *Phys. Rev. Lett.* **83**, 2730–2733 (1999).
36. Galisteo Lòpez, J. F. & Vos, W. L. Angle-resolved reflectivity of single-domain photonic crystals: Effects of disorder. *Phys. Rev. E* **66**, 036616 (2002).
37. van Driel, H. M. & Vos, W. L. Multiple Bragg wave coupling in photonic band-gap crystals. *Phys. Rev. B* **62**, 9872–9875 (2000).

CHAPTER 4

Abstract

We report the Bragg diffraction due to different high Miller-index planes in the transmission spectral characteristics of 331 nm diameter polystyrene photonic crystals with different alcohols as background media. The stop band features due to (311) *Bragg plane are observed over a wide range (33^0) of incident angles with ethanol as background. We also investigated systematically the results on the change of the volume fraction of polystyrene microspheres and the uniform shifting of different high Miller-index Bragg plane features when the photonic crystal is introduced in different alcohols.*

Spectral and morphological changes of 3D polystyrene photonic crystals with the incorporation of alcohols

3.1 Introduction

Detecting specific organic molecules is of great interest for environment protection and human health and many efforts have been made to develop and improve effective and simple means of sensors. Today, there are many novel sensor methods especially that based on optical measurements enabling advanced sensing with faster, environmentally safer and easier to implement than those employing the electrical measurements.[1] Lately, porosity in materials is well investigated for the application of optical sensors. Mainly they show enormous changes in the prominent characteristics such as refractive index, absorption or emission when these porous structures are occupied by the probed substance.[1,2,3,4,5] Similarly, opals which consist of organic polymer microspheres in fcc structure will provide templates for the optical sensors. Although opals are known for the absence of complete photonic band gap, the stop band positions are quite sensitive to the change in refractive index of the 26% interstitial volume. Properties such as long-range ordering, maximal packing density, well-defined pore size, and high surface-to-volume ratio make these self assemblies suitable candidates for physical, chemical and biological sensors[6,7,8] and display products.[9]

In the last few years several researchers are focusing on understanding the colloidal crystal geometry through various experimental and analytical techniques which enable one to know the details of stop bands due to various planes that present in a fcc structure and improve the efficiency of opal structures as sensors. For example, Asher et al. have studied diffraction efficiencies of the putative fcc (111), (200), (220) and (311) planes and the structural characteristics of the colloidal photonic crystals (PCs) using Kossel ring analysis.[10] Khunsin et al.[11] have reported quantitatively, based on the Fourier transform analysis of

scanning electron microscope (SEM) images. They find an improvement in the hexagonal lattice formation and better ordering of Bragg planes with acoustic noise agitation during the crystal growth. Polarization dependent studies were also done to understand the colloidal crystal geometry by Schutzmann et al.[12] Most of the experiments in literature are focused on the study of polarization dependent photonic band structures of colloidal PCs[13,14,15] and it has become a challenging debate for the explanation of Bragg-diffraction due to the high Miller index (hMi) planes of the optical spectra of 3D opals. Hence, the work presented here focuses on the study of stop bands due to different hMi Bragg planes by a simple technique of incorporating ethanol into the interstitials of D = 331 nm PS PC. This also helped us to identify hMi Bragg planes with large stop band depth due to their shifting towards the longer wavelength region. This shift in the stop bands due to hMi Bragg planes is proposed to help improve the sensitivity of the PC sensors. Earlier studies[15] report the effect of alcohols on the stop bands of different Bragg planes using silica PCs. Here we study the hMi Bragg planes of PS PC and the effect of alcohols on them. We interpret our observed results with the changes in volume fractions and the refractive index contrast.

3.2 Experimental Details

The transmission spectral characteristics of D = 331 nm PC are recorded using UV-Vis-NIR spectrophotometer (JASCO: V-670) in the range from 300 nm to 1000 nm in steps of 0.2 nm using beam dimensions of 1 mm x 6 mm at normal incidence. The PC was dipped in a cell (25 mm x 25 mm x 4 mm) containing alcohol solution for recording the transmission spectra. When alcohol solution was completely removed and the PC was dried, the PC exhibited the same spectra as before the immersion in alcohol. Reproducibility of the spectra was observed even after several cycles of immersion and drying. This demonstrates that PC does not lose its generic symmetry of lattice and mechanical stability with the treatment of the alcohols. Since the fcc structure is anisotropic, the periodicities along different directions are different. The transmission spectrum was therefore measured by changing the angle of incidence from 0-75° and 0-63° for PC with

air (bare) and alcohols as background media respectively. The lower limit to the angles is due to equipment limitation of accommodating the glass cell.

3.3 Results and Discussion

Two equations are used to find Bragg resonances for (111) and other (hkl) planes as follows.[16,17]

$$\lambda_{111} = 2d_{111}\sqrt{n_{eff}^2 - sin^2\theta} \quad (1)$$

$$\lambda_{hkl} = 2d_{hkl}n_{eff}\sqrt{1 - sin^2\left\{\beta - \arcsin\left(\frac{sin\theta}{n_{eff}}\right)\right\}} \quad (2)$$

Here, d_{111} and d_{hkl} are the inter-planar spacing for (111) and (hkl) planes. For (111) planes d_{111}=0.816D, where D is the diameter of the PS microspheres. n_{eff} is the effective refractive index defined as

$$n_{eff}^2 = f_{PS}n_{PS}^2 + f_b n_b^2 \quad (3)$$

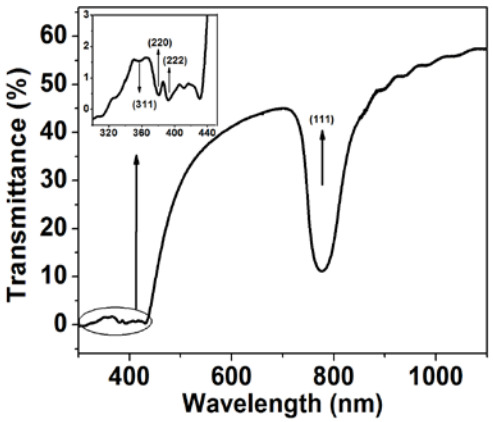

Table 1

plane	Expt value (nm)	Calculated value (nm)
(220)	393	395
(222)	380	389
(311)	358	358

Figure 1: Transmission spectra of bare PC at normal incidence. Inset shows the dips corresponding to (311), (220) and (222) Bragg planes respectively. Table 1 indicates the central wavelengths of stop bands due to different hMi Bragg planes at normal incidence in bare PC.

f_{PS} and f_b are the volume fractions of PS microspheres and background media of PC for the close packed fcc structure of identical microspheres and the refractive indices of PS and background are n_{ps} (=1.59) and n_b respectively and θ is the

external angle between the incident wave and normal to the (111) plane. β is the angle between the normal of (111) and any other (hkl) planes. The central wavelength and stop band depth for (111) plane at normal incidence are 776 nm and 35% respectively as shown in figure 1. The hMi Bragg planes like (220), (222) and (311) planes are shown in the inset of figure 1 and their corresponding experimental and calculated values of the central wavelengths are given in table 1.

From the Fabry-Perot fringes[18] as shown in figure 1 the thickness of the sample can be estimated as 6.6 μm. From the thickness the number of layers can be found as 26. These fringes indicate the homogeneity of the thickness and effective refractive index of the PC within the illuminated area. The inter-planar spacing, thereby diameter and effective refractive index can be calculated from the angle dependent transmission spectra for the set of (111) planes as λ_{111}^2 varies linearly with $\sin^2\theta$ from equation 1. The linear fit parameters, slope (=$-4d_{111}^2$) and intercept (=$4d_{111}^2 n_{eff}^2$) of λ^2 vs $sin^2\theta$ plot, are d_{111}= 270 nm and

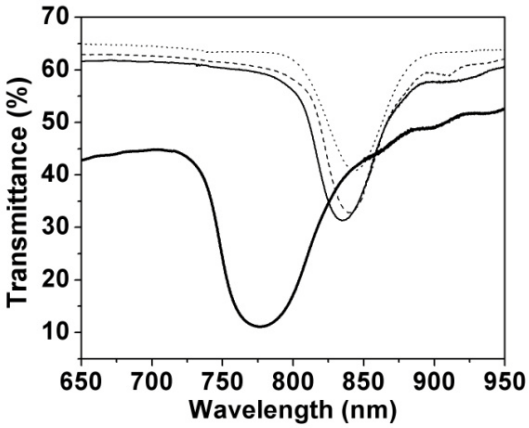

Figure 2: Transmission spectra recorded at normal incidence for bare PC (thick line) and when it is infiltrated with methanol (thin line), ethanol (dashed line), butanol (dotted line) as backgrounds.

n_{eff}=1.459 respectively. These values are used for fitting the stop bands due to other planes obtained in the transmission spectra for bare PCs. The diameter D can be calculated as d_{111}=0.816D for the close packed fcc structure and it is found to be 331 nm which is in good agreement with the FESEM values. Now

the PC was kept vertically in a cell which contains 5 ml of alcohol solution and the transmission spectra were recorded at normal incidence.

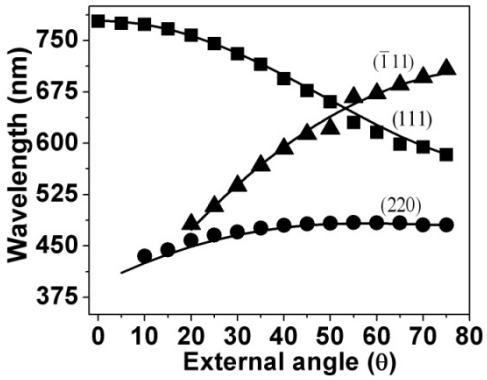

Figure 3: Theoretical fitting for the experimentally observed diffraction features of different planes obtained in bare opal; filled squares, triangles and circles represent the corresponding (111), (1̄11) and planes (220) respectively.

The shifting of (111) Bragg dips from bare PC (thick line) to PCs with methanol (thin line), ethanol (dotted line) and butanol (dashed line) as the background media are shown in figure 2. We observe huge shift of PBG towards longer wavelength region compared to bare PC due to increment of background

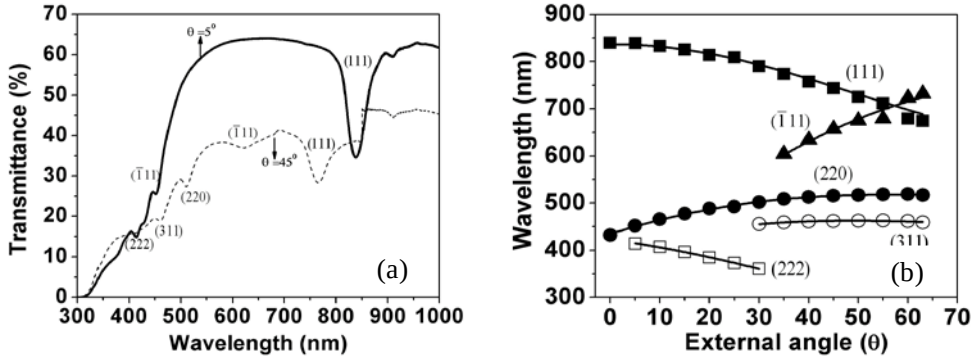

Figure 4: (a) Transmission spectra of PC in ethanol as background at θ = 5° (thin line) and 40° (dashed line). (b) Theoretical fitting for the hMi Bragg planes obtained with ethanol as background; filled squares, triangles, circles, open circles and squares represent the (111), (1̄11), (220), (311) and (222) planes respectively.

refractive index. This shift to longer wavelengths finds application in the field of chemical and physical sensors as reported elsewhere.[6,8] From figure 2, it is

observed that the stop band depth for butanol is approximately 20% and a maximum of 30% for methanol.

The full width half maximum (FWHM) $\Delta\lambda$ of the stop band mainly depends on the volume fraction of PS/background and the refractive index contrast δn_c. The $\Delta\lambda$ and the volume fractions of PS (f_{PS}) microspheres in different alcohols as background media are calculated using the following equation 4[19] and they are given in the table 2.

$$\Delta\lambda = \lambda_c \left| \frac{4(sint - tcost)\delta n_c^2}{\pi^2\alpha^3(f_{PS}\delta n_c^2+1)+\sqrt{\pi^4\alpha^6(f_{PS}\delta n_c^2+1)^2-4\delta n_c^4(sint-tcost)^2}} \right| \quad (4)$$

Here λ_c is the central wavelength of the stop band, $t = (3/2)\alpha^3\pi^2 f_{PS}$, $\delta n_c = \frac{n_{ps}}{n_b}$ and $\alpha = \sqrt{3}$ for Γ-L direction. The increase of f_{PS} with the increment of

Table 2: Estimated values of f_{ps} and FWHM using equation 4 in different alcohols as background media.

Background	Refractive index n_b	Calculated f_{PS}	Calculated FWHM (nm)	Expt. FWHM (nm)	Expt. λ_c for (111) plane (nm)
air	1	0.742	67.45	67.13	776
methanol	1.33	0.786	44.96	44.96	835.9
ethanol	1.36	0.794	41.97	41.91	840
butanol	1.39	0.808	39.71	39.74	848.1

refractive index of the background is an indirect evidence of swelling of microspheres in the alcohol media and it is maximum for butanol.

Similar studies were carried out for the swelling of microspheres in water[20,21] which were confirmed through atomic force microscope studies. As 0.74 can be the largest value for f_{PS}, the observed values for f_{PS} >0.74 in alcohols indicate

the non-uniform swelling of the microspheres (into the air gaps), which is being reported here for the first time. The experimental $\Delta\lambda$ for different background media were found to decrease with increasing refractive index of background as shown in the table 2.

As the shift for the PBG with ethanol as the background medium is much larger than for the methanol, we chose ethanol to study the hMi Bragg planes by recording the angle dependent transmission spectra. From the linear plot of λ_{111}^2vs $sin^2\theta$ with ethanol as background, the values of $d_{111}$and n_{eff} are obtained as 279 nm and 1.548 respectively. It may be noted that these values are for the swollen microspheres in ethanol. By substituting f_{ps} for ethanol in equation 3 we get a value for n_{eff} as 1.545, which is in good agreement with the value obtained from the linear plot with ethanol as background. This value is used for fitting the stop bands due to other planes with ethanol as background. The transmission spectrum is recorded in the LK path of the Brillouin zone (BZ) of close packed fcc structure.

At the shorter wavelength region the transmittance decreases drastically at normal incidence as shown in figure 1 due to the Bragg diffraction by other planes. These planes get well resolved and shift towards longer wavelength region with increasing θ for both bare and alcohol doped PCs. However stop band due to (222) plane shifts towards shorter wavelength region due to its characteristic nature. The (220) plane features appear from θ=10-75° and ($\bar{1}$11) plane features appear from θ=20-75°. The fittings (lines) for ($\bar{1}$11) (triangles) and (220) (circles) plane for bare PC are shown in figure 3.

At θ = 54° the two dips due to ($\bar{1}$11) and (111) planes coincide and after this angle they shift towards their corresponding directions. The appearance of these two dips/peaks in transmission/reflection spectra at 54° is attributed as the phenomenon of wave coupling that occurs when the incident wave vector reaches

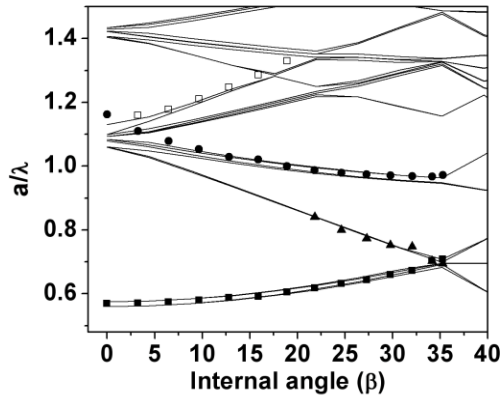

Figure 5: Comparison of various stop band features obtained with ethanol as background with the band diagrams generated in the LK path of BZ of close packed fcc structure using Bandsolve software. Filled squares, triangles, circles, and open squares indicate (111), ($\bar{1}$11), (220) and (222) respectively.

the U/K point, and diffracted by the (111) and (200)/($\bar{1}$11) families of planes simultaneously.[22] From the fitting of equation 2 for wavelength vs. angle of incidence, the inter-planar spacing and angle β for ($\bar{1}$11) and (220) planes are calculated as 263 and 166 nm and 66° and 35° respectively for the bare PC.

For the PC with ethanol as background we observe additional features belonging to (311) and (222) planes along with the ($\bar{1}$11) and (220) Bragg planes as shown in figure 4(a). The ($\bar{1}$11) (filled triangles), (220) (filled circles), (311) (open circles) and (222) (open squares) plane features appear for θ values of 0° to 63°, 0° to 63°, 30° to 63° and 5° to 30° respectively as shown in figure 4b. The solid lines correspond to the fittings using equation 2. From these fits one can obtain the inter-planar spacing for ($\bar{1}$11), (220), (311) planes as 274, 167, 149 nm respectively and the corresponding angles β for these planes are 66.5° and 32.6°, 28.9°. The inter-planar spacing for (222) plane is 142 nm. This is approximately half of the d_{111}. In bare PC the features of (311) and (222) planes can be observed well only at normal incidence. Features due to these two sets of planes appear better with ethanol as the background and also over wide range of incident angles. Earlier report[11] shows the features due to (311) plane appears at only one incident angle. We attribute our observation of these planes over wide angles due to larger δn_c for PS PC compared to silica PC and also to the incorporation of

alcohol. We strongly believe that this is the first report on the observation of (311) and (222) planes over a wide range (33°) of incident angles for PS PCs. Larger the diameter more will be the shift of the stop bands due to different planes towards the longer wavelength region.[8] The study of hMi Bragg planes by incorporating alcohols inside the interstitials of PC leads to an indirect method to realize the features due to different planes which otherwise cannot be seen with bare PC. The values of λ_c for different Bragg planes are compared with the band diagrams calculated in the LK path of BZ of fcc structure using RSoft's BandSOLVE commercial sfotware[23] which implements plane wave

Table 3: The central wavelengths of the stop bands due to different hMi Bragg planes at θ = 45° and 5° in different alcohols as background media.

Background	(111) θ = 45° (nm)	$(\bar{1}11)$ θ = 45° (nm)	(220) θ = 45° (nm)	(311) θ = 5° (nm)	(222) θ = 5° (nm)
air	671.4	623.9	476.3	--	--
methanol	736.1	651.8	511.5	460.4	417.2
ethanol	742.2	655.8	514.5	461.6	421.4
butanol	749.7	659.7	518.2	463.9	422.4

expansion method. Figure 5 shows the comparison of observed and calculated values for the stop bands due to (111), $(\bar{1}11)$, (220) and (222) planes. The X and Y- axes represent the internal angle in PC with ethanol as background and the frequency in the reduced units of 'a/λ' respectively. Here 'a' is the lattice constant of the crystal. It is found that there is a good agreement between experimental data and the calculated band diagrams. As the (311) plane zone does not contain the high symmetry points of irreducible BZ of fcc, the stop band features due to (311) Bragg plane cannot be compared with the band gap calculations which are calculated based on plane wave expansion method.[24] However in our present study, we could achieve a very good fit for the stop band due to (311) plane using equation 2.

The stop bands show a maximum depth at normal incidence to a particular hMi planes. figure 6a and 6b show the stop bands due to (222), (311), (220) and ($\bar{1}$11) planes in different alcohols as background. Transmission shows

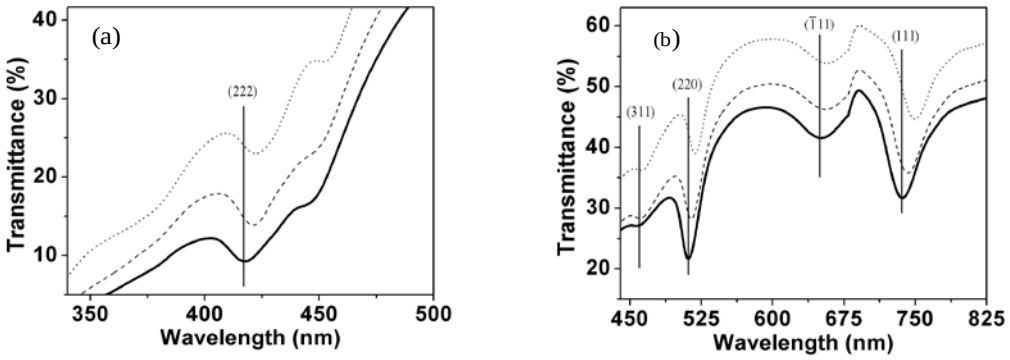

Figure 6: Transmission spectra of PC (a) at θ = 5° (b) θ = 45° when it is infiltrated with the methanol (thin), ethanol (dashed), and butanol (dotted) background media. The vertical lines represent the variation of λ_c for the (222), (311), (220), ($\bar{1}$11) and (111) planes.

a dip at θ =5° for (222) plane and at θ = 45° for (311), (220)and ($\bar{1}$11) planes as these angles are close to the normal's of their corresponding planes. The vertical lines in figure 6a and 6b show the shifting of corresponding planes in methanol (thin) ethanol (dotted) and butanol (dashed) as background media. From table 3 it can be inferred that the shifts uniformly increase as one goes from methanol to butanol. These uniform shifts also indicate that the alcohols penetrate the PC uniformly.

The shifting of the stop bands due to ($\bar{1}$11) and (220) planes is very close to that of the shifting of stop band due to (111) plane. In comparison to the shifting of stop bands due to ($\bar{1}$11) and (220) planes, (311) and (222) planes show smaller stop band shifts with the addition of alcohols. The uniform shifting of the stop bands due to hMi planes in alcohols as background, therefore, enhances the measurement accuracy for different alcohols that show a variation in the second decimal of the refractive index.

3.4 Conclusions

In conclusion, different hMi Bragg plane characteristics were investigated with the incorporation of highly volatile solvents into the interstitials of PCs and the observed stop bands were compared with the calculated band diagrams. The volume fraction of PS microspheres was found to increase by 6.6% in butanol in comparison to bare PC. We showed that observation of the hMi Bragg planes in addition to (111) plane can essentially improve the sensitivity of the PC application as a refractive index sensor.

3.5 References

1. Hsiao, V. K. S. *et al.* Organic Solvent Vapor Detection Using Holographic Photopolymer Reflection Gratings. *Advanced Materials* **17**, 2211–2214 (2005).
2. Gao, J., Gao, T., Li, Y. Y. & Sailor, M. J. Vapor Sensors Based on Optical Interferometry from Oxidized Microporous Silicon Films. *Langmuir* **18**, 2229–2233 (2002).
3. Li, Y. Y. *et al.* Polymer Replicas of Photonic Porous Silicon for Sensing and Drug Delivery Applications. *Science* **299**, 2045–2047 (2003).
4. Convertino, A., Capobianchi, A., Valentini, A. & Cirillo, E. n. m. A New Approach to Organic Solvent Detection: High-Reflectivity Bragg Reflectors Based on a Gold Nanoparticle/Teflon-like Composite Material. *Advanced Materials* **15**, 1103–1105 (2003).
5. Li, J. & Zheng, T. A comparison of chemical sensors based on the different ordered inverse opal films. *Sensors and Actuators B: Chemical* **131**, 190–195 (2008).
6. Ozin, G. A. & Arsenault, A. C. P-Ink and Elast-Ink from lab to market. *Materials Today* **11**, 44–51 (2008).
7. Chiappini, A. *et al.* Opal-Type Photonic Crystals: Fabrication and Application. *Advances in Science and Technology* **71**, 50–57 (2010).
8. Nishijima, Y. *et al.* Inverse silica opal photonic crystals for optical sensing applications. *Opt Express* **15**, 12979–12988 (2007).
9. Ge, J., Goebl, J., He, L., Lu, Z. & Yin, Y. Rewritable Photonic Paper with Hygroscopic Salt Solution as Ink. *Advanced Materials* **21**, 4259–4264 (2009).
10. Asher, S. A., Weissman, J. M., Tikhonov, A., Coalson, R. D. & Kesavamoorthy, R. Diffraction in crystalline colloidal-array photonic crystals. *Phys. Rev. E* **69**, 066619 (2004).
11. Khunsin, W., Kocher, G., Romanov, S. G. & Torres, C. M. S. Quantitative analysis of lattice ordering in thin film opal-based photonic crystals. *Advanced Functional Materials* **18**, 2471–2479 (2008).
12. Schutzmann, S., Venditti, I., Prosposito, P., Casalboni, M. & Russo, M. V. High-energy angle resolved reflection spectroscopy on three-dimensional photonic crystals of self-organized polymeric nanospheres. *Opt Express* **16**, 897–907 (2008).
13. Ishii, M., Harada, M., Tsukigase, A. & Nakamura, H. Photonic band structures of colloidal crystals measured with angle-resolved reflection spectroscopy. *Colloids and Surfaces B: Biointerfaces* **56**, 224–230 (2007).
14. Romanov, S. G. *et al.* Erasing diffraction orders: Opal versus Langmuir-Blodgett colloidal crystals. *Applied Physics Letters* **90**, (2007).

15. Rybin, M. V., Samusev, K. B. & Limonov, M. F. High Miller-index photonic bands in synthetic opals. *Photonics and Nanostructures - Fundamentals and Applications* **5**, 119–124 (2007).
16. Aguirre, C. I., Reguera, E. & Stein, A. Tunable Colors in Opals and Inverse Opal Photonic Crystals. *Advanced Functional Materials* **20**, 2565–2578 (2010).
17. Romanov, S. Anisotropy of light propagation in thin opal films. *Physics of the Solid State* **49**, 536–546 (2007).
18. Born, M. & Wolf, E. *Principles of Optics: Electromagnetic Theory of Propagation, Interference and Diffraction of Light*. (Cambridge University Press: 1997).
19. Tarhan, I. I. & Watson, G. H. Analytical expression for the optimized stop bands of fee photonic crystals in the scalar-wave approximation. *Physical Review B - Condensed Matter and Materials Physics* **54**, 7593–7597 (1996).
20. Galembeck, A., Costa, C. A. R., Medeiros da Silva, M. do C. V. & Galembeck, F. Macrocrystal Swelling: AFM in Situ Observation of Particle and Film Deformation and Motion. *Journal of Colloid and Interface Science* **234**, 393–399 (2001).
21. Chen, X., Chen, Z., Lu, G., Bu, W. & Yang, B. Measuring the swelling behavior of polymer microspheres with different cross-linking densities and the medium-dependent color changes of the resulting latex crystal films. *Journal of Colloid and Interface Science* **264**, 266–270 (2003).
22. Galisteo-López, J. F., Palacios-Lidón, E., Castillo-Martínez, E. & López, C. Optical study of the pseudogap in thickness and orientation controlled artificial opals. *Phys. Rev. B* **68**, 115109 (2003).
23. RSoft Design Group, BandSOLVE. at <http://www.rsoftdesign.com/products.php?sub=Component+Design&itm=BandSOLVE>
24. Onodera, Y. Band structure and Jones zone of SnTe. *Solid State Communications* **11**, 1397–1399 (1972).

CHAPTER 5

Abstract

The enhancement of nonlinear absorption of polystyrene was investigated using 3D polystyrene photonic crystals with Z-scan technique. The Z-scan experiment was carried out at 532 nm in the picosecond regime. The transmittance of the photonic crystal was found to get modified because of the non linear absorption of polystyrene particularly when 532 nm is near the band edges of photonic band gap. Calculations show that the field gets enhanced by 1.4 times the input field intensity within the crystal when the 532 nm wavelength falls at the band edge while keeping the crystal at an angle of 35°.

Experimental verification of enhanced electromagnetic fields at the band edge of 3D polystyrene photonic crystals using Z-scan technique

5.1 Introduction

In 1993, Dowling et al. have observed the enhanced gain in photonic band edge lasers [PBEL].[1] In semiconductor physics, for an electron at the band edges, the de Broglie wave is nearly standing and effective mass of the electron becomes very large.[2] In a similar analogy, at the band edges of PC, the group velocity of light approaches zero. As a result, the photon undergoes many multiple reflections in the crystal structure and leads to the increased path length which would enhance the effective gain and thus results in low threshold lasers. In the same year, Scalora et al. investigated the ultrashort pulse propagation through 1D PCs and proposed the band edge optical limiting and switching mechanisms[3] based on intensity dependent transmission or reflections of PC. These pioneer works motivated many scientists to fabricate the low threshold lasers and ultrafast optical switches with 3D opal structures.[4,5,6] A good amount of literature is available on the study of enhanced nonlinear optical properties with 1D PCs.[7,8,9,10] In particular, Hache´ and Bourgeois et al. have observed enhanced two photon absorption (TPA) and Kerr nonlinearity using silicon based 1D PCs.[11] In the case of colloidal PCs the depth/height (transmission/reflection spectra) of photonic stop band (PSB) due to (1 1 1) plane is maximum as it occupies larger filling fraction compared to other planes.[12] However, the overlapping of PSBs due to the high Miller index planes such as (2 0 0), (2 2 0), (2 2 2), etc. lead to larger attenuation in the transmitted light than that due to the (1 1 1) plane. Here, in this work we look at the EM field enhancement at the edges of the PSB due to (1 1 1) plane.

5.2 Nonlinear absorption

Nonlinear absorption refers to the change of transmittance of a material as a function of intensity or fluence. The high intensities associated with nanosecond, picosecond or femtosecond pulses can induce profound changes in the optical properties of a material leading to a nonlinear response of the real and imaginary parts of polarization. The imaginary part of the nonlinear polarization is associated for instance with two/multiphoton transitions and will exhibit a n-photon resonance when two level of an atomic or molecular system can be connected by n optical quanta via an intermediate virtual state, as schematically shown in figure 1.

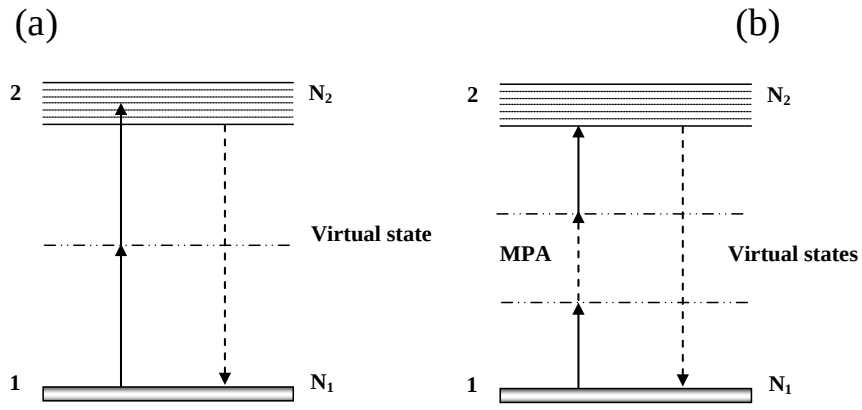

Figure 1: Schematic energy level diagram for (a) Two-photon absorption (TPA); (b) Multi-photon absorption.

In this case, the attenuation of the incident light is described by

$$\frac{dI(z)}{dz} = -\alpha_n I^n(z)$$

where α^n is the n-photon absorption coefficient.

$$\frac{dI(z)}{dz} = -\alpha_n I^n(z)$$

$$\int_{I_{in}}^{I_{out}} \frac{1}{I^n(z)} dI(z) = -\alpha_n \int_0^L dz$$

$$-\alpha_n L = \left[\frac{I^{-n+1}}{-n+1} \right]_{I_{in}}^{I_{out}} \Rightarrow \alpha_n L = \frac{1}{n-1} \left[\frac{1}{I_{in}^{n-1}} - \frac{1}{I_{out}^{n-1}} \right]$$

$$\alpha_n L = \frac{1}{(n-1) I_{in}^{n-1}} \left[1 - \frac{1}{T^{n-1}} \right], \text{where } T = \frac{I_{out}}{I_{in}} \quad T^{n-1} = \frac{1}{1 + \alpha_n L (n-1) I_{in}^{n-1}}$$

$$T = \frac{1}{\left[1 + \alpha_n L (n-1) I_{in}^{n-1} \right]^{\frac{1}{n-1}}}$$

$$\frac{I_{in}}{\omega_0^2} = \frac{I_{00}}{\omega_Z^2}, \quad \text{where } I_{in} = \frac{I_{00}}{1 + \frac{Z^2}{Z_0^2}} \text{ and } \omega_Z^2 = \omega_0^2 \left(1 + \frac{Z^2}{Z_0^2} \right)$$

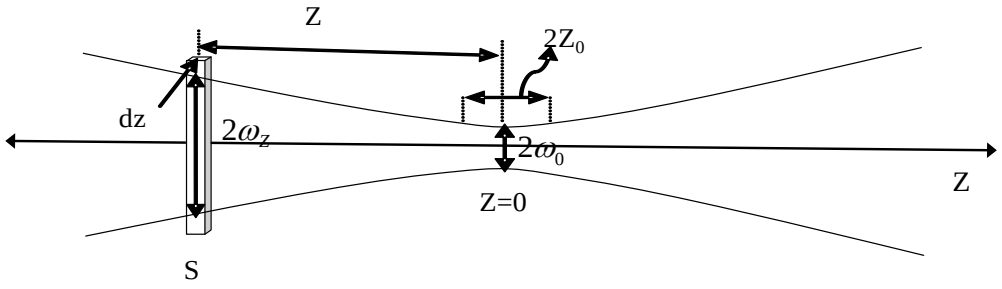

Figure 2: Schematic diagram of focused laser beam.

$$T = \frac{1}{\left[1+(n-1)\alpha_n L\left(I_{00}/\left(1+\left(Z/Z_0\right)^2\right)\right)^{n-1}\right]^{1/n-1}}$$

$$\Rightarrow T_{OA(nPA)} = \frac{1}{\left[1+(n-1)\alpha_n L\left(I_{00}/\left(1+\left(Z/Z_0\right)^2\right)\right)^{n-1}\right]^{1/n-1}}$$

where α_n is the effective multi photon absorption coefficient (n = 2 for two photon absorption; n = 3 for three photon absorption, and so on), I_{00} is the peak intensity (at Z=0), I_{in} is intensity at sample position (if Z- is the distance from focal point I_{in} (I_Z) is the intensity at that point), $Z_0 = \pi\omega_0^2/\lambda$ is the Rayleigh range, ω_0 is the beam waist at the focal point (Z=0), dz is small slice of the sample, I_{in} is input intensity and I_{out} is output intensity of the sample. The Z-scan technique was introduced by Sheik-Bahae et al.[13] for accurate and sensitive measurements of nonlinear absorption ($\alpha_2 = \beta$) and refraction by translating a sample along the optical axis of a focused Gaussian beam. The main consequence of two photon absorption or multiphoton absorption in nonlinear optics is optical limiting. In literature people have reported the OL studies with semiconductor, metal, organic nanoparticles and graphene composites.[14,15,16] A wide variety and well known nonlinear optical phenomenon like multi photon absorption, excited state absorption, self-focusing or defocusing and nonlinear scattering are exploited for achieving OL.[16,17] OL is a nonlinear optical process in which the transmittance of a material decreases with increased incident light intensity. Optical limiters are one of the most important types of devices used to control the amplitude of high intensity optical pulses. These devices work due to intrinsic properties of the materials used for their fabrication. An ideal optical limiter has a linear transmittance at low input intensities, but above the threshold intensity (I_{th}) (at which non linear absorption takes place) its transmittance becomes constant. The ideal behavior of such a device is shown in figure 3.

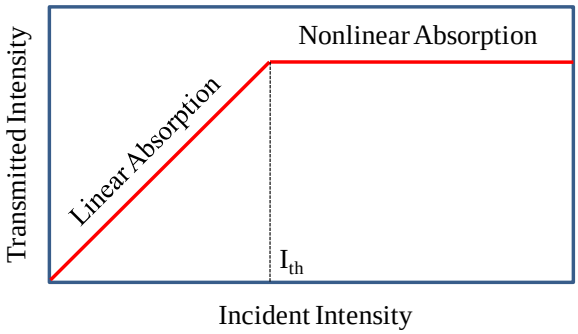

Figure 3: An ideal optical limiter.

5.3 Motivation of the Experiment

We show in this section the effect of photonic band gap on the emission spectrum of Rhodamine B (RhB) by doping the PC with a dye. RhB is chosen as its characteristic emission spectrum overlaps with the stop bands of D = 260 nm PS PC from θ = 0 - 45° and the dye is easily soluble in water. D = 260 nm PS microspheres are put in 10^{-5} M of RhB[18] water solution and the crystal growth is carried out at the same temperature and humidity of the bare opals. The RhB doped PC is found to have the same thickness as that of bare PC. This low concentration of RhB has not altered the the position of the stop band and the crystal structure. The stop band due to (111) plane of RhB doped PC at near normal incidence given in the inset of figure

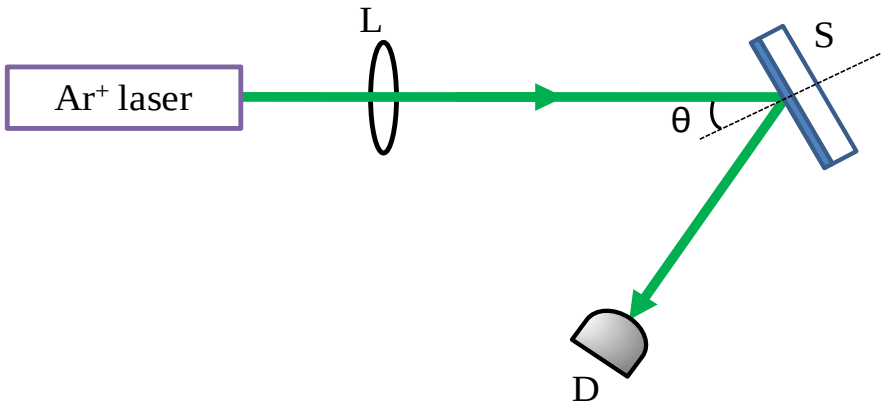

Figure 4: Schematic of emission collection for PC. S: PC substrate, L: Lens, D: detector, θ: incident angle and dotted line indicates the normal to PC.

5. The dye in the PC is excited with the 514.5 nm wavelength from the continuous wave Ar^+ laser and it is transmitted through the PC as it falls outside region of the stop band of D = 260 nm PS PC. A low excitation power of the beam 4 mW was used in order to avoid the bleaching of the laser dye in the crystal. The spectral characteristics are recorded with a fiber connected to the Ocean Optics spectrometer in the reflection geometry as shown in figure 4. The laser beam is focused to 30 μm by using a lens of 200 mm focal length. The PC is mounted on a rotational stage that has resolution of 1°. The emission is collected at a distance of 5 cm from the sample surface and the same distance is maintained for every angle of collection. One can see that the stop band due to (111) plane at normal incidence for the D = 260 nm PS PC (inset of figure 5) falls on the larger wavelength side of the emission of the dye.

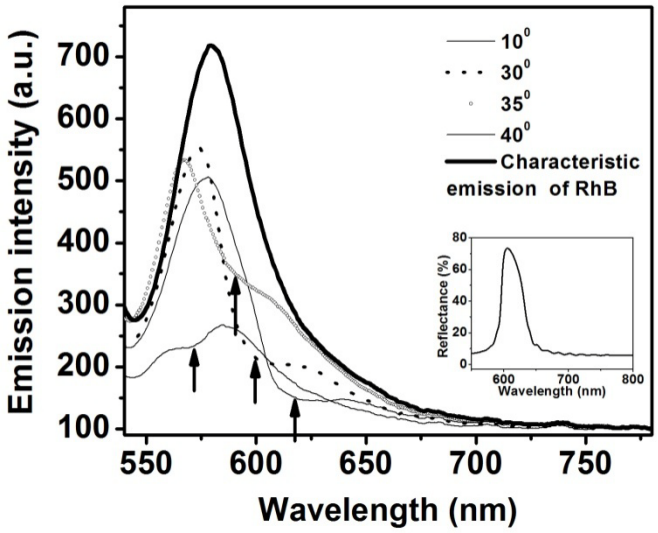

Figure 5: Emission changes of RhB doped in D = 260 nm PS PC by changing the angle of incident from θ = 10-40°. The suppression due to stop band of (111) plane is indicated by an arrow for each angle. Thicker line represents the characteristic emission of RhB doped in D = 331nm diameter PS PC. Inset shows the reflection spectra of RhB doped D = 260 nm PS PC at θ = 5°.

Thick continuous line in figure 5 is the characteristic emission of the same dye which is doped in D = 331 nm PS PC (for which the stop band is far from the emission of RhB). The peak wavelength of emission is at 579 nm with FWHM of 34 nm. The

emission spectrum is collected for different orientations/angles with respect to the excitation wavelength at 514.5 nm of Ar^+ laser. The detector position is kept slightly away from the specular reflection of the PC in order to avoid the saturation of spectrometer with the excitation wavelength. Though the characteristic emission spectrum of the dye should remain the same for any excitation ray angle, the emission from the dye doped in D = 260 nm PS PC recorded at different angles as shown in figure 5, clearly indicates the effect of the photonic band gap. The emission gets suppressed on the shorter wavelength side with the increase of the incident angle θ. This clearly shows that the emission is not from the surface of the PC but comes from the inner layers of the PC. This inhibition of emission wavelengths due to photonic band gap would be very useful in achieving the increased gain at different wavelengths. Our results also indicate the good crystalline structure of the PC and the uniform distribution of the dye throughout the crystal structure. This change in emission observed could lead to the realization of low threshold lasers in which control of spontaneous emission is a key factor. This inhibition of spontaneous emission at different positions of emission of RhB for different incident angles leads to an experiment of Z-scan to investigate the control of nonlinear absorption of PS using PC structures.

5.4 Experimental details for Z-Scan

A frequency doubled Nd:YAG laser with 30 ps and 10Hz repetition rate was used for nonlinear optical studies. Optical limiting and Z-scan studies were performed with different incident angles from 0-50° by focusing the input beam onto the sample using a lens of focal length 120 mm and collecting the output effectively with a large-area fast photodiode (FND100). The PCs (used in this work) fabricated from D = 225 and 331 nm PS microspheres, show stop bands in ‘green’ and near ‘infrared’ wavelength regions, so they will be termed as GRPC and IRPC respectively throughout this work. From the Fabry-Perot fringes we estimated the thickness of the GRPC and IRPC are around 3.3 μm.

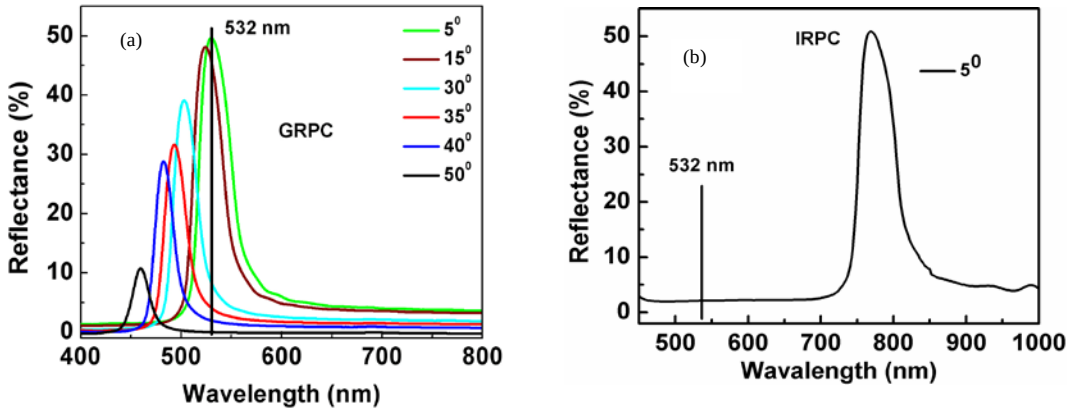

Figure 6: (a) and (b) show reflectance spectra recorded with JASCO spectrometer with p-polarization light of beam dimensions 1 mm × 6 mm for GRPC at θ = 5, 15, 30, 35, 40 and 50° and for IRPC at θ = 5° respectively. The vertical line shows the position of 532 nm.

5.5 Results and Discussion

The angle dependent reflection spectra for GRPC with incident angles θ = 0-50° (LU direction) recorded with large beam (1 mm × 6 mm of JASCO spectrometer) dimensions indicate weak Fabry-Perot (FP) fringes at the band edges as shown in figure 6a. As the transmission/reflection spectral characteristics of 3D opal structures are polarization dependent and the laser source used in this experiment delivers p-polarized 532 nm light, we show the corresponding p-polarization dependent spectral characteristics of PSB due to (111) plane as shown in figure 6a. For GRPC the central wavelength of the PSB due to (111) plane changes from 528 to 466 nm for θ = 0 to 50°. The height and full width at half maxima (FWHM) of PSB vary with increasing θ and they reduce from 50% (θ = 5°) to 11% (θ = 50°) and from 35 nm (θ = 5°) to 18 nm (θ = 50°) respectively. Around θ = 35°, 532 nm falls at the edges of the PSB, which is indicated by a vertical line as shown in figure 6a. Figure 6b shows the reflection spectra of IRPC recorded at normal incidence for which 532 nm falls very far from the PSB.

The Z-scan beam waist for 532 nm was calculated to be around 28 μm. The peak intensity, I_{00} at the focus is ~ 13 GW/cm^2. The observed valley behavior from the open aperture (OA) Z-scan curve represents TPA of the PS in which the material absorbs maximum energy at higher intensities and with lowest transmission. From figure 7a it is observed that for GRPC the normalized transmittance (NT) has decreased from 0.94 to 0.46 for θ = 0° to 35°. After θ = 35° NT has increased to 0.6

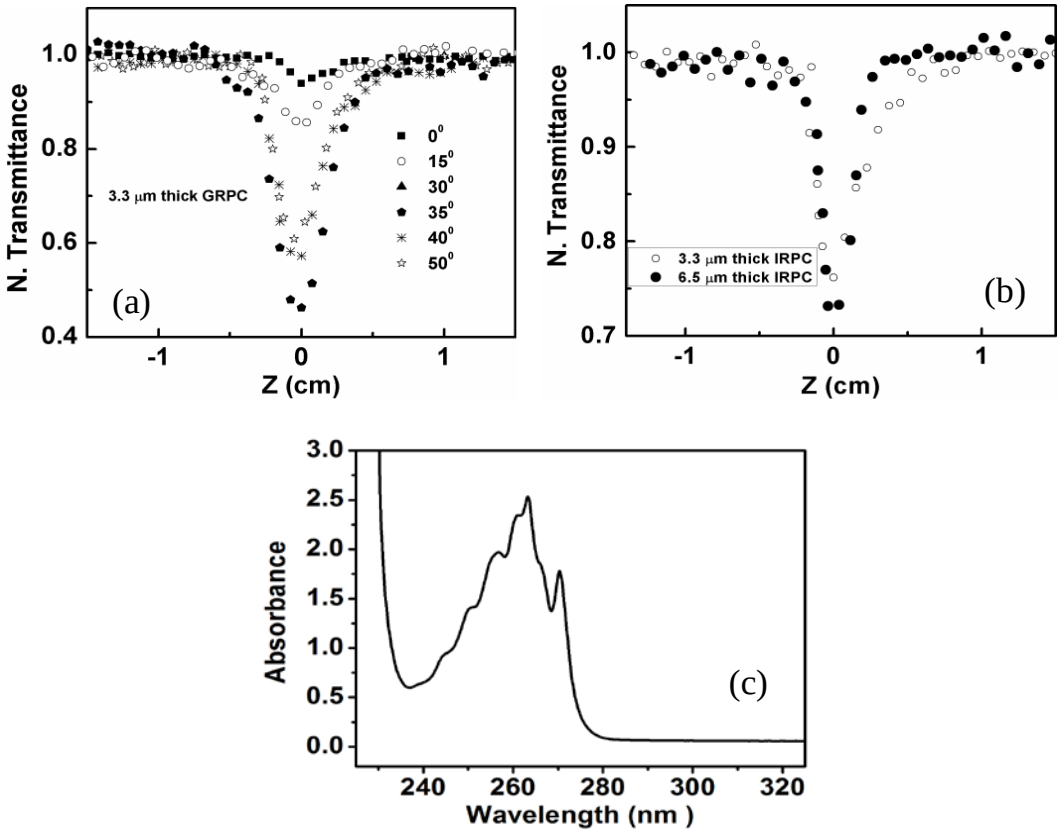

Figure 7: a) Open aperture Z-scan curves of GRPC recorded from θ = 0-50°. b) Open aperture Z-scan curves of IRPCs with thicknesses of 3.3 μm and 6.5 μm recorded at θ = 0°. c) Linear absorption spectra of PS thin film.

at θ = 50°. For GRPC the effective thickness is around 5 μm at the incident angle θ = 50°. In order to confirm that the transmission variation is not due to the thickness variation during the rotations, we compared this transmission with a IRPC whose PSB is far from the 532 nm and also of two different thicknesses, 3.3 μm (IRPC1) and 6.7 μm (IRPC2). The NT falls to 0.76 and 0.73 for IRPC1 and IRPC2

respectively as shown in figure 7b. This indicates that there is no significant variation in the NT for IRPC even for larger thicknesses at higher angles and we can neglect the effect due to thickness variation caused by angular studies in the Z-scan experiment. The 532 nm, which falls at the center of the PSB of GRPC at normal incidence, shifts along the right edge of the PSB with increment of θ. This allows the transmission of the pump intensity increase monotonically with increase of θ to build up enhanced fields in each layer. The observed behavior resembles controlling the nonlinear absorption of PS using PC.

As the absorption peak of PS is around at 260 nm as shown in figure 7c , the nonlinear absorption behavior obtained with PS can be attributed as the phenomenon of TPA process and we have considered a simple two level model (as shown in figure 8) for theoretical fitting. The rate equations for the 2-level model are as follow.

$$\frac{dN_0}{dt} = -\frac{\beta I^2}{2\hbar\omega} + \frac{N_1}{\tau_1}$$

$$\frac{dN_1}{dt} = \frac{\beta I^2}{2\hbar\omega} - \frac{N_1}{\tau_1}$$

$$\frac{dI}{dz} = -\beta I^2$$

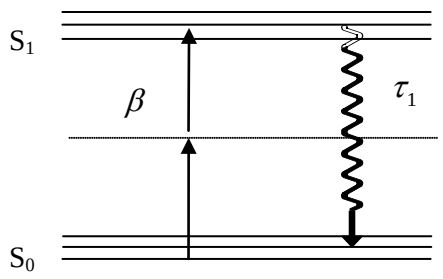

Figure 8: Schematic energy level model of PS. Dotted line represent the virtual state.

with $I = I_{00}(\frac{\omega_0^2}{\omega^2(z)})\exp(-\frac{t^2}{t_p^2})\exp(-\frac{2r^2}{\omega^2(z)})$

and $\omega(z) = \omega_0(1+(z/z_0)^2)^{1/2}$; $z_0 = \frac{\pi\omega_0^2}{\lambda}$

where N_0 and N_1 are the corresponding populations of ground and excited states; τ_1 is the life time of the excited state; I is the intensity as a function of r, t and Z; I_{00} is the peak intensity at the focus; τ_p is the pulse width of the beam used; ω(Z)

and ω_0 are the beam waist at different values of Z and focus respectively and β is the TPA coefficient. The differential equations are solved numerically using the Runge-Kutta fourth-order method. The differential equations are first de-coupled and

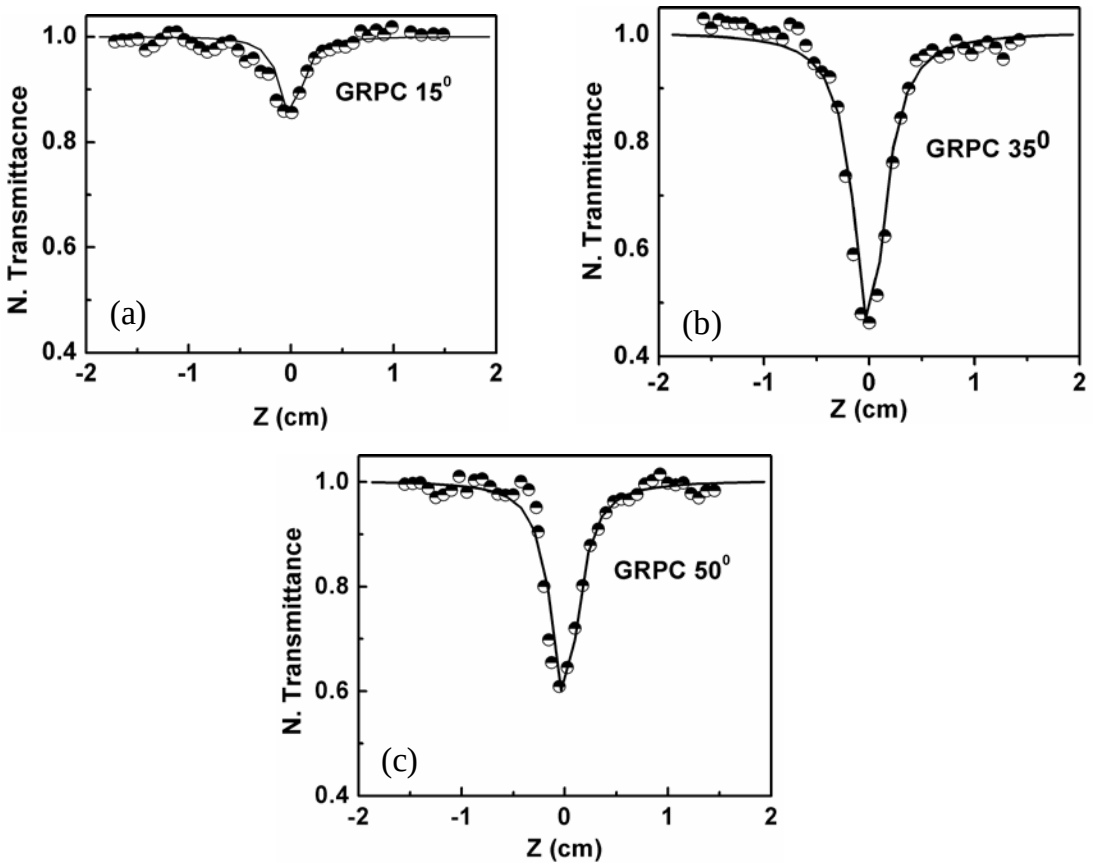

Figure 9: (a) (b) and (c) show the variation in the transmittance and theoretical fits for the GRPC at θ = 15, 35 and 50° respectively.

then integrated over time, length, and along the radial direction. Assuming the input beam to be a Gaussian, the limits of integration for r, t and Z are varied from 0 to ∞, $-\infty$ to ∞ and 0 to L (thickness of the PC) respectively. A typical number of slices used for r, t and Z are 60, 30 and 5 respectively. β is then estimated from the least-squares fit of the experimental data.

Out of the several curves recorded at different angles, we show in figure 9 the experimental and theoretical fits of OA Z-scan data which were obtained at θ=15,

35 and 50° for GRPC using the rate equations. From the fits we obtained β and I_{00} while the value of τ_1 was taken from the literature[19] in order to reduce the number of variables and the fits are reliable. First we made a theoretical fit for the IRPC shown in figure 7b at θ=0° which yielded a value of β as 12.3 cm/GW. With these values of τ_1 and β as the input parameters we arrived at the theoretical fits for GRPC Z-scan data and arrived at the values of I_{00}. From figure 9 and table 1 it can be observed that the value of I_{00} reaches a maximum for GRPC at θ = 35° and falls again for higher angles. All other parameters were kept the same for the curve fitting. At 35°, 532 nm excitation falls right at the band edge, for small angles it falls within the band gap and for angles higher than 35° it falls away from the band gap.

Table 1

	I_{00} (GW/cm^2)	βI_{00} (/cm)
IRPC	13	159.9
GRPC 15°	9	110.7
GRPC 35°	18	221.4
GCPC 40°	16	196.8
GCPC 50°	15	184.5

Here the product βI_{00} indicates the change in nonlinear absorption coefficient due to TPA. From table 1 it is observed that the value of βI_{00} for GRPC at θ = 35° is enhanced nearly 1.4 times compared to IRPC. Thus the field gets enhanced by 1.4 times within the PC and this enhancement is attributed to band edge effect. At the edges of PSB, the group velocity of light reduces which results in large interaction time of EM radiation with the PC.[3,20,21,22] This leads to an increased effective path length and field enhancement due to many multiple reflections. It has been observed

that the reduction of group velocity at the band edges of PS opals by Galisteo-López et al.[20] which support the observation of enhanced fields in the PC structure. The measured group delays reported in the case of silica opals are around 100-150 fs (femtoseconds) and approximately the same reduction in the group velocity can be expected for our experimental conditions.[21,23] At normal incidence (θ = 0°), the diffraction in the PC lattice rejects large portion of 532 nm laser beam from entering the PC interior which results as very weak TPA as shown in figure 9a (represented by filled squares). The linear transmittance values for 532 nm at θ = 30, 35, 40 and 50° are 25, 35, 35 and 35%, respectively. But the observed NT due to TPA falls down. This indicates that the field enhancement is due to the band edge effect and not due to the variation in the linear transmittance. The NT falls more steeply for lower angles (θ < 35°) and less rapidly for higher angles (θ > 35°) and it reaches a minimum value of 0.46 at θ = 35°. This is because at lower values of θ, the 532 nm falls more rapidly into the PSB while for higher values of θ, 532 nm still remains in

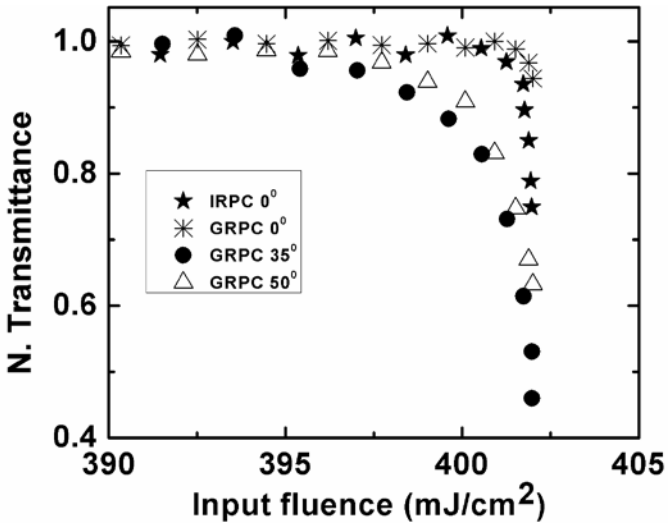

Figure 10: Optical limiting curves for IRPC at θ = 0° and for GRPC at θ = 0, 40 and 50°.

the edge of PSB. As θ increases the PSB moves towards shorter wavelength region and 532 nm moves along the right edge of the PSB due to (111) plane. Our observations can be assumed to be free from any band crossing which is expected for θ > 50°.

In order to confirm that the observed changes in the Z-scan transmittance curves are indeed due to the field enhancement, we have taken a 5 μm thick PS film coated on a glass plate using spin coating technique and adjusted the input I_{00} as 11 GW/cm^2 to get a NT of 0.7 at the beam waist. We subsequently measured the NT vs input intensity by increasing the input power. We observed that the NT falls to 0.4 (exactly as that observed with GRPC at 35°) when the I_{00} reaches 15 GW/cm^2 which is exactly 1.4 times of the original value of I_{00}.

In order to show that the PC can be conveniently demonstrated as an optical limiter with different threshold intensities, the data was obtained for IRPC at $\theta = 0^0$ and GRPC for different angles are shown in figure 10. The limiting threshold values for IRPC at $\theta = 0°$ is 401 mJ/cm^2 and for GRPC at $\theta = 0$, 35 and 50° are 401, 395 and 398 mJ/cm^2 respectively. At the PSB edge of GRPC (θ =35°) the limiting threshold is reduced by 6 mJ/cm^2 compared to IRPC ($\theta = 0°$). The major contribution for this behavior is attributed to the enhanced electric field and TPA at the PSB edge of the PC. Though the observed changes are small at present, we expect large enhancements with improvements in the PC preparation and introduction of organic molecules or quantum dots in the interstitials that can enhance nonlinear absorption and refractive index contrast.

5.6 Conclusions

In conclusion we have shown that the nonlinear absorption of PS can be controlled easily through PBG. We observed from the OA Z-scan data, the peak intesnsity in the PC and hence the nonlinear absorption βI_{00} is enhanced by 1.4 times. Due to the enhanced electric field and two photon absorption coefficient, the limiting threshold values are decreased from 401- 395 mJ/cm^2.

5.7 References

1. Dowling, J. P., Scalora, M., Bloemer, M. J. & Bowden, C. M. The photonic band edge laser: A new approach to gain enhancement. *Journal of Applied Physics* **75**, 1896–1899 (1994).
2. Quinn, C. M. *An introduction to the quantum chemistry of solids*. (Clarendon Press: 1973).
3. Scalora, M., Dowling, J. P., Bowden, C. M. & Bloemer, M. J. Optical Limiting and Switching of Ultrashort Pulses in Nonlinear Photonic Band Gap Materials. *Phys. Rev. Lett.* **73**, 1368–1371 (1994).
4. Jin, F., Song, Y., Dong, X.-Z., Chen, W.-Q. & Duan, X.-M. Amplified spontaneous emission from dye-doped polymer film sandwiched by two opal photonic crystals. *Applied Physics Letters* **91**, 031109–031109–3 (2007).
5. Hu, X., Zhang, Q., Liu, Y., Cheng, B. & Zhang, D. Ultrafast three-dimensional tunable photonic crystal. *Applied Physics Letters* **83**, 2518–2520 (2003).
6. Liu, Y. *et al.* 10 fs ultrafast all-optical switching in polystyrene nonlinear photonic crystals. *Applied Physics Letters* **95**, 131116–131116–3 (2009).
7. Hwang, J. & Wu, J. W. Determination of optical Kerr nonlinearity of a photonic bandgap structure by Z-scan measurement. *Optics Letters* **30**, 875–877 (2005).
8. Pong, R. G. S., Wiggins, M., Flom, S. R. & Shirk, J. S. Nonlinear 1D photonic polymer optical limiter materials. *Lasers and Electro-Optics, 2004. (CLEO). Conference on* **2**, 2 pp. vol.2 (2004).
9. Delaye, P., Astic, M., Frey, R. & Roosen, G. Transfer-matrix modeling of four-wave mixing at the band edge of a one-dimensional photonic crystal. *Journal of the Optical Society of America B* **22**, 2494–2504 (2005).
10. Zhu, X. *et al.* Nonlinear optical performance of periodic structures made from composites of polymers and Co3O4 nanoparticles. *Applied Physics Letters* **97**, 093503–093503–3 (2010).
11. Haché, A. & Bourgeois, M. Ultrafast all-optical switching in a silicon-based photonic crystal. *Applied Physics Letters* **77**, 4089–4091 (2000).
12. Romanov, S. Anisotropy of light propagation in thin opal films. *Physics of the Solid State* **49**, 536–546 (2007).
13. Sheik-Bahae, M., Said, A. A., Wei, T.-H., Hagan, D. J. & Van Stryland, E. W. Sensitive measurement of optical nonlinearities using a single beam. *Quantum Electronics, IEEE Journal of* **26**, 760 –769 (1990).
14. Porel, S., Venkatram, N., Narayana Rao, D. & Radhakrishnan, T. P. In Situ Synthesis of Metal Nanoparticles in Polymer Matrix and Their Optical Limiting Applications. *Journal of Nanoscience and Nanotechnology* **7**, 1887–1892 (2007).
15. Krishna, M. B. M., Kumar, V. P., Venkatramaiah, N., Venkatesan, R. & Rao, D. N. Nonlinear optical properties of covalently linked graphene-metal porphyrin composite materials. *Applied Physics Letters* **98**, 081106 (2011).
16. Tutt, L. W. & Boggess, T. F. A review of optical limiting mechanisms and devices using organics, fullerenes, semiconductors and other materials. *Progress in Quantum Electronics* **17**, 299–338 (1993).
17. Sutherland, R. L. *Handbook of Nonlinear Optics*. (CRC Press: 2003).
18. Li, M., Xia, A., Wang, J., Song, Y. & Jiang, L. Coherent control of spontaneous emission by photonic crystals. *Chemical Physics Letters* **444**, 287–291 (2007).
19. Scurlock, R. D., Kristiansen, M., Ogilby, P. R., Taylor, V. L. & Clough, R. L. Singlet oxygen reactions in a glassy polystyrene matrix. *Polymer Degradation and Stability* **60**, 145–159 (1998).

20. Galisteo-López, J. F. *et al.* Effective refractive index and group velocity determination of three-dimensional photonic crystals by means of white light interferometry. *Phys. Rev. B* **73**, 125103 (2006).
21. von Freymann, G., John, S., Wong, S., Kitaev, V. & Ozin, G. A. Measurement of group velocity dispersion for finite size three-dimensional photonic crystals in the near-infrared spectral region. *Applied Physics Letters* **86**, 053108–053108–3 (2005).
22. Delaye, P., Astic, M., Frey, R. & Roosen, G. Transfer-matrix modeling of four-wave mixing at the band edge of a one-dimensional photonic crystal. *Journal of the Optical Society of America B* **22**, 2494–2504 (2005).
23. Vlasov, Y. A., Petit, S., Klein, G., Hönerlage, B. & Hirlimann, C. Femtosecond measurements of the time of flight of photons in a three-dimensional photonic crystal. *Phys. Rev. E* **60**, 1030–1035 (1999).

CHAPTER 6

Abstract

Surface enhanced Raman scattering experiments are carried out both in silver nanoparticles doped polystyrene opal structures and polyvinyl alcohol + silver nitrate thin films. The Raman scattering signal of polyvinyl alcohol, which acts as a stabilizing agent for the silver nanoparticles was found to get enhanced with the formation of the silver nanoparticles. In-situ studies were carried out to record the Raman scattering as well as the Mie scattering to monitor the growth of the silver nanoparticles. Mie scattering was observed in a solution of polyvinyl alcohol + silver nitrate mixture in particular which was not observed in the case of thin films. The diffraction pattern which was seen in the solution was elucidated in the context of bubble formation due to the silver nanoparticles.

In-situ investigation of the formation of silver nanoparticles in polyvinyl alcohol through Raman spectroscopy

6.1 Background of Raman scattering

When a monochromatic light of a certain frequency ν_0 interacts with a molecule, there occurs both elastic and inelastic scattering. Elastically scattered light has the same frequency ν_0 as the incident light and is called Rayleigh scattering while the inelastically scattered light has frequency $\nu_0 \mp \nu_s$ is called Raman scattering, where (ν_s) is related to the characteristic vibrational frequency of the molecule shifted to higher and lower frequencies from incident light. If the frequency is shifted to lower frequencies, $\nu_0 - \nu_s$, it's called Stokes shift. Otherwise, if the frequency is shifted to higher frequencies, $\nu_0 + \nu_s$, it's called anti-Stokes shift.

A simple, classical electromagnetic field description of Raman spectroscopy can be used to explain many of the important features of Raman band intensities. The induced dipole moment, μ with an incident electric field, $E = E_0 \cos(2\pi\nu_0 t)$ (E_0 is the amplitude and t is the time) can be given by

$$\mu = \alpha E = \alpha E_0 \cos(2\pi\nu_0 t) \quad (1)$$

where α is the polarizability and its tensor components depend on the conformation of the molecule. If the molecule is vibrating with a frequency ν_s, the nuclear displacement dq about its equilibrium position is written as

$$dq = q_0 \cos(2\pi\nu_s t) \quad (2)$$

where q_0 is the vibrational intensity. However, the polarizability changes with small displacement from equilibrium position (i.e. molecular vibration), and can be expressed as a function of q using Taylor series,

$$\alpha = \alpha_0 + \left(\frac{\partial \alpha}{\partial q}\right)_0 dq \quad (3)$$

Here, α_0 is the polarizability of the molecular mode at equilibrium position and $\frac{\partial \alpha}{\partial q}$ is the rate of change of α with respect to the change in q, evaluated at the equilibrium position.

By substitution of α in equation 1, the induced dipole can be calculated in the following way

$$\mu = \alpha_0 E_0 \cos(2\pi\nu_0 t) + \left(\left(\frac{\partial \alpha}{\partial q}\right)_0 \frac{q_{0E_0}}{2}\right)\{\cos[2\pi(\nu_0 - \nu_s)t] + \cos[2\pi(\nu_0 + \nu_s)t]\} \quad (4)$$

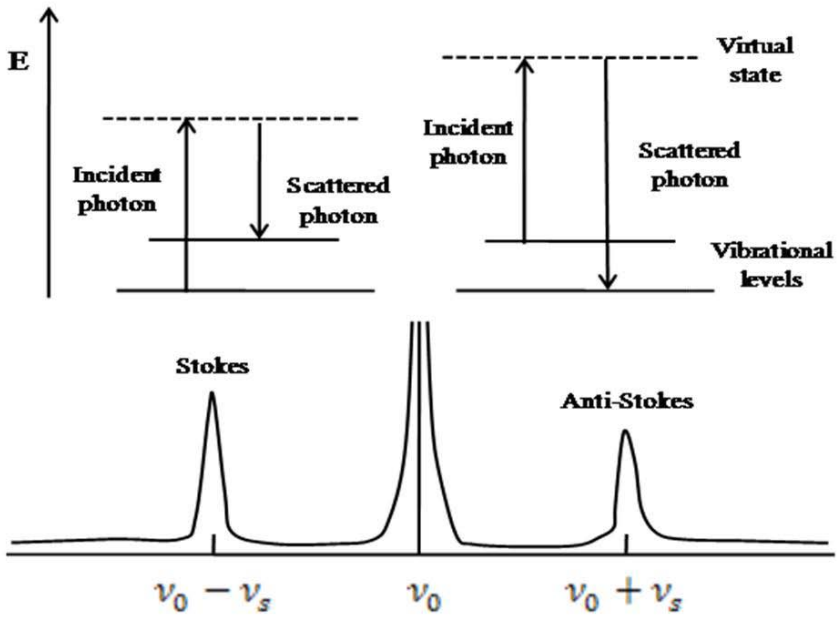

Figure 1: Idealized model of Rayleigh, Stokes and anti-Stokes scattering.

Here the first term describes the Rayleigh scattering of frequency ν_0 and second term gives the Raman scattering of frequencies $(\nu_0 - \nu_s)$ and $(\nu_0 + \nu_s)$ which may be detected as shifts from the Rayleigh frequency although they are very weak. This equation depicts that either molecules should possess larger polarizability or they should experience stronger electric fields in order to achieve higher intense Raman

signal. If $\frac{\partial \alpha}{\partial q} = 0$, the second term of equation 4 vanishes and indicates that the vibration is not Raman active because the molecular polarizability doesnot change during the vibration.

A general question is that if the vibrational modes are Raman-active or IR-active, which concerns the so-called selection rules. In infrared absorption, the vibrations can be detected if the dipole moment, μ of a molecule is changes during the normal vibration, while in Raman spectroscopy, the molecules are Raman active if the polarizability α is changes during the vibration. The intensities of an infrared absorption band, I_{IR}, and Raman active band, I_{Raman} , are proportional to the square of derivative of the polarizability, α, and dipole moment, μ, during the vibration, respectively as given below.

$$I_{IR} \sim (\frac{\partial \mu}{\partial q})^2 \quad (5)$$

$$I_{Raman} \sim (\frac{\partial \alpha}{\partial q})^2 \quad (6)$$

From the group theory, it is straightforward to show that if a molecule has a center of symmetry, vibrations that are Raman active will be "weak" in the infrared, and vice versa.[1] As a consequence of the selection rules, infrared spectroscopy provides a detailed information about the functional groups and Raman spectroscopy, especially, contributes to the characterization of the carbon backbone of organic substances or polymers. Moreover, Raman scattering has become a well-known technique that provides information on vibrational energies of molecules which are the finger prints for unique chemical identification. Despite its small interactive cross-section (10^{-30} to 10^{-25} cm^2/molecule), the Raman scattered signal is very sensitive to the changes in the crystal structure due to impurities, doping, phase transformations etc.[1,2,3] These extremely small cross sections of Raman scattered

signal can be enhanced enormously through the unique property of localized surface plasmons which lead to the field of surface enhanced Raman spectroscopy (SERS).

6.2 Surface enhanced Raman spectroscopy

Metal nanoparticles (NPs) show very complex and interesting optical properties. When a metal NP interacts with the electric field of the incident light, there is a collective oscillation of free electrons in the opposite direction of the electric field, which are termed as plasmons. As a consequence, most metals possess a negative dielectric constant at optical frequencies which causes a very high reflectivity.[4] For metallic NPs with high conductivity which are much smaller than the wavelength of the electromagnetic radiation, if the radiation's wavelength is optimal, the electrons oscillate coherently producing a localized surface plasmon.[4] These localized surface plasmons are characterized by frequencies which depend upon the size, shape and dielectric constant of the object to which the surface plasmon is confined[4]. When a scatterer is placed near to the metal NP, the Raman scattering signal is greatly enhanced and it is known as the so called 'surface enhanced Raman spectroscopy (SERS)'. The first SERS phenomena was discovered by Martin Fleischman and his colleagues[5] in 1974 from pyridine adsorbed on electrochemically roughened silver materials. However, they concluded that the greatly enhanced signals were from the increased surface area. Basically, there are two models that explain SERS mechanism: "electromagnetic (EM) model" and "charge transfer (CT) model". In 1977, Richard Van Duyne and his group confirmed the SERS phenomena and firstly proposed the EM enhancement mechanism.[6] Later, Albrecht and Creighton proposed a CT effect to the mechanisms behind the SERS phenomena[7]. Both Nie and Kneipp groups achieved single-molecule detection independently with different experimental conditions.[8,9]

6.2.1 Electromagnetic model

Let us consider a metal NP with a complex dielectric constant $\varepsilon(\nu) = \varepsilon_1(\nu) + i\varepsilon_2(\nu)$ surrounded by a dielectric constant ε_0 is interacting with a incident light of frequency ν. The diameter of the sphere is $2R$ (R is the radius of NP) and it is assumed to be small compared to the incident wavelength (Rayleigh limit). Then a molecule at a distance r away from the metal surface will then experience the total electric field E_M which is a superposition of incoming field E_0 and the induced electric field from the metal sphere, E_{sp}.

$$E_M = E_0 + E_{sp} \tag{7}$$

where $E_{sp} = E_0 \frac{\varepsilon(\nu)-\varepsilon_0}{\varepsilon(\nu)+2\varepsilon_0}\left(\frac{R}{R+r}\right)^3$ (8)

Then field enhancement factor $A(\nu)$ is the ratio of the field at the position of the molecule to incoming field and can be expressed as below.

$$A(\nu) = \frac{E_M(\nu)}{E_0(\nu)} \sim \frac{\varepsilon(\nu)-\varepsilon_0}{\varepsilon(\nu)+2\varepsilon_0}\left(\frac{R}{R+r}\right)^3 \tag{9}$$

The enhancement takes a maximum value when $\varepsilon(\nu) = -2\varepsilon_0$. Thus, a metal is suitable for use in SERS as it has negative real part of the dielectric function and a small imaginary part of the dielectric function.

The SERS effect has become most popular as the field enhancement process occurs twice in the mechanism of EM model. Initially, the incident field is magnified by localized surface plasmons which will excite the Raman modes of the molecule, thereby increasing the signal of the Raman scattering. The radiative photons (either stokes or anti-stokes) are then amplified by the same mechanism, resulting in a greater increase in the total output signal of the experiment. Taking into account the

enhancing effect at each stage the electromagnetic enhancement factor $G(\nu)$ can be written as

$$G(\nu) \approx |A(\nu)|^2 |A(\nu_s)|^2 \approx \left|\frac{\varepsilon(\nu)-\varepsilon_0}{\varepsilon(\nu)+2\varepsilon_0}\right|^2 \left|\frac{\varepsilon(\nu_s)-\varepsilon_0}{\varepsilon(\nu_s)+2\varepsilon_0}\right|^2 \left(\frac{R}{R+r}\right)^{12} \quad (10)$$

Here $A(\nu_s)$ represent the enhancement factor for stokes or antistokes components. Thus, the enhancement scales as the fourth power of the local field of metal NP and it is strongly enhanced when the excitation and scattered fields are in resonance with the surface plasmons. Moreover, EM SERS enhancement does not require direct contact between molecule and metal but it strongly decreases with increasing distances as $(1/r)^{12}$.[10]

6.2.2 Chemical Enhancement

Another contribution to the SERS scattering is a chemical enhancement which is also referred as charge transfer (CT) and short-range effect. Actually, it has been proved to be very difficult to study the chemical enhancement mechanism selectively for two reasons. First, it is generally thought the contribution has only a factor of 10–10^2 compared to a factor of 10^4–10^7 for EM enhancement. Second, almost any experimental parameters which can be varied to probe a system will have an influence via both mechanisms, making the separation of two effects very difficult. EM enhancement should be a nonselective amplifier for Raman scattering by all molecules adsorbed on a particular surface yet the molecules CO and N_2 differ by a factor of 200 in their SERS intensities under the same experimental conditions.[11] This result is very hard to explain invoking only EM enhancement. The polarizabilities of the molecules are nearly identical and even the most radical differences in orientation upon adsorption could not produce such a large difference. The second evidence comes from potential-dependent electrochemical experiments. When the molecule adsorbed on the 'flat' surface in the nanometer scale, the enhancement factor is dependent on the electrode potential.[11]

Chemical enhancement can be explained by a resonance-like Raman mechanism. Figure 2 depicts the operative charge transfer mechanism for a molecule adsorbed on an electrode. The resonance Raman process is very unlikely because of the large energy gap between the highest occupied molecular orbitals (HOMO) and the lowest unoccupied molecular orbitals (LUMO) in spite of the perturbed redistribution of the energy levels for a molecule adsorbed on a rough surface. However, the resonance Raman scattering can occur through photon-driven charge-transfer processes between the metal and adsorbates. It is assumed that transitions from states near the Fermi level (E_F) are preferred because of favorable matrix elements involving wave function overlap of localized electron density of states. The process occurs 1) with the annihilation of photon by the metal which creates an electron hole pair and the electron is excited as a 'hot electron'. 2) The so called 'hot electron' tunnels into the available energy levels such as LUMO of the adsorbate generating a negatively charged excited molecule. 3) The resulting negative ion, i.e. the complex of the adsorbate molecule and an electron, has a different equilibrium geometry with the original neutral adsorbate molecule. 4) Therefore, the charge transfer process induces a nuclear relaxation in the adsorbate molecule which, after return of the electron to the metal, leads to a vibrationally excited neutral molecule but also to the emission of a Raman shifted photon.

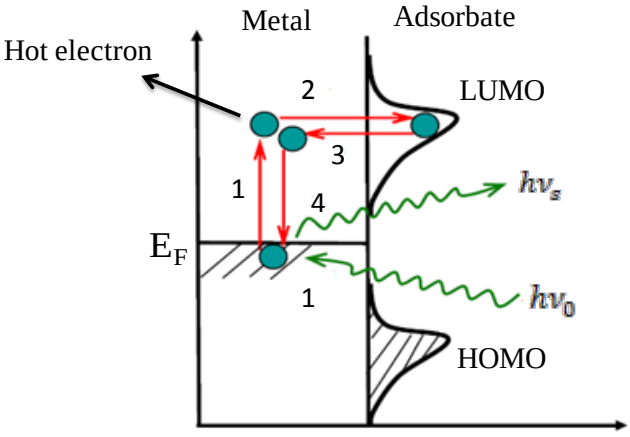

Figure 2: Schematic representation of a charge-transfer mechanism in SERS.

This mechanism is site-specific and analyte-dependent. Although the chemical enhancement mechanism is not a general mechanism and is restricted by its chemical specificity, it can provide useful information uniquely on chemisorptive interactions between metals and adsorbates.

6.3 Micro-Raman studies of silver nanoparticles incorporated polystyrene photonic crystals

Recently, there has been a rapidly growing interest in the fabrication of metal NPs incorporated photonic crystals (PCs) due to their enormous applications like substrates for SERS and as chemical and biological sensors.[12,13] Djaoued et al.[14] have shown that gold NPs embedded polystyrene (PS) PCs enhanced the Raman signal of PS nearly 100 times as compared with a single monolayer of PS. However, in our work silver nanoparticles (AgNPs) were chosen to incorporate them in the crystal structure because of their easiness of preparation and low cost associated with their manufacture.

6.3.1 Experimental Results and Discussion

One of the most popular methods to synthesize AgNPs through chemical methods is by the use of ice-cold sodium borohydride to reduce silver nitrate.[15] A 10-mL volume of 1.0 mM silver nitrate was added dropwise (about 1 drop/second) to 30 mL of 2.0 mM sodium borohydride solution that had been chilled in an ice bath. The reaction mixture was stirred vigorously on a magnetic stir plate. The solution turns light yellow after the addition of 2 mL of silver nitrate ($AgNO_3$) and a brighter yellow when all of the silver nitrate had been added. The entire addition took about three minutes, after which the stirring was stopped and the stirrer was removed. The average size of the NPs obtained in this recipe was 30 nm (calculated from the FESEM pictures) and the peak corresponding to surface plasmon absorption was obtained at 410 nm (Inset of figure 4 shows the absorption spectra of AgNPs). To embed the AgNPs in the PC lattice structure, 1 mL of the colloidal solution

containing around 200 µg/mL of AgNPs were mixed with a solution of 331 nm diameter PS microspheres (weight percent =1). The crystal growth was continued with the same conditions as discussed in the chapter 2. The thickness of the crystal is found to be 5 µm. As presented in figure 3, the AgNPs have settled down on the

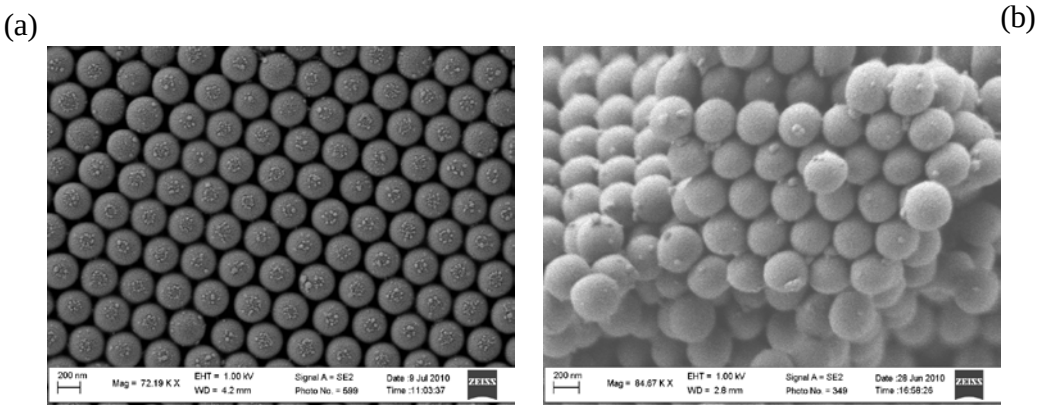

Figure 3: FESEM images of a) surface morphology of (111) Bragg plane and b) cross sectional view of AgNPs incorporated D = 331 PS PC.

surface of the spheres and as well inside the crystal structure because these AgNPs also experiences same capillary forces and convection fluxes as that of PS microspheres. The Raman spectrum of the PC was recorded using micro-Raman spectrometer (HORIBA Jobin Yvon: HR800). A continuous wave (CW) Ar^+ ion laser which delivers a wavelength of 514 nm was employed as an excitation source. The spectrometer was operated in the confocal geometry with a 50X microscope objective. The laser power before the microscope objective was 3 mW. All the spectra were recorded with an average time of 5 sec in the range of 50 - 3500 cm^{-1}. A bare PC (without AgNPs) having the same thickness of AgNP doped PC is used for comparison. The band at 1001 corresponding to ring breathing mode of PS is the most intense peak and the other significant bands at 1602 (C=C), 2909 (CH_2 and CH_3 symmetric and asymmetric vibrations) and 3052 cm^{-1} (CH ring vibrations)[16] were enhanced more than 3 times compared to bare PC. The enhancement is expected due to EM effect as the wavelength of the excitation source is falling at the edges of the surface plasmon absorption peak. The PCs of diameter less than 331

nm possess the stop band in the visible region and consists of smaller interstitial widths compared to larger diameter PCs. For example, the interstitial width (= 0.1547 × D)[17] for D = 331 and 220 nm PCs are 51 and 34 nm respectively. The smaller diameter PCs allows the excitation wavelengths (514, 532 and 633 nm) available with commonly available

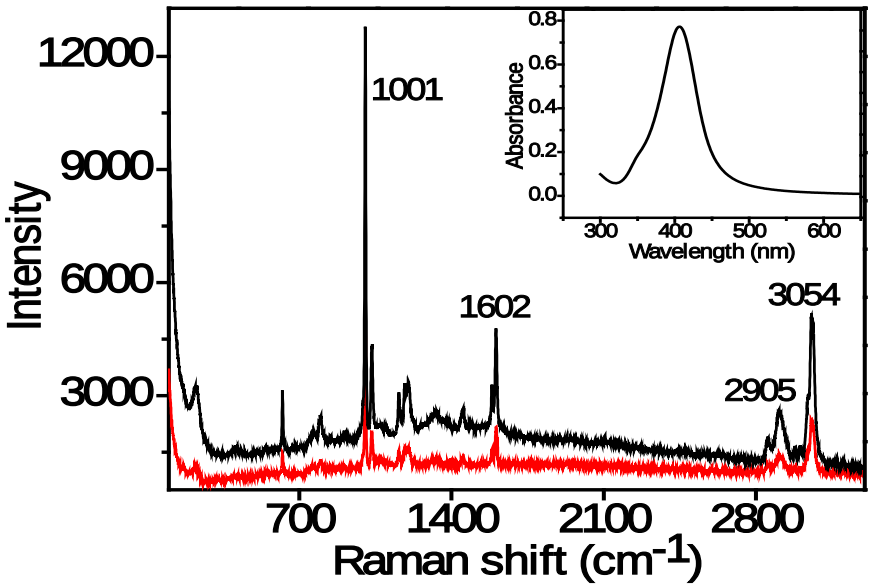

Figure 4: Raman spectra of bare PC (red line) and AgNPs doped PC (black line). Inset shows the absorption spectra of AgNPs.

Raman instrument to fall at the stop band edge at which the interaction time of EM field with the probed material increases[18] and gives multiple enhancements of Raman signal along with the surface plasmon effect. Moreover, the enhancement of Raman signal depends on the concentration of NPs in the probed region.[19] However with the incorporation of higher concentration of AgNPs in the PS solution during the crystal growth yielded whitish colored substrates indicating the destruction of the crystal lattice. The incorporation of volatile solutions[20] and low viscous polymers[21] in the interstitials after PC growth will not affect the crystal structure. We, therefore, decided to incorporate the polymer solution with $AgNO_3$ in the PC and irradiate with laser to create the AgNPs in the interstitials. Hence, we initially undertook the study

on the formation of NPs and their growth during laser irradiation through scattering phenomena.

6.4 In-situ observation of silver nanoparticle formation through micro-Raman studies

In this work, we have made use of a polymer matrix as reducing and capping agent for AgNP formation with an aim to monitor the SERS signals of the polymer, which otherwise would have been difficult to observe. The metal NPs have been synthesized through numerous techniques such as the chemical method,[22,23,24] sputtering[25] and pulsed laser deposition.[26] Advantage in the present experiment is that we would be able to monitor the growth of the AgNPs by observing the SERS signals, where it has been well established in the literature that one requires an optimum size for the NPs to observe maximum SERS signal.[27] Thus, the present experiment deals with the metal NPs homogeneously dispersed in the polymer matrix. Such systems have added advantage of being used as sensors,[28] as materials with solvent switchable electronic properties,[29] as optical data storage,[30,31] surface plasmon enhanced random lasing media[32] etc. Earlier, our group reported the synthesis of Ag and Au NPs in polyvinyl alcohol (PVA) free standing film which involves a sacrificial layer of PS and the biosynthesis of AgNPs towards optical limiting studies.[33]

Photochemical synthesis of AgNPs using high power laser and fluorescent light sources[34,35] is one of the powerful techniques that has recently attracted substantial interest of researchers as it offers a versatile and convenient process with distinguishable advantages such as space selective fabrication. However, there is no literature that talks simultaneously the fabrication as well as its characterization or influence on the surroundings. This study exploits the in-situ synthesis of the NPs by employing CW laser sources such as He-Ne (633 nm), Ar^+ (514 nm) and diode (785 nm) lasers and 6 ns pulsed laser at 532 nm and monitoring the formation of the NPs

through the SERS of the encapsulating molecules. The formation of NPs through laser irradiation was also confirmed through absorption and scattering studies. The formation of NPs within an area of a 1 μm^2, shows its potential in many applications such as memory devices and biomedical applications.

6.4.1 Experimental Details

Thin films of PVA+$AgNO_3$ were prepared by mixing the solutions of 100 mg of $AgNO_3$ dissolved in 5 ml of water and 1.44 gm of PVA (MW = 88,000 gm/mole) dissolved in 30 ml of water and stirring for eight hours for complete miscibility in a dark room to avoid photo-dissociation of silver nitrate. Next, an aliquot solution of 1 ml was uniformly distributed on a 2 cm x 2 cm glass plates using spin coating technique. These homogeneous films were dried in an oven for two hours at 300 K. The thickness of the film was 4 μm. Absorption spectra of these films were taken immediately to confirm that there was no absorption peak in the visible region due to surface plasmon resonance of AgNPs. This confirms that the film does not contain any species of AgNPs before laser irradiation. The work carried out in this paper is divided into four sections. 1) To study the surface plasmon absorption characteristics of AgNPs, the PVA + $AgNO_3$ thin films were irradiated with frequency doubled Nd:YAG laser delivering 532 nm wavelength of pulse width of 6 ns at the repetition rate of 10 Hz. The beam diameter on the film was 8 mm. The energy used for irradiation was 20 mJ. 2) The Raman spectrum of the freshly prepared PVA + $AgNO_3$ films were recorded using Raman spectrometer (HORIBA Jobin Yvon: HR800). CW 514, 633 and 785 nm were used as the excitation wavelengths and the spectrometer was operated in the confocal geometry with a 50x microscope objective. The Raman spectrum was periodically collected at finite time intervals. This was continued till the laser damaged the film. The damage was confirmed through the imaging system. The laser power before the microscope objective for both 514 and 633 nm was 3 mW. We used a higher power level of 20 mW for the excitation source at 785 nm as the lower power levels of 3 and 10 mW did not induce

any changes in the spectra. The Raman spectra were collected from 50 to 3100 cm^{-1} for 514 and 633 nm and 50 to 1200 cm^{-1} for 785 nm at room temperature. The calculated diameters of the focal spots were 0.84, 1 and 1.3 μm, respectively, for the 514, 633 and 785 nm excitations. 3) As recording the in-situ absorption spectra of AgNP formation within a 1 μm^2 area was not possible, a parallel experiment was set up for recording absorption spectra as a function of irradiation time. A 8W diode pumped CW laser at 532 nm (Spectra-Physics, Millennia) was used to achieve nearly the same intensities as that in the confocal-micro-Raman setup over a much larger area so that we could record the absorption spectrum very easily with the absorption spectrometer (JASCO, V-670). 4) An in-situ light scattering experiment to monitor the AgNP formation was carried out in a solution of PVA + $AgNO_3$ using both a pulsed Nd:YAG ns laser and a diode pumped CW laser.

6.4.2 Results and Discussion

6.4.2.1 Studies with nanosecond pulsed laser excitation in polyvinyl alcohol + silver nitrate thin films

Initially, we irradiated the thin films of PVA + $AgNO_3$ with ns laser delivering 532 nm at a rep rate of 10 Hz. The energy and beam diameter were 20 mJ and 8 mm, respectively. We recorded absorption spectra after one minute of exposure time and some of them are shown in figure. 5a. Subsequent to the irradiation time duration of one minute the film changes from originally transparent to yellow color and all the recorded absorption spectra showed a plasmon peak around 426 nm which indicated the formation of AgNPs. Figure 5b shows the FESEM picture of AgNPs obtained after 6^{th} min of irradiation and the corresponding particle size histograms are shown in the inset. The mean diameter of the AgNPs is estimated to be around 12 nm. The intensity of surface plasmon absorption was found to be increasing with successive irradiations as shown in figure 5a. This could be attributed to the formation of more number of AgNPs with continued exposure time. No significant changes were observed in the peak position of the absorption spectra obtained with increasing

irradiations. Very few NPs of larger size were also observed after 6th min of irradiation but they did not show any significant changes in shifting of the peak positions.

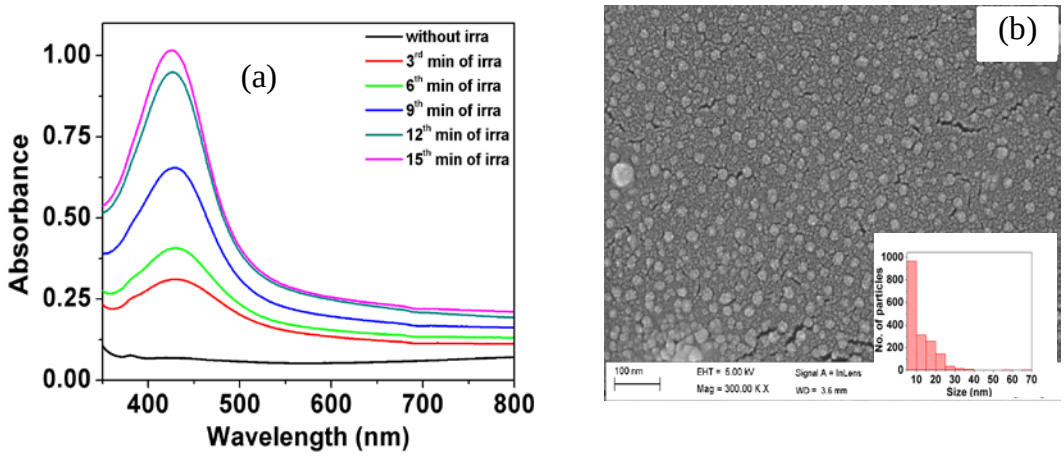

Figure 5: a) Absorption spectra recorded with increasing number of irradiations using ns laser. b) FESEM picture of AgNPs and (inset) the corresponding size histograms at 6th min of irradiation.

Significant efforts have been made to investigate the mechanisms involved in the formation of AgNPs which are synthesized through the photo synthesis method.[36] Kutsenko et al.[37] explained the photo synthesis of AgNPs in the PVA matrix which were formed with mercury lamp irradiation. According to their proposal, the reduction of Ag^+ ions into AgNPs was accompanied by the formation and stabilization of hydroxyl radicals.

6.4.2.2 Confocal-micro-Raman studies on SERS

The spectra obtained from figures 6 to 8 show the effect on the Raman bands of PVA due to the SERS of AgNPs. With subsequent irradiations, we observed a drastic increase in the intensity of the Raman bands. Our discussions below focus on the effect of 514, 633 and 785 nm excitations. In each case, the spectra were recorded in time duration of one minute (where the laser in the confocal-micro-Raman

spectrometer was used as the excitation source and forms the heat source for generating AgNPs). The time duration for each collection was 15 seconds.

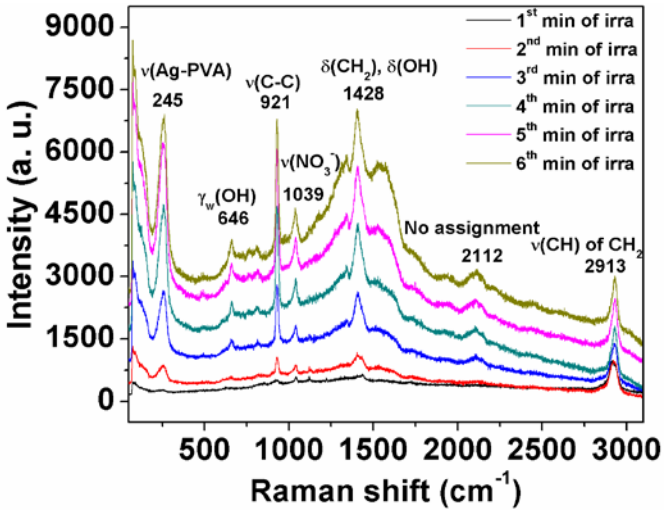

Table 1

Raman bands of PVA as given in literature (cm^{-1})	Assignment
245	ν(Ag-PVA)
479	δ(C-O), CH out of plane
646	γ_w (OH)
818	No assignment
921	ν(C-C)
1121	C-OH valence asymmetric ring vibrations
1343	γ_w (CH_2), δ(OH)
1428	δ(CH_2)
1723	ν(C=O) residual acetate
2112	No assignment
2913	ν(CH) of (CH_2)

Figure 6: Raman spectra of PVA+$AgNO_3$ film recorded with subsequent irradiations using the excitation wavelength of 514 nm. Table 1 summarizes the most pronounced bands of PVA and Ag-PVA composite. ν = stretching, δ = bending, γ_w = wagging.

Table 1 summarizes the most pronounced Raman bands of pure PVA and their corresponding assignments given in the literature.[38,39,40] A new band at 245 cm^{-1} starts appearing with irradiation and it corresponds to the stretching vibrational frequency of the Ag-PVA composite.[40]

6.4.2.3 514 nm CW excitation

Raman spectra were recorded for the PVA with $AgNO_3$ casted films using confocal-micro-Raman setup. With the 514 nm irradiation, the bands at 245, 646, 921, 1039, 1428, 2112 and 2913 cm^{-1} were clearly seen and show large intensity changes with increasing laser irradiations as shown in figure 6. The bands at 245, 646, 921 and 2913 cm^{-1} are blue-shifted monotonically by 8, 16, 9 and 8 cm^{-1} respectively. The band at 1039 cm^{-1} which corresponds to a stretching vibration of a nitrate ion[41] did not show any shift. The band at 1428 cm^{-1} was red shifted by 17 cm^{-1} after the 5^{th} min of irradiation. The band at 1343 cm^{-1} does not appear after the initial 1^{st} min of irradiation but appears after the 2^{nd} min of irradiation and attains maximum intensity at the 4^{th} min of irradiation. It did not show any shift in its energy. Similarly, the band at 2112 cm^{-1} appears at the 3^{rd} min of irradiation and did not show any shift. Interestingly, we observed that the band at 1121 cm^{-1} disappear after the 3^{rd} min of irradiation and the possible reasons for this behavior and the shifting of the bands are discussed later.

6.4.2.4 633 nm CW excitation

Compared to 514 nm irradiation, 633 nm irradiation took a long time to observe the changes in the intensities of the Raman bands of PVA. With this irradiation, only bands at 245, 818, 921, 1039, 1428 and 2913 cm^{-1} show clear enhancement as shown in figure 7.

The band at 245 cm^{-1} was blue-shifted by 9 cm^{-1} at the 18^{th} min of irradiation and did not show any shift with further irradiation. The bands at 818, 921, 1039 and 2913 cm^{-1} did not show any shift. The band at 1428 cm^{-1} was red-shifted by 17 cm^{-1} at the 18^{th} min of irradiation and did not show any shift with further irradiation. The band at 1121 cm^{-1}, which disappeared with 514 nm irradiation was seen throughout the 633 nm laser irradiation. A very weak band at 1723 cm^{-1} corresponding to the stretching vibration of a residual carbonyl group is found with both 514 nm and 633

nm irradiations. The experimental data thus give evidence of the change of the alcohol group to a carbonyl group which has been established as the route to the formation of AgNPs.

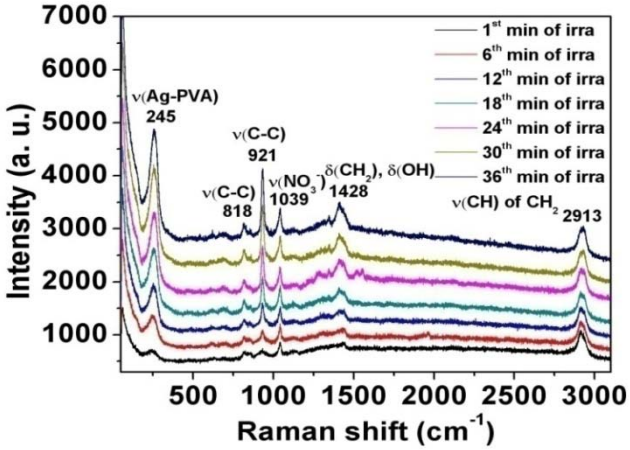

Figure 7: Raman spectra of PVA+$AgNO_3$ film recorded with subsequent irradiations using the excitation wavelength of 633 nm.

6.4.2.5 785 nm CW excitation

The 785 nm laser irradiation had a much weaker effect on the formation of the AgNPs as could be noticed from the Raman spectral enhancement (6th min of

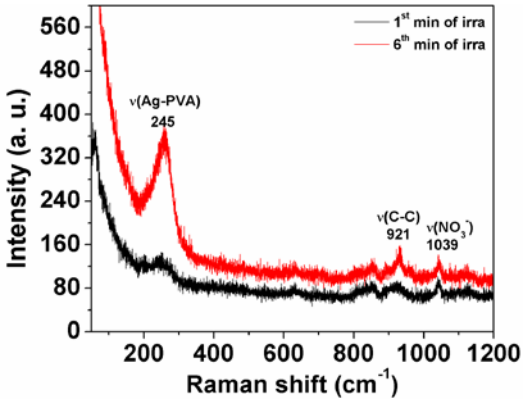

Figure 8: Raman spectra of PVA+$AgNO_3$ film recorded with subsequent irradiations using the excitation wavelength of 785 nm.

irradiation) as shown in figure 8, where the bands corresponding to 245, 921 and 1039 cm^{-1} only appear.

Other than PVA and Ag-PVA bands, low frequency bands at 141, 88 and 76 cm^{-1} were also observed. These low frequency bands were labeled as lattice vibrations of AgNPs[42]. These bands were not present in the spectra at the 1st min of irradiation with any of the three excitations, 514, 633 and 785 nm, but appeared only after longer irradiation dose. The broad peak that appears at 141 cm^{-1} was blue shifted by 11 cm^{-1} in the case of 514 nm irradiation and is comparatively weak with 633 nm irradiation. This indicates that fewer NP form with 633 nm irradiation. The other two low frequency bands (76 and 88 cm^{-1}) were obscured in the case of 633 nm irradiation. Moreover, these low frequency bands were not seen in the case of 785 nm irradiation.

The sample was found to get damaged after the 6, 38 and 6th min of irradiation with the 514, 633 and 785 nm excitation wavelengths respectively. The relative enhancement factor (EF) for each band with each irradiation was calculated as EF = $I_n{}^{th}{}_{irrad}$/ $I_1{}^{st}{}_{irrad}$, where $I_n{}^{th}{}_{irrad}$ and $I_1{}^{st}{}_{irrad}$ are the intensities at the n^{th} min of irradiation and the 1st min of irradiation for each band. We considered only those bands that

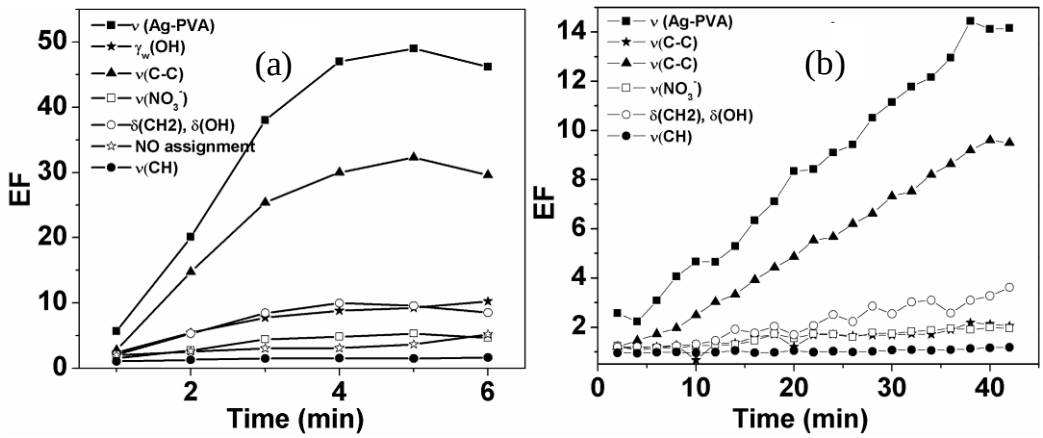

Figure 9: EF for each band calculated with subsequent irradiations using the excitation wavelengths of a) 514 and b) 633 nm.

showed a large change with increasing irradiations to calculate the EF. These bands are 245, 646, 921, 1039, 1428, 2112 and 2913 cm^{-1}. The major difference in the EFs was that the bands of PVA show faster enhancement with 514 nm irradiation compared to 633 nm irradiation with the same power level as shown in figure 9a and 9b.

In both cases, the bands at 245 and 921 cm^{-1} gained maximum enhancement compared to other bands. However, the characteristic band at 2913 cm^{-1} corresponding to the CH stretching vibration of CH_2 did not show any significant enhancement on the formation of AgNPs.

The enhancement of different bands was expected due to the formation of AgNPs. Once the AgNPs are formed with the laser irradiation, the same incident wavelength would excite the surface plasmons simultaneously and this results in producing a localized EM field around the AgNPs. This localized EM field is proportional to the square of the inverse of the wavelength and the difference of the dielectric constants of metal NPs and the surrounding media.[19] In our study, the excitation source 514 nm is closer to the surface plasmon resonance maxima, while the 633 and 785 nm excitations are far from the surface plasmon resonance maximum. Hence, the EFs for different bands with a 514 nm excitation source were large compared to the 633 nm excitation source as shown in figure 9a and 9b. As 785 nm is far from the surface plasmon absorption of AgNPs and the absorption region of PVA, the yield of NPs and the increase in the EFs of the PVA bands is very small compared to the other two excitation sources. This localized EM field also decays exponentially with a distance r from the metal surface as r^{-3}. To experience the maximum enhancement, the molecule must be within 2 nm of the metal surface.[10] As PVA caps around the NPs, the enhancement obtained in the present study is maximum.

Metal NPs absorb the light up to several times their geometrical cross section if the incident wavelength falls in the region of surface plasmon absorption which results in the effect of local induced heating.[43] The local induced heating around the NP causes a rise in temperature and it is greater for 514 nm compared to 633 and 785 nm. Hence, we observed a drastic increase in the EF of bands of PVA with 514 nm irradiation using the same power level in shorter time duration. This gave evidence of the cumulative production of AgNPs with 514 nm irradiation. A more detailed explanation of temperature increase due to AgNPs formed with 514 nm irradiation is provided in the section **6.4.2.7.**

As the AgNPs get heated, polymer chains move far apart due to which a weakening of H bonds and a decrease in the streak of the carbon skeleton chains occur. This results in either a blue or red shift of the corresponding bands of PVA. The PVA gets adsorbed on the surface of the resulting AgNPs as a capping agent due to which the stretching of the Ag-PVA band occurs and is blue shifted with the increased amount of AgNPs. As the number density of the AgNPs and their size increases, the absorption of the laser increases. This induces more heat in the surrounding area resulting in the formation of a greater number of AgNPs. The disappearance of the 1121 cm^{-1} band after the 3rd min of irradiation in the case of 514 nm irradiation could be due to the cleavage of the C-(OH) bonds in PVA surrounding the AgNPs.[44] Since the heat generated with 633 nm excitation is very small, this 1121 cm^{-1} band does not disappear.

6.4.2.6 Studies with CW laser excitation in thin films of polyvinyl alcohol + silver nitrate

In order to have a good comparison of absorption of the AgNPs that were formed with the irradiation of the CW laser used for the Raman spectra collection, we recorded the absorption spectra for the same thin films for every minute by irradiating them with the 532 nm CW laser as shown in figure 10. The power (around 8W) and the beam dimensions of the CW laser were selected in such a way

to get approximately the same intensity as that of 514 nm used in the micro-Raman studies.

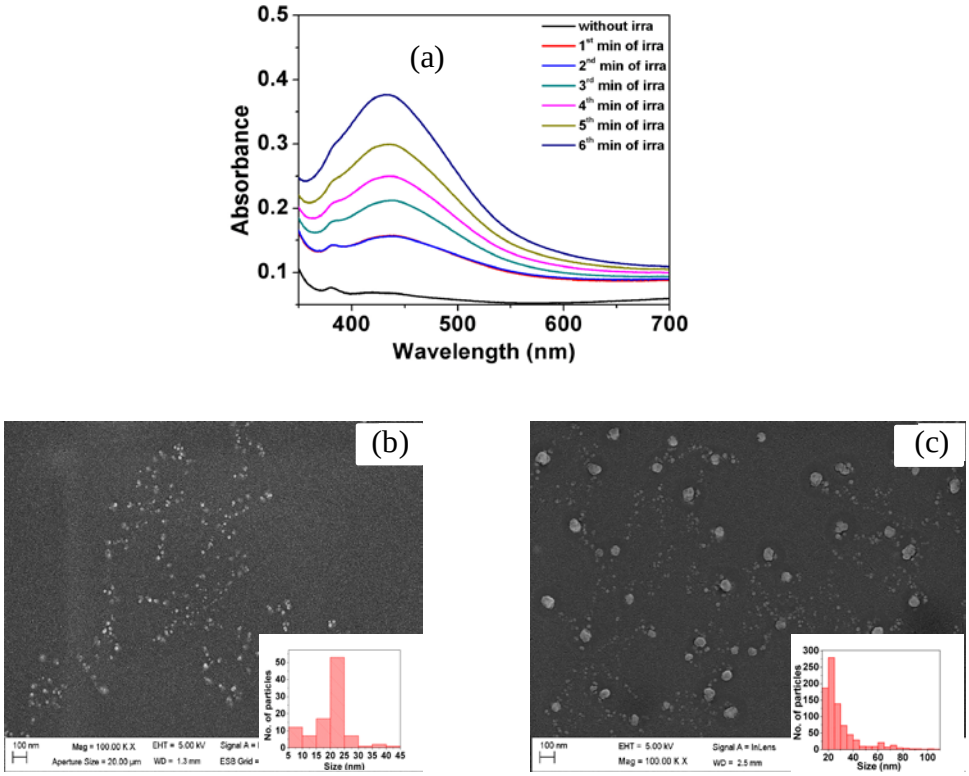

Figure 10: a) Absorption spectra recorded with increasing number of irradiations using CW 532 nm laser at 8W power. FESEM pictures of AgNPs and (insets) the corresponding size histograms at b) 3rd and c) 6th min of irradiation.

The surface plasmon absorption peak appears at 432 nm and did not show any shift for subsequent irradiation doses as shown in figure 10a. Figure 10b and 10c show the FESEM pictures of AgNPs obtained at 3rd and 6th min of irradiations. The picture obtained at 6th min of irradiation also contains larger size NPs which might have formed through agglomeration of smaller size NPs. The particle size histograms (insets of figure 10b and 10c) of AgNPs obtained at 3rd and 6th min of irradiations show that mean diameters are 20 and 30 nm, respectively. Subsequent irradiations result in an increase of amplitude of absorption peak similar to that of ns laser irradiation. The observed full width at half maxima (FWHM) at 6th min of irradiation

is 110 nm which is larger than the FWHM obtained at 15th min of irradiation with ns laser (74 nm). This may be because the CW beam creates larger number of seed particles and resulting in the formation of particles with wider distribution in size. It has also been established that the pulsed laser breaks the larger sized particles into smaller ones.[26] Therefore the absorption spectra with the pulsed laser irradiation are narrower than with the CW laser irradiation. It has been noticed that with CW laser beam irradiation, the particle size does not increase monotonically but reaches a maximum of around 30 nm and any further irradiation lead to the damage of the surrounding PVA matrix as mentioned earlier.

A corresponding shift was not observed for the surface plasmon absorption peaks obtained with different irradiations even though the FESEM pictures of 10b and 10c show different average sizes of NPs. This could probably due to much smaller number of larger size NPs compared to smaller size NPs.

6.4.2.7 Heat generation due to silver nanoparticles

The absorption laser radiation by the free electrons in metal NPs cause strong heating effects. The incident electric field of laser wavelength that falls wihin the surface plasmon absorption band strongly drives the free electrons inside the nanocrystals and the energy gained by free electrons turn into heat. Then the heat diffuses away from the NP and leads to an elevated temperature of the surrounding medium. By solving the heat transfer equation in the absence of phase transformations, one can estimates the increase in the local temperature around a single NP.[45] For an ensemble of metal NPs, the local temperature enhances dramatically as the heat flux from individual NP can be added. The increase in the temperature of a structure which consist of $'N'$ NPs embedded in a matrix of dielectric constant ε_0 and are separated by a distance Δ, can be calculated as below. [45,46]

$$\Delta T_{tot} \approx \Delta T_{max} \frac{R}{\Delta} N^{\frac{n-1}{n}} \quad (11)$$

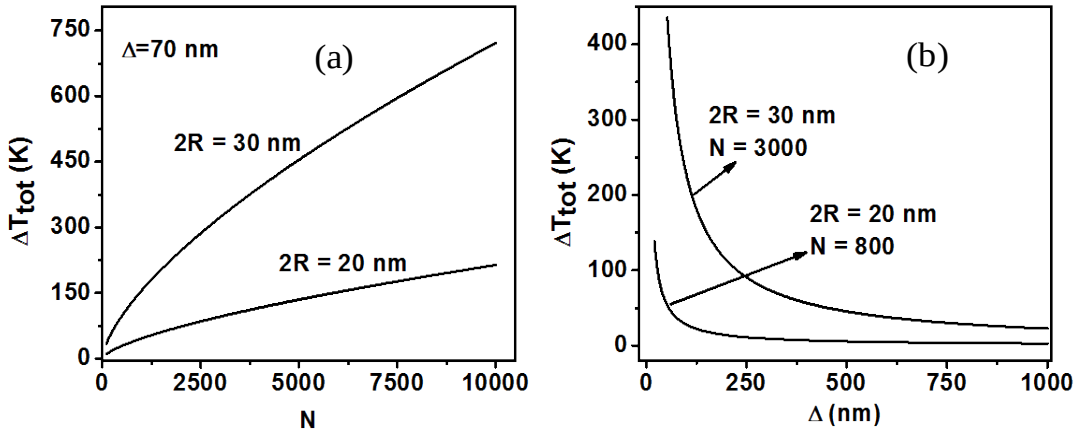

Figure 11: The increase in temperature (ΔT_{tot}) with a) number of particles (N) and b) average distance between particles (Δ) for $2R$ = 20 and 30 nm, respectively.

Here, ΔT_{max} describes the temperature due to a single NP of radius R and can be expressed as given below.

$$\Delta T_{max} = \frac{2\pi R^2 I_0 Im(\varepsilon_{NP})}{3k_0\lambda}\left|\frac{3\varepsilon_0}{2\varepsilon_0+\varepsilon_{NP}}\right|^2 \quad (12)$$

where ε_{NP} is the complex dielectric constant of metal NP, I_0 and λ are the intensity and wavelength of light irradiation, k_0 is the thermal conductivity of the surrounding medium and n is the dimension of the structure. The equation 11 is valid only when the particles are separated by a distance more than the size of the NP.

From equation 11, it can be inferred that ΔT_{tot} increases with the number of metal NPs $'N'$. Hence, the increase in the value of absorbance at each irradiation with 532 nm CW laser (as shown in figure 10a) indicate the increased NP formation at each step of irradiation which leads to the increase in the temperature ΔT_{tot}. Using Equations 11 and 12, we approximated the increase in the temperature at 3rd and 6th irradiation by counting the number of AgNP from FESEM pictures shown in figure 10b and 10c respectively. From histograms, the particle number on the surface is estimated to be around 100 and 750 for 3rd and 6th irradiations, respectively. The average distance Δ between the AgNP is calculated to be around 70 nm. With the

assumption of same number of particles formation along the thickness direction, the maximum number of particle yield in the area of focal spot with 3rd and 6th irradiations are 800 and 3000, respectively. The value of ε_{NP}= -9.2767+0.4041i for 514 nm is calculated using equations available in reference 47. For the values of k_0=0.0046 W/cm/K,[48] ε_0=2.403 and I_0 = 5.42 x 10^5 W/cm^2, the calculated increase in temperatures ΔT_{tot} with the variation of N and Δ for $2R$ = 20 and 30 nm are presented in figure 11a and 11b. From figure 11a, the ΔT_{tot} = 40K, which indicates the increase in temperature after the 3rd irradiation. This increase in temperature additionally causes the formation of more number of NPs along with the photo synthesis process as the chemical synthesis of AgNPs requires only a minimum temperature of 323 K.[49] Thus, the temperature increase with each irradiation generates the excess number of AgNP and leads to increase in the Raman signal of PVA as shown in figure 6. The increased number of AgNPs which form after 6th irradiation causes the ΔT_{tot} = 323K. As the melting temperature of PVA is around 500 K and the calculated temperature after the 6th irradiation is greater than this temperature and any further irradiation will damage the film, which is observed through microscope. As the real part of the dielectric constant of the Ag decreases with longer wavelengths,[2] less amount of heat might have been generated compared with 514 nm irradiation causing the damage of the film after 36th irradiation in the case of 633 nm and 6th irradiation in the case of 785 nm with higher power.

It needs to be mentioned here that the calculated increase in temperature due to surface plasmon absorption of AgNPs is only approximate as the exact calculations require the exact count of NPs, their average separation, photon flux and thermal diffusion coefficient, etc.

6.4.3 Light scattering in a pure solution of polyvinyl alcohol + silver nitrate

We observed scattering of light with the formation of NPs, when the solution containing PVA+$AgNO_3$ was irradiated with 532 nm pulsed laser, while the films

did not show any scattering. Further, we did not observe any scattering with 514, 633 and 785 nm CW laser excitations either in thin films or solutions.

A freshly prepared solution of PVA+$AgNO_3$ was taken in a cuvette of 100 μm thickness and the ns laser beam was focused on the sample with a lens of focal length f = 120 mm. The cuvette was kept exactly at the focus and the intensity at the focal spot was estimated as 1MW/cm^2.

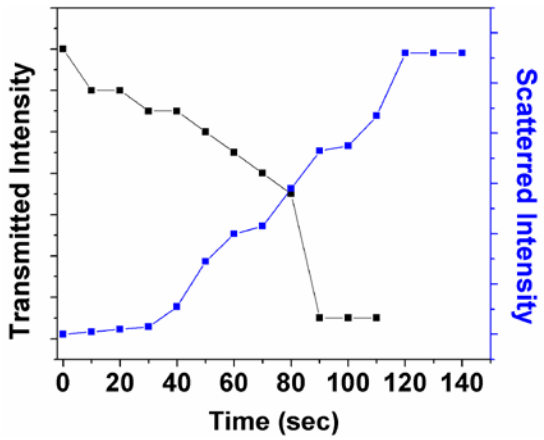

Figure 12: Black line represents transmitted intensity versus time which is observed in the beam direction of incidence and blue line represents scattered intensity versus time which is collected at an angle of 10° respectively.

We recorded both transmitted and scattered (at 10° angle) intensities using a silicon photodiode which was connected to a boxcar averager. The details of the experimental set up have described earlier.[50] Figure 12 shows the recorded transmitted and scattered intensities with time, where we do not observe any scattering for the first 30 sec. After 30 sec we observe a continuous increase in the scattered signal with the formation of AgNPs. With increase in the size of the particles and the number density, the absorption cross-section increases. This increase in absorption due to the localized surface plasmon band then results in an increase in local temperature. It is also a known fact from the literature that the $AgNO_3$ breaks up leading to the formation of NO_2 gas[51] while forming the NP. With

pulse excitations, the NO_2 gas would be close to the irradiation region and then it slowly diffuses into the solution with time. We, therefore, expect the formation of a microbubble around the irradiation area consisting the AgNPs,[52] which then leads to scattering of light when excited with pulsed laser. No scattering was observed with CW laser excitation as the NO_2 gas diffuses through the solution. Similarly, we observe decrease in the transmitted light with irradiation time. The scattering reach saturation after sometime. This is well expected as the number of Ag^+ ions are limited leading to a limit to the number density.

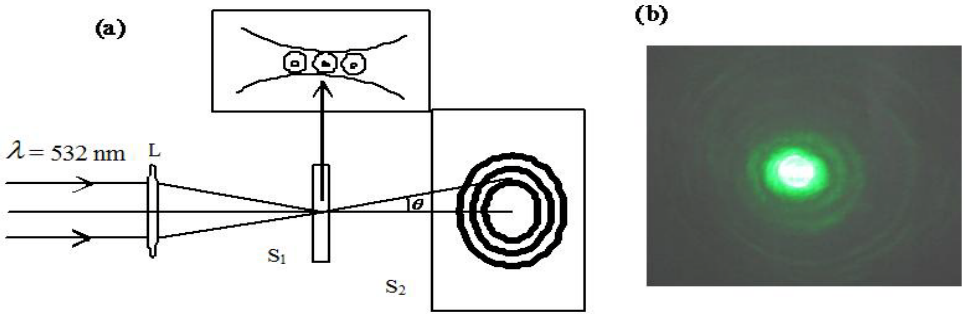

Figure 13: a) Schematic diagram of the circular aperture diffraction pattern which is formed due to a microbubble around AgNP. L: lens, S_1: sample, S_2: screen, ⊙ :microbubble around AgNP. b) Snap shot of scattering which contains circular fringes in the far field pattern at the intensity of 1 MW/cm^2.

Earlier studies[53,54,55] also indicated the formation of a bubble around the AgNP leading to Mie scattering. The formation of the bubble along the path of the focused beam is shown in figure 13a. The Rayleigh range and laser beam waist at the focus were calculated as 4.3 mm and 27 μm respectively. We observed diffraction rings in the far-field as shown in figure 13b, which was captured on a white paper in the transverse direction to the beam propagation and recorded with a CCD camera. The formation of diffraction rings is explained by assuming the formation of microbubble in the path of the beam as shown in figure 13a. Ignoring the size of the NPs, this bubble acts as a circular aperture leading to diffraction rings in the far field.[56] The aperture size was estimated using the formula:[57] $\sin\theta = 1.22\lambda / d$, where θ, d and λ

are the angle between the center of the axis and the first dark fringe, aperture diameter and incident wavelength, respectively as shown in figure 13a. The calculated aperture size d = 14 μm gives the approximate bubble size formed in this experiment. We did not observe any scattering with thin films which were 4 μm thickness, as NO_2 from the $AgNO_3$ dissociation could possibly have escaped out of the film very easily.

6.5 Conclusions

In this work, the in-situ monitoring of AgNP formation was studied for the first time to the best of our knowledge in thin films and solutions using CW laser source and pulsed lasers. We proposed observation of SERS and scattering as the novel and simple techniques to record the growth of AgNPs in PVA films and solutions. Observed enhancement in the Raman bands of PVA were explained through the localized surface plasmon resonance of AgNPs. Influence of the excitation wavelength on the enhancement of Raman modes of PVA with 514, 633 and 785 nm excitations was compared. Formation of the surface plasmon of AgNPs in films and solutions was confirmed through absorption and FESEM recordings. The appropriate reasons for the formation of AgNPs were exploited in terms of local temperatures generated by AgNPs along with the photosynthesis process. The in-situ monitoring of the scattering in solutions was also carried out. The scattering was explained through the formation of microbubble around the AgNPs. As we did not observe any band corresponding to Ag-O (200 cm^{-1}) stretching vibration, this method provides oxidation free AgNPs for SERS studies, where the molecules of our interest can be mixed with the PVA solution. This simple method may open a new window to infiltrate the precursor solution of metal NPs in the opal and inverse opal structures to explore the combined effect of localized surface plasmons and photonic band gap effect in the enhancement of Raman signal of the probed materials.

6.6 References

1. Long, D. A. *The Raman Effect: A Unified Treatment of the Theory of Raman Scattering by Molecules.* (Wiley: 2001).
2. Ru, E. L. & Etchegoin, P. *Principles of Surface-Enhanced Raman Spectroscopy: and related plasmonic effects.* (Elsevier Science: 2008).
3. Ferraro, J. R. & Nakamoto, K. Introductory Raman Spectroscopy. (Academic Press: 1994).
4. Maier, S. A. *Plasmonics: Fundamentals And Applications.* (Springer: 2007).
5. Fleischmann, M., Hendra, P. J. & McQuillan, A. J. Raman spectra of pyridine adsorbed at a silver electrode. *Chemical Physics Letters* **26**, 163–166 (1974).
6. Jeanmaire, D. L. & Van Duyne, R. P. Surface raman spectroelectrochemistry: Part I. Heterocyclic, aromatic, and aliphatic amines adsorbed on the anodized silver electrode. *Journal of Electroanalytical Chemistry and Interfacial Electrochemistry* **84**, 1–20 (1977).
7. Albrecht, M. G. & Creighton, J. A. Anomalously intense Raman spectra of pyridine at a silver electrode. *Journal of the American Chemical Society* **99**, 5215–5217 (1977).
8. Nie, S. & Emory, S. R. Probing Single Molecules and Single Nanoparticles by Surface-Enhanced Raman Scattering. *Science* **275**, 1102–1106 (1997).
9. Kneipp, K. et al. Single Molecule Detection Using Surface-Enhanced Raman Scattering (SERS). *Phys. Rev. Lett.* **78**, 1667–1670 (1997).
10. Kneipp, K., Kneipp, H., Itzkan, I., Dasari, R. R. & Feld, M. S. Surface-enhanced Raman scattering and biophysics. *Journal of Physics: Condensed Matter* **14**, R597–R624 (2002).
11. Campion, A. & Kambhampati, P. Surface-enhanced Raman scattering. *Chemical Society Reviews* **27**, 241 (1998).
12. Lu, L. et al. Controlled Fabrication of Gold-Coated 3D Ordered Colloidal Crystal Films and Their Application in Surface-Enhanced Raman Spectroscopy. *Chem. Mater.* **17**, 5731–5736 (2005).
13. Jiang, C., Markutsya, S., Pikus, Y. & Tsukruk, V. V. Freely suspended nanocomposite membranes as highly sensitive sensors. *Nature Materials* **3**, 721–728 (2004).
14. Djaoued, Y. et al. Micro-Raman spectroscopy study of colloidal crystal films of polystyrene-gold composites. *Appl Spectrosc* **61**, 1202–1210 (2007).
15. Fang, Y. Optical absorption of nanoscale colloidal silver: Aggregate band and adsorbate-silver surface band. *The Journal of Chemical Physics* **108**, 4315–4318 (1998).
16. section2.htm. at <http://www.ijvs.com/volume5/edition3/section2.html>
17. Pozas, R., Mihi, A., Ocaña, M. & Míguez, H. Building Nanocrystalline Planar Defects within Self-Assembled Photonic Crystals by Spin-Coating. *Advanced Materials* **18**, 1183–1187 (2006).
18. von Freymann, G., John, S., Wong, S., Kitaev, V. & Ozin, G. A. Measurement of group velocity dispersion for finite size three-dimensional photonic crystals in the near-infrared spectral region. *Applied Physics Letters* **86**, 053108–053108–3 (2005).
19. Tiwari, V. S. et al. Non-resonance SERS effects of silver colloids with different shapes. Chemical *Physics Letters* **446**, 77–82 (2007).
20. Shadak Alee, K., Sriram, G. & Narayana Rao, D. Spectral and morphological changes of 3D polystyrene photonic crystals with the incorporation of alcohols. *Optical Materials* **34**, 1077–1081 (2012).
21. Bertone, J. F., Jiang, P., Hwang, K. S., Mittleman, D. M. & Colvin, V. L. Thickness Dependence of the Optical Properties of Ordered Silica-Air and Air-Polymer Photonic Crystals. *Phys. Rev. Lett.* **83**, 300–303 (1999).
22. Porel, S., Singh, S. & Radhakrishnan, T. P. Polygonal gold nanoplates in a polymer matrix. *Chemical Communications* 2387 (2005).doi:10.1039/b500536a
23. Porel, S., Singh, S., Harsha, S. S., Rao, D. N. & Radhakrishnan, T. P. Nanoparticle-Embedded Polymer: In Situ Synthesis, Free-Standing Films with Highly Monodisperse Silver Nanoparticles and Optical Limiting. *Chem. Mater.* **17**, 9–12 (2004).
24. Zhang, J. & Noguez, C. Plasmonic Optical Properties and Applications of Metal Nanostructures. *Plasmonics* **3**, 127–150 (2008).

25. Upender, G. et al. Silver nanocluster films as novel SERS substrates for ultrasensitive detection of molecules. *Chemical Physics Letters* **511**, 309–314 (2011).
26. Resta, V. et al. Sharpening the shape distribution of gold nanoparticles by laser irradiation. *Journal of Applied Physics* **100**, 084311–084311–6 (2006).
27. Sant'Ana, A. C., Rocha, T. C. R., Santos, P. S., Zanchet, D. & Temperini, M. L. A. Size-dependent SERS enhancement of colloidal silver nanoplates: the case of 2-amino-5-nitropyridine. *Journal of Raman Spectroscopy* **40**, 183–190 (2009).
28. McFarland, A. D. & Van Duyne, R. P. Single Silver Nanoparticles as Real-Time Optical Sensors with Zeptomole Sensitivity. *Nano Lett.* **3**, 1057–1062 (2003).
29. Holmes, J. D., Johnston, K. P., Doty, R. C. & Korgel, B. A. Control of Thickness and Orientation of Solution-Grown Silicon Nanowires. *Science* **287**, 1471–1473 (2000).
30. Ouyang, J., Chu, C.-W., Szmanda, C. R., Ma, L. & Yang, Y. Programmable polymer thin film and non-volatile memory device. *Nature Materials* **3**, 918–922 (2004).
31. Ouyang, J., Chu, C.-W., Sieves, D. & Yang, Y. Electric-field-induced charge transfer between gold nanoparticle and capping 2-naphthalenethiol and organic memory cells. *Applied Physics Letters* **86**, 123507 (2005).
32. Hao, F., Nehl, C. L., Hafner, J. H. & Nordlander, P. Plasmon Resonances of a Gold Nanostar. *Nano Lett.* **7**, 729–732 (2007).
33. Sathyavathi, R., Krishna, M. B. M. & Rao, D. N. Biosynthesis of silver nanoparticles using Moringa oleifera leaf extract and its application to optical limiting. *J Nanosci Nanotechnol* **11**, 2031–2035 (2011).
34. Tilaki, R. M., Iraji zad, A. & Mahdavi, S. M. Stability, size and optical properties of silver nanoparticles prepared by laser ablation in different carrier media. *Applied Physics A: Materials Science & Processing* **84**, 215–219 (2006).
35. Kim, J.-H., Lavin, B. W., Burnett, R. D. & Boote, B. W. Controlled synthesis of gold nanoparticles by fluorescent light irradiation. *Nanotechnology* **22**, 285602 (2011).
36. Sakamoto, M., Fujistuka, M. & Majima, T. Light as a construction tool of metal nanoparticles: Synthesis and mechanism. *Journal of Photochemistry and Photobiology C: Photochemistry Reviews* **10**, 33–56 (2009).
37. Kutsenko, A. & Granchak, V. Photochemical synthesis of silver nanoparticles in polyvinyl alcohol matrices. *Theoretical and Experimental Chemistry* **45**, 313–318 (2009).
38. Krimm, S., Liang, C. Y. & Sutherland, G. B. B. M. Infrared spectra of high polymers. V. Polyvinyl alcohol. Journal of Polymer Science **22**, 227–247 (1956).
39. Tobin, M. C. *Laser Raman spectroscopy.* (Wiley-Interscience: 1971).
40. Badr, Y. & Mahmoud, M. A. Enhancement of the optical properties of poly vinyl alcohol by doping with silver nanoparticles. *Journal of Applied Polymer Science* **99**, 3608–3614 (2006).
41. Oliver, B. G. & Janz, G. J. Raman spectra of silver nitrate in water-acetonitrile mixtures. *J. Phys. Chem.* **74**, 3819–3822 (1970).
42. Roy, D. & Furtak, T. E. Evidence for Ag cluster vibrations in enhanced Raman scattering from the Ag/electrolyte interface. *Chemical Physics Letters* **124**, 299–303 (1986).
43. Harris, N., Ford, M. J., Cortie, M. B. & McDonagh, A. M. Laser-induced assembly of gold nanoparticles into colloidal crystals. *Nanotechnology* **18**, 365301 (2007).
44. Iwamoto, R., Miya, M. & Mima, S. Determination of crystallinity of swollen poly(vinyl alcohol) by laser Raman spectroscopy. *Journal of Polymer Science: Polymer Physics Edition* **17**, 1507–1515 (1979).
45. Govorov, A. O. et al. Gold nanoparticle ensembles as heaters and actuators: melting and collective plasmon resonances. *Nanoscale Research Letters* **1**, 84 (2006).
46. Govorov, A. O. & Richardson, H. H. Generating heat with metal nanoparticles. *Nano Today* **2**, 30–38 (2007).
47. Slistan-Grijalva, A. et al. Classical theoretical characterization of the surface plasmon absorption band for silver spherical nanoparticles suspended in water and ethylene glycol. *Physica E: Low-dimensional Systems and Nanostructures* **27**, 104–112 (2005).

48. Krishna Bama, G., Indra Devi, P. & Ramachandran, K. Structural and thermal properties of PVDF/PVA blends. *Journal of Materials Science* **44**, 1302–1307 (2009).
49. Porel, S., Venkatram, N., Narayana Rao, D. & Radhakrishnan, T. P. In Situ Synthesis of Metal Nanoparticles in Polymer Matrix and Their Optical Limiting Applications. *Journal of Nanoscience and Nanotechnology* **7**, 1887–1892 (2007).
50. Venkatram, N., Kumar, R. S. S. & Narayana Rao, D. Nonlinear absorption and scattering properties of cadmium sulphide nanocrystals with its application as a potential optical limiter. *Journal of Applied Physics* **100**, 074309–074309–8 (2006).
51. Kwon, J., Yoon, S. H., Lee, S. S., Seo, K. W. & Shim, I. Preparation of Silver Nanoparticles in Cellulose Acetate Polymer and the Reaction Chemistry of Silver Complexes in the Polymer. *Bulletin of the Korean Chemical Society* **26**, 837–840 (2005).
52. Neumann, J. & Brinkmann, R. Self-limited growth of laser-induced vapor bubbles around single microabsorbers. *Applied Physics Letters* **93**, 033901–033901–3 (2008).
53. Vivien, L. et al. Picosecond and nanosecond polychromatic pump–probe studies of bubble growth in carbon-nanotube suspensions. *Journal of the Optical Society of America B* **19**, 208 (2002).
54. Mansour, K., Soileau, M. J. & Stryland, E. W. V. Nonlinear optical properties of carbon-black suspensions (ink). *Journal of the Optical Society of America B* **9**, 1100–1109 (1992).
55. Nashold, K. M. & Walter, D. P. Investigations of optical limiting mechanisms in carbon particle suspensions and fullerene solutions. *Journal of the Optical Society of America B* **12**, 1228 (1995).
56. Cowley, L., Laven, P. & Vollmer, M. Rings around the sun and moon: coronae and diffraction. *Physics Education* **40**, 51–59 (2005).
57. Born, M. & Wolf, E. *Principles of Optics: Electromagnetic Theory of Propagation, Interference and Diffraction of Light.* (Cambridge University Press: 1997).

CHAPTER 7

Conclusions and future perspectives

7.1 Conclusions

With homemade PS microspheres of different sizes, opal type 3D colloidal photonic crystal (PCs) structures were fabricated using self-assembly method. The surface and cross sectional morphologies were examined with FESEM. The transmission and reflection spectral characteristics were studied using UV-vis-NIR spectrometer. The thickness dependant behavior of transmission spectral characteristics of PCs due to (111) plane were compared with scalar wave approximation and found a good agreement between the experimental and theoretical data. Angle dependent spectral characteristics enabled us to calculate various PC parameters such as interpalnar spacing for different planes and effective refractive index of the crystal structure. The polarization dependent characteristics of PC structures are carried out in the reflection geometry and compared with photonic band structure calculations using RSoft (BandSOLVE). The experimentally observed peak widths of reflection spectra obtained for $\theta>20°$ for unpolarized light do not follow the theoretical bands and they fall in between the bands 1&2 and 3&4. This is not observed by earlier group[1] and they mentioned that the peak widths will merge with the outer band 1&2 only. This observation indicates that the unpolarized light penetrates more into the crystal structure compared to s-polarized light and it is maximum for p-polarized light. The peak height decreases with p- and unpolarized light and remains almost constant for s-polarized light with increasing incident angle can be attributed to Brewster angle phenomenon.

By incorporating different alcohols in the interstitials of PCs, the studies of Bragg diffraction due to various high Miller index (hMi) planes over wide range of incident angles and swelling of micropsheres were exploited. The realization of uniform shifting of stop bands due to hMi Bragg planes in addition to that of the stop band due to (111) plane to the refractive index variation of 10^{-2}, may allow the

improvement in the sensitivity of the PC while allowing us to use it at any incident angle.

Till now optical limiting studies were reported on the various phenomena such as multiphoton absorption, reverse saturable absorption and nonlinear scattering. The enhanced two photon absorption of PS PC at the band edge leads to the reduction in the threshold value of optical limiting. In this connection, a Z-scan experiment is performed at different incident angles using photonic crystals and explored the concept of enhanced electromagnetic fields at the stop band edge due to reduction in the group velocity of light.

A simple phenomenon of incorporation of silver nanoparticles (AgNPs) in the interstitals of opal structure was used in order to achieve enhanced Raman scattering of PS microspheres. In addition, an in-situ formation of AgNPs in PVA matrix was demonstrated in terms of surface enhanced Raman scattering (SERS) technique. In this process different low power CW lasers were used for the formation of AgNPs and as well to collect the enhanced Raman scattering of host matrix simultaneously. The approximate local temperatures due to surface plasmon absorption were calculated which causes the NP formation along with the photo chemical process. An increased scattering with time was observed when the precursor solution of AgNPs is irradiated with nano second laser. Along with the scattering circular aperture diffraction fringe pattern was also observed which indicates the formation of microbubbles along with the AgNPs. From the observed fringe pattern the diameter of the microbubble is estimated as 14 μm.

7.2 Future perspectives

The spectral characteristics due to hMi Bragg planes were resulted at the high energy region as discussed in chapter 3. Our next step is an elaborate study of the polarization dependent reflection/transmission spectral characteristics of hMi Bragg planes using bare and alcohol doped opals which would allow us to exploit some

more interesting results with these good quality PCs. Higher refractive index contrast (more than 2.8) of PC structure resulted into full photonic band gap. Hence, the good quality opal structures fabricated in our work will be used as replica for creating high refractive index contrast inverse silica, titania and zinc sulphide for many photonic applications.[2,3]

This inhibition of emission wavelengths due to photonic stop band of (111) Bragg plane would be very useful in achieving the increased gain at different wavelengths. This change in emission of RhB observed could lead to the realization of low threshold lasers in which control of spontaneous emission is a key factor. This guides us to the next step of fabrication of micro laser system with the RhB doped PC.

The reduction in the group velocity of light mainly depends on the number of layers and refractive index contrast.[4] Calculations show that the refractive index contrast possessed by opals will result in the reduction of light velocity around of 10% of vacuum speed.[4] As cadmium sulphide (CdS) NPs are good candidates for nonlinear absorption[5] and possess high refractive index, creating inverse opals with CdS NPs may reduce the group velocity to a greater extent compared to normal opals and thus resulting in the further reduction of limiting threshold value of optical limiters.

The method of in-situ formation of AgNPs with low power CW laser can be extended to other metals such as gold and copper and as well to their precursor solutions. Extremely intense electromagnetic fields have been observed at “hot spots” and located at gaps between metallic nanostructures that are in the order of tens of nanometers.[6,7] Hence, the precursor solutions of metal NPs can be spin coated on a single layer of PS microspheres to create hotspots in the interstitial gaps which are essential in the realization of effective SERS substrates. Preparation of metal NPs by laser irradiation can hold a tremendous advantage as by irradiating the PS PC with the precursor solutions, metal NPs can easily be dispersed in the PC, which

otherwise is very difficult to prepare a PC with metal NPs by diffusing them through the crystal structure. Thus all might aggregate on the top layer. The same method can be treated to incorporate high refractive index materials such as semiconductor, titanium dioxide and zinc sulphide NPs in a PC structure. This may yield a PC structures with wider band gaps (towards full photonic band gap) and results in larger electric field confinements to enhance the Raman signal of probed molecule.

7.3 References

1. Galisteo-Lopez, J. F., López-Tejeira, F., Rubio, S., López, C. & Sánchez-Dehesa, J. Experimental evidence of polarization dependence in the optical response of opal-based photonic crystals. *Applied Physics Letters* **82**, 4068–4070 (2003).
2. López, C. Materials Aspects of Photonic Crystals. *Advanced Materials* **15**, 1679–1704 (2003).
3. Galisteo-López, J. F. *et al.* Self-Assembled Photonic Structures. *Advanced Materials* **23**, 30–69 (2010).
4. von Freymann, G., John, S., Wong, S., Kitaev, V. & Ozin, G. A. Measurement of group velocity dispersion for finite size three-dimensional photonic crystals in the near-infrared spectral region. *Applied Physics Letters* **86**, 053108–053108–3 (2005).
5. Venkatram, N., Rao, D. N. & Akundi, M. A. Nonlinear absorption, scattering and optical limiting studies of CdS nanoparticles. *Opt Express* **13**, 867–872 (2005).
6. Qian, L. H., Yan, X. Q., Fujita, T., Inoue, A. & Chen, M. W. Surface enhanced Raman scattering of nanoporous gold: Smaller pore sizes stronger enhancements. *Applied Physics Letters* **90**, 153120–153120–3 (2007).
7. Duan, G., Cai, W., Luo, Y., Li, Y. & Lei, Y. Hierarchical surface rough ordered Au particle arrays and their surface enhanced Raman scattering. *Applied Physics Letters* **89**, 181918–181918–3 (2006).

List of Publications

Journal publications:

1. **K. Shadak Alee**, G. Sriram, D. Narayana Rao, "Spectral and morphological changes of 3D polystyrene photonic crystals with the incorporation of alcohols" Optical Materials **34** 1077 (2012).
2. **K. Shadak Alee**, M. Bala Murali Krishna, B. Ashok, D. Narayana Rao "Experimental verification of enhanced electromagnetic field intensities at the photonic stop band edge of 3D polystyrene photonic crystals using Z-Scan technique" Photonics and Nanostructures: Fundamentals and Applications **10** 236 (2012).
3. **K. Shadak Alee**, Maruthi M. Brundavanam, S. N. B. Bhaktha, A. Chiappini, M. Ferrari, D. Narayana Rao "Effect of dye on the band gap of 3D polystyrene photonic crystals" Proc. SPIE **7212** 72120R (2009).
4. **K. Shadak Alee**, B. M. Carina, G. Sriram, D. Narayana Rao "Optical characteristics of different Bragg planes of 3D polystyrene photonic crystals in the LU and LK path of the first Brillouin zone of close packed fcc structure with large band gap depth and steeper band edges" Proc. SPIE **8173** 81730I (2010).
5. **K. Shadak Alee**, M. Bala Murali Krishna, B. Ashok, D. Narayana Rao "Application of 3D Polystyrene Photonic Crystals for Optical Limiting Studies" AIP Conf. Proc. **1391** 260 (2011).
6. **K. Shadak Alee**, B. Ashok, K. L. N. Deepak, R. Kuladeep, D. Narayana Rao "In-situ investigation of the formation of silver nanoparticles in polyvinyl alcohol through Raman spectroscopy" Submitted to Opt. Commun. (Manuscript No. PK-635).
7. **K. Shadak Alee,** D. Narayana Rao "Polarization effects on high Miller index Bragg plane diffraction in 3D polystyrene opal structures" (Manuscript under preparation).

Papers that not included in thesis

1. G. Kurumurthy, **K. Shadak Alee**, D. Narayana Rao "Photoluminescence studies of Si/SiO2 nanoparticles synthesized with different laser irradiation wavelengths of nanosecond pulse duration" Opti. Commun. **282** 3509 (2009).

2. G. Upendar, R. Satyavati, B. Raju, **K. Shadak Alee**, D. Narayana Rao, C. Bansal "Silver nanocluster films as novel SERS substrates for ultrasensitive detection of molecules" Chem. Phys. Lett. **511** 309 (2011).
3. R. Kuladeep, L. Jyothi, **K. Shadak Alee**, K. L. N. Deepak, and D. Narayana Rao "Laser-assisted synthesis of Au-Ag alloy nanoparticles with tunable surface Plasmon resonance frequency" Opt. Matr. Express **2** 161 (2011).
4. K. L. N. Deepak, R. Kuladeep, **K. Shadak Alee,** D. Narayana Rao "Synthesis of silver nanoparticles in poly (vinyl alcohol) matrix in solution and thin films through laser irradiation" J. Nanosci. Nanotechnol. **11** 1 (2011).
5. Sriram Guddala, A. Chiappini, G. Alombert-Goget, C. Armellini, M. Ferrari, **K. Shadak Alee**, Narayana Rao D., A. Chiasera, E. Moser, S. Berneschi, G. Nunzi Conti, G. C. Righini, P. Féron "Fabrication and characterization of confined structures for sensing and lasing applications" Proc. SPIE 8173, 817317 (2010).
6. G. Sriram, **K. Shadak Alee**, A. Chiappini, M. Ferrari, D. Narayana Rao "Experimental investigation on effect of photonic band gap on enhancement of Raman-scattering in metal-dielectric colloidal crystals" Submitted to J. Appl. Phys.
7. R. Kuladeep**, K. Shadak Alee**, D. Narayana Rao "Synthesis of laser-induced Au colloidal nanoparticles and their nonlinear optical properties" Accepted in Adv. Mat. Lett.
8. C. Dennis, **K. Shadak Alee**, D. Narayana Rao "Synthesis and Characterization of Silver Nanoparticles Produced by Laser Ablation Technique in Aqueous Monomer Solution" J. Trens. Chem. **2** 1 (2011).
9. P. Prem Kiran, S. Venugopal Rao, M. Ferrari, B. M. Krishna, H. Sekhar, **K. Shadak Alee**, D. Narayana Rao "Enhanced optical limiting performance through nonlinear scattering in nanoparticles of CdS, co-doped Ag-Cu, and BSO" Nonlinear Optics and Qunatum Optics, **40** 223 (2010).
10. C. Dennis, **K. Shadak Alee**, D. Narayana Rao, S. Vidya "Synthesis and Characterization of Silver Nanoparticles Produced by Laser Ablation by manual adjustment of ablating target at two different time intervals " International journal on nanomaterials and technology **2** 47 (2011).

Conference Papers (International and national):

1. **K. Shadak Alee**, Maruthi M. Brundavanam, S. N. B. Bhaktha, A. Chiappini, M. Ferrari, D. Narayana Rao, "Rhodamine B doped 3D polystyrene photonic crystals" Photonics-2008, IIT-Delhi, India, Dec 15^{th} -17^{th}, 2008. [Poster Presentation]

2. **K. Shadak Alee**, K. S. Bindra, D. Narayana Rao, "Three dimensional photonic crystals and their optical characteristics", National Laser Symposium-09, BARC, Mumbai, India, Jan 13th -16th, 2009. [Poster Presentation]
3. **K. Shadak Alee**, D. Narayana Rao "Fabrication of 3D polystyrene photonic crystals towards the application of micro-lasers and refractive index sensors" 'Physics at small scales' University of Hyderabad, Hyderabad, India, Feb 18th - 19th, 2011. [Poster presentation]
4. **K. Shadak Alee**, B. M. Carina, G. Sriram, D. Narayana Rao "3D polystyrene photonic crystals and study of higher order Bragg-diffraction" International conference on Photonics-2010, IIT Guwahati, India, Dec 11th -15th, 2010. [Poster presentation]
5. **K. Shadak Alee**, G. Sriram, B. M. Carina, D. Narayana Rao "Optical characteristics of bare and doped 3D polystyrene photonic crystals" National Laser Symposium-09, RRCAT, Indore, India, Jan 1st - 4th, 2010. [Poster Presentation].
6. **K. Shadak Alee**, M. Bala Murali Krishna, B. Ashok, D. Narayana Rao "Application of 3D Polystyrene Photonic Crystals for Optical Limiting Studies" 'International conference on light (OPTICS 11)', Calicut, Kerala, India, May 23th - 25th, 2011. [Oral presentation]
7. **K. Shadak Alee**, G. Sriram, D. Narayana Rao "Spectral characteristics of dye and alcohol doped 3D polystyrene photonic crystals" 'International conference on materials science and technology' St. Thomas College Pala, Kottayam, Kerala, India, June 10th -14th, 2012. [Poster presentation]
8. **K. Shadak Alee**, D. Narayana Rao, "Micro-Raman spectroscopy of in-situ formation of silver nanoparticles in polymer matrix" 23rd International conference on Raman spectroscopy, IISc, Bangalore, India, August 12th -17th, 2012 [Accepted for Poster presentation]
9. R. Kuladeep, L. Jyothi, **K. Shadak Alee**, K. L. N. Deepak, D. Narayana Rao " Synthesis of gold and silver nanoparticles in PVA matrix with laser irradiation" 'Emerging trends in applications lasers and accelerators in nano materials (ETALAN-2011)' BARC, Mumbai, India, Oct 20th-21st, 2011). [Poster presentation]
10. B. Ashok, **K. Shadak Alee**, K. L. N. Deepak, H. Sekhar, B.M. Krishna, D. Narayana Rao "Nanophotonics at University of Hyderabad " Workshop on 'Recent trends in nanophotonics' IIT Delhi, India, Sept 30th -Oct 1st, 2011). [Poster presentation]

11. Sriram Guddala, A. Chiappini, G. Alombert-Goget, C. Armellini, M. Ferrari, **K. Shadak Alee**, Narayana Rao D., A. Chiasera, E. Moser, S. Berneschi, G. Nunzi Conti, G. C. Righini, P. Féron "Fabrication and characterization of confined structures for sensing and lasing applications" International conference on Photonics-2010, IIT Guwahati, India, Dec 11^{th} -15^{th} , 2010. [Poster presentation]
12. S. Guddala, A. Chiappini, C. Armellini, L. Battisti, M. Benedetti, M. Brenci, , M. Ferrari, M. Pozzi, **K. Shadak Alee**, D. Narayana Rao,G. C. Righini, S. Soria, D. Zonta, R. Zandonini, "Mechanochromic colloidal crystals for strain detection" International conference on Photonics-2010, IIT Guwahati, India, Dec 11^{th} -15^{th} , 2010. [Poster presentation]
13. Sriram Guddala, A. Chiappini, G. Alombert Goget, C. Armellini, **K. Shadak Alee**, M. Ferrari, D. N. Rao, "Confined Structures: Fabrication and Characterization" National Laser Symposium-09, RRCAT, Indore, India, Jan 1^{st} -4^{th}, 2010. [Poster Presentation]

Awards:

1. **K. Shadak Alee**, D. Narayana Rao "Fabrication of 3D polystyrene photonic crystals towards the application of micro-lasers and refractive index sensors" (**Best poster Award**, Poster presentation at the conference on 'Physics at small scales' held at University of Hyderabad, Hyderabad, India, Feb 18^{th}-19^{th} , 2011).
2. **K. Shadak Alee**, G. Sriram, D. Narayana Rao "Spectral characteristics of dye and alcohol doped 3D polystyrene photonic crystals" (**Best poster Award**, Poster presentation at the conference on 'International conference on materials science and technology' St. Thomas College Pala, Kottayam, Kerala, India, June 10^{th}-14^{th}, 2012).

==========*****==========